Fall 12-1-2020

Cost-Effective GNSS Hardware for High-Accuracy Surveys and Its Prospects for Post-Processed Kinematic (PPK) and Precise Point Positioning (PPP) Strategies

Johnson Olusegun Oguntuase

COST-EFFECTIVE GNSS HARDWARE FOR HIGH-ACCURACY SURVEYS AND ITS PROSPECTS FOR POST-PROCESSED KINEMATIC (PPK) AND PRECISE POINT POSITIONING (PPP) STRATEGIES

by

Johnson Olusegun Oguntuase

A Dissertation
Submitted to the Graduate School,
the College of Arts and Sciences
and the School of Ocean Science and Engineering
at The University of Southern Mississippi
in Partial Fulfillment of the Requirements
for the Degree of Doctor of Philosophy

Approved by:

Dr. Anand Hiroji, Committee Chair
Dr. David Wells
Dr. Sunil Bisnath
Dr. Stephan Howden
Dr. Davin Wallace

December 2020

Published by the Graduate School

ABSTRACT

This dissertation determines for the first time the vertical accuracy achievable with low-cost mass-market multi-frequency, multi-GNSS (LM3GNSS) receivers, and antennas in the context of Ellipsoid Reference Survey (ERS), usually employed in bathymetric operations aboard survey platforms. LM3GNSS receivers are relatively new in the market, and their emergence is driven by the automobile industry and several mass-market applications requiring location-based solutions at high accuracies. It is foreseeable that emerging hydrographic survey platforms such as autonomous surface vehicles, small unmanned aircraft, crowd-sourced bathymetric platforms, and offshore GNSS buoy will find LM3GNSS receivers attractive since they are power- and cost-effective (often less than $1,000 per unit). Previous studies have shown that some mass-market GNSS receivers' positioning accuracy is at the sub-meter level in some positioning strategies, but the authors rarely discussed the vertical accuracy. In rare cases where attention is given to the vertical component, the experiment design did not address the dynamic antenna scenario typical of hydrographic survey operations and the positioning performance that meets the hydrographic survey community's aspirations.

The LM3GNSS receivers and low-cost antennas considered in this dissertation achieved vertical accuracies within 0.15 m at a 95% confidence level in simulated precise point positioning (PPP) and post-processed kinematic positioning strategies. This dissertation characterizes the signal strength, multipath, carrier-phase residuals, and code residuals in the measurement quality assessment of four LM3GNSS receivers and four low-cost antennas. The dissertation investigates the performances of the LM3GNSS receivers and low-cost antennas in different antenna-receiver pairings, relative to a high-

grade GNSS receiver and antenna in simulated-kinematic and precise point positioning (PPP) strategies. This dissertation also shows that solutions with an uncalibrated antenna improve with a cloned ANTEX file making the results comparable to those achieved with a high-end GNSS antenna. This dissertation also describes a GNSS processing tool (with graphic user interface), developed from scratch by the author, that implements, among others, orbit interpolation and geodetic computations as steps towards multipath computation and analysis. The dissertation concludes as follows: (1) The LM3GNSS hardware considered in this dissertation provides effective alternative positioning and navigation performance for emerging survey platforms such as ASV and sUAS. (2) LM3GNSS hardware can meet vertical positioning accuracy on the order of 0.15 m at a 95% confidence level in PPP strategy on less dynamic platforms. (3) LM3GNSS receivers can provide PPK solutions at medium (30 – 40 km) baselines with a vertical positioning accuracy better than 0.15m at a 95% confidence level. (4) LM3GNSS receivers in PPP strategy should meet IHO S-44 order-1 and order-2 in shallow waters. (5) Zephyr3 antenna, being a high-end GNSS antenna, may not always offer the best performance with the LM3GNSS receiver, especially in a dynamic environment. (6) Given the current tracking capabilities, the measurement quality, and positioning performances of LM3GNSS receivers relative to the geodetic grade receiver, it is foreseeable that the distinction between high-end GNSS and LM3GNSS receivers will most likely fade away as GNSS hardware technology advances. (7) Maximizing an LM3GNSS receiver in PPK strategy requires a multi-constellation-enabled reference station and high (i.e., 1 Hz) data tracking rate; otherwise, the PPK solutions will likely drift up to 20 cm.

ACKNOWLEDGMENTS

I am grateful to have been fully funded throughout my graduate degree program at USM from the grants (NA11OAR4320199 and NA16OAR4320199) awarded by NOAA's Office of Ocean and Atmospheric Research, US Department of Commerce. The research reported in this dissertation was conducted under the grant (NA16OAR4320199) received by the Hydrographic Science Research Center (HSRC) of the University of Southern Mississippi (USM).

Thanks to Kevin Martin for assistance in constructing the RG58 cables and the enclosure for the UB4B0M receiver. I do appreciate the professional services of faculty and staff of the Division of Marine Science for their academic and administrative contributions while navigating this Ph.D. program. Thanks also to the Director of HSRC, Captain Brian Connon, Ret., for the prompt approvals of hardware acquisition funds.

Special thanks also to all the Dissertation Committee members, Dr. Hiroji, Dr. Wells, Dr. Bisnath, Dr. Howden, and Dr. Wallace, for their professional mentorship, advice, and constructive criticisms while pursuing this program at USM. The supervisory role played by Dr. Sunil Bisnath during this dissertation has strengthened my resolve to apply skills acquired during this dissertation in solving some engineering-related problems. Some of such projects are planned for execution in the immediate future.

The unflinching guidance, support, and mentorship of Dr. David Wells (Professor Emeritus) since 2017 is well appreciated. His unique mentoring style has entrenched a new level of expertise upon which I will build the next phase of my career. In my opinion, Dr. Wells is a true father, and with his retirement from an active academic career, I have resolved to strive hard in order to sustain and perhaps further his legacies.

DEDICATION

In fall 2015, I decided to resume the Hydrographic Science class at the Division of Marine Science, Stennis Space Center, Mississippi. That decision would have earned me a second Master of Science degree but for the encouragement of my spouse, Tolulope M. Oguntuase, who persuaded me to pursue my age-long passion for a doctorate and a world-class career. Tolulope emphasized that it was now or never. For me, I was between the devil and the deep blue sea, knowing that I was married, with children, and such responsibility is no mean task, in addition to plunging into years of studies, hard work, mental drills, and perhaps life-long readings.

Inundated with thoughts of coping with family responsibilities while pursuing a Ph.D. degree, on the other hand, I imagined the regrets I would bear if I opted to sacrifice my passions for the immediate succor to ease what I considered challenges. The decision was tight, and it was only possible with the gritty support of my spouse, Tolulope. Perhaps I would not have come this far without her motivations and sacrifices. I, therefore, dedicate this dissertation to Tolulope and my children, who tolerated me in the last five years during the M.Sc. and the Ph.D. degree programs.

This dissertation is also dedicated to my mother and siblings for their benevolence and motivation. I have reasons to be grateful to friends who supported my family as we navigated the "… blue sea," particularly Mr. Hayward and Mrs. Charry Rapp, who played supportive roles in various capacities. Lastly, I am grateful for the spirit of academic excellence that my late father engraved on my heart as early as age six. Though he passed on while I was barely twenty, his legacy lives on.

TABLE OF CONTENTS

LIST OF TABLES

LIST OF ILLUSTRATIONS

LIST OF ABBREVIATIONS

AC	Analysis Center
ANTEX	antenna exchange format
ASV	autonomous surface vehicles
BDS	Beidou
C/A	coarse / acquisition code
CDDIS	Crystal Dynamics Data Information System
CDMA	code division multiple access
CORS	continuously operating reference station
DCB	differential code biases
DF	dual frequency
DF-PPP	dual-frequency PPP
DORIS	Doppler Orbitography and Radiopositioning Integrated by Satellite
ERP	earth rotation parameter
ERS	ellipsoid referenced survey
FDMA	Frequency division multiple access
GIM	global ionospheric model
GIPSY	GNSS Inferred Positioning System
GLO	Global’naya Navigatsionnaya Sputnikova Sistema (Russian Global Navigation Satellite System - GLONASS)
GMF	global mapping function

GNSS	Global Navigation Satellite System
GPM	GipsyX Project Manager
GPS	Global Positioning System
GPT2	Global Pressure and Temperature 2
GUI	Graphic User Interface
IERS	International Earth Rotation and Reference Systems
IGS	International GNSS Service
IGSO	inclined geosynchronous orbit
JPL	Jet Propulsion Laboratory
LM3GNSS	Low-power, Mass-market, Multi-frequency, Multi-constellation GNSS
MEO	medium earth orbit
MGEX	Multi-GNSS Experiment
MGNSS	Multi-GNSS
NMF	Niel mapping functions
NGS	National Geodetic Survey
OPUS	Online Positioning User Service
OTL	ocean tide loading
PBM	permanent benchmark
PCO	phase center offset
PCV	phase center variation
PNT	positioning, navigation, and timing

PPK	post-processed kinematic
PPP	precise point positioning
PPP-AR	PPP with Ambiguity Resolution
PRN	pseudo-random noise
RINEX	Receiver Independent Exchange Format
RTG	Real-Time Gipsy
SINEX	Solution Independent Exchange Format
SK-PPP	simulated kinematic PPP
SLR	satellite laser ranging
SNR	signal-to-noise ratio
SP3	Standard Product 3 Orbit Format
SSC	Stennis Space Centre
sUAS	small unmanned aircraft systems
SV	Space Vehicle
SVN	space vehicle number
TVU	total vertical uncertainty
USMCS	USM Calibration Station
UTM	Universal Transverse Mercator
VDOP	vertical dilution of precision
VMF1	Vienna mapping function 1
WLPB	wide-lane phase bias
ZBL	zero-baseline

CHAPTER I - INTRODUCTION

This dissertation describes for the first time the vertical accuracies achievable using Low-power, Mass-market, Multifrequency, Multi-constellation GNSS (LM3GNSS) receivers, and antennas in different positioning strategies in the context of the ellipsoid reference survey (ERS) strategy. It evaluates the results as a precursor to providing alternatives to high-end power-hungry and expensive GNSS hardware on emerging hydrographic and oceanographic survey platforms, such as autonomous surface vehicles (ASV), small unmanned aircraft systems (sUAS), crowd-sourced bathymetric platforms, and offshore GNSS buoys. This chapter presents the research motivation, questions, scope, and contributions.

1.1 Motivation

LM3GNSS receivers are increasingly gaining acceptance for different positioning applications. In contrast with the geodetic grade receivers, they are much more affordable, power-efficient, and customizable for any conceivable application. The price range is a few tens to hundreds of dollars (see Table 1.1). Besides, power efficiency, multi-frequency, and multi-constellation capabilities make them attractive options for mobile applications.

Table 1.1 *Receiver classification*

Receiver types	Price range ($)	Performance	Description
Low-cost	100 – 2,500	cm-level accuracy depending on the strategy	Drones, machine guidance, mapping applications
Geodetic	About 10,000	mm-level depending on the strategy	Survey and geodetic applications

It is conceivable that LM3GNSS would become the preferred GNSS hardware aboard hydrographic vessels and unmanned systems. In recent years, the hydrographic community has witnessed a surge in the emergence of un-manned and remotely operated vehicles in the wake of the campaign to map the entire ocean floor by 2030 (Mayer et al., 2018). The new survey platforms are becoming the preferred platforms of the future for mapping almost any water body, including deep-waters, constricted areas, and nearshore. Before the launching of Seabed 2030, the popularly held report was that 80 % of the world's ocean and seafloor were largely unmapped at the desired resolution (Mayer et al., 2018; Smith, 2018). According to the recent press release by GEBCO, the percentage of the World's seabed, mapped to modern standards had risen from 15 to 19% between 2017 and June 2020 (The Nippon Foundation-GEBCO Seabed 2030 Project, 2020). Since these platforms are widely considered force multipliers, they are expected to play a significant role in achieving the World's seafloor mapping goals.

The role of the GNSS positioning technique in relating soundings to chart datum using the ERS strategy is well documented by (Dodd & Mills, 2012; Mills & Dodd, 2014). The technique offers the most convenient means of reducing soundings to chart-datum, provided the adopted GNSS positioning strategy can achieve the desired positioning accuracy. If LM3GNSS receivers are to replace the geodetic grade for hydrographic surveys, the vertical accuracies achievable in dynamic scenarios must be determined in the context of the error budget and specifications for hydrographic survey application.

1.2 Problem Statement

In determining that LM3GNSS hardware will provide reliable positioning results that meet the ERS requirement in the context of hydrographic survey specifications (S-44 document) of the International Hydrographic Organisation (IHO), this dissertation addresses the following questions:

1. Is it possible to use LM3GNSS hardware to provide adequate alternative positioning and navigation performance for emerging survey platforms such as ASV and sUAS?
2. What are the performances of LM3GNSS hardware in the PPP strategy, especially on platforms like a GNSS buoy?
3. What are the performances of LM3GNSS receivers in PPK solution, and are they suitable alternatives to high-end GNSS receivers when performing special order surveys?
4. What IHO order of survey will LM3GNSS hardware meet when used in the PPP strategy?
5. How do the performances of LM3GNSS hardware vary with different antenna pairings?
6. Given the current tracking capabilities of LM3GNSS receivers, are there factors that predict lesser distinctions in their characteristics and performances relative to high-end receivers commonly used for very high accuracy applications?
7. Will the LM3GNSS receiver achieve high PPK positioning accuracy with continuously operating reference stations even when operating within reasonable (30 – 40 km) baseline length?

1.3 Dissertation Scope

This dissertation describes the vertical accuracies achievable with LM3GNSS receivers when using different low-cost antennas. The performances are based on post-processed kinematic (PPK) results and precise point positioning (PPP) strategies. Besides, the code and carrier phase residuals from these strategies are assessed to provide a stochastic weighting model for measurement types and constellations. Multipath and signal-to-noise ratio (SNR) are assessed to understand the limitations LM3GNSS hardware may have when deciding on an antenna choice. Finally, the limitations of LM3GNSS hardware in comparison with geodetic receivers are also discussed.

1.4 Research Contribution

This dissertation describes, for the first time, the achievable vertical accuracies of LM3GNSS receivers in the context of ERS and total vertical uncertainty (TVU) requirements, especially in shallow waters where un-manned systems play a critical role. This dissertation's novelty is leveraging LM3GNSS receiver, and antennas, for applications requiring low power mass-market high-order positioning accuracy. A newly developed GNSS analysis software (with GUI) called GipsyX Project Manager (GPM) is a significant aspect of this dissertation. The software (8,692 lines), developed from scratch, and the motivation stems from the desire to automate data processing and management in GipsyX and decoding code-phase residual files from GrafNav. As GPM evolves in this dissertation, it engenders in the author a software engineering passion and broader knowledge base in GNSS algorithm development and implementation.

1.5 Dissertation Outline

CHAPTER I highlight this dissertation's motivation; it states the problems addressed; it describes the dissertation scope and its contributions. CHAPTER II chronicles the related literature and the vertical accuracies achieved. A section of the chapter is devoted to antenna types and the factors that determine their performances. CHAPTER III lists the GNSS hardware used in this dissertation and their market prices when writing this dissertation. The chapter also describes the experiment design and data acquisition scheme. In CHAPTER IV, ANTEX file cloning is discussed as a novel approach for improving PPP results with uncalibrated low-cost antennas. The chapter also discusses a new GNSS analysis software, known as GipsyX Project Manager (GPM) is introduced as a tool for multipath characterization, SNR characterization, GipsyX automation, and analysis. Additionally, the chapter describes GPM’s features, including its orbit interpolation technique and the validation relative to an interpolated orbit from GipsyX software. The chapter details the processing strategies and the stochastic estimates for all LM3GNSs receivers per trackable constellation.

CHAPTER V discusses the measurement and positioning performances in the context of ERS. It discusses LM3GNSS performances when using different antennas in different positioning strategies and scenarios. The contextual information provides the readers with various options on how to choose LM3GNSS hardware for their application. This chapter identifies some potential challenges that induce solution degradation when using a standard continuously operating reference station for differential kinematic solutions. The dissertation concludes with a summary, a catalog of future works, and recommendations in CHAPTER VI.

CHAPTER II – LITERATURE REVIEW

The vertical positioning uncertainties of LM3GNSS hardware are rarely discussed in the literature. Often, researchers' focus is on the horizontal component, and in few cases where the vertical uncertainty is discussed, it does not meet the stringent ERS requirements for hydrographic survey operation nearshore. This chapter presents some previous studies and discusses the ERS error budget in shallow waters. It briefly presents some LM3GNSS measurement quality, positioning performances with PPP, PPP with ambiguity resolution (PPP-AR), PPK / RTK, and the impact of antenna type on solution quality.

2.1 Previous Studies on Measurement Quality

For a set of LM3GNSS receivers, Aggrey et al. (2019) show from empirical results that SNR ranges between 35 and 55 dB, the measurement noise is 4m (L1 code minus phase), multipath is 3m, code and carrier phase residuals are generally better than 1 and 0.001 m respectively for a 24-hour dataset when operating in static mode. In kinematic mode, code and carrier phase residuals are better than 10 and 0.05 m for a 50-minute dataset. Those results indicate the measurement quality of LM3GNSS receivers. However, their vertical positioning performances require a thorough assessment through a well-designed experiment, given the vertical component's implication to specific marine applications, such as bathymetric charting and under-keel clearance requirements for vessels approaching port channels.

2.2 Previous Studies on PPP and PPP-AR Performance

PPP is known to offer centimeter- to decimeter-level accuracy at a convergence time between 40 and 60 minutes, depending on the constellation combination scenario

(Cai et al., 2015; T. Liu et al., 2017; Y. Liu et al., 2017; Lou et al., 2016; Sunet al., 2015; Tegedor et al., 2014). While PPP strategy utilizes orbit and clock products to estimate the position of a user without the need for a reference receiver (Zumberge et al., 1997), PPP-AR incorporates atmospheric models in addition to the orbit and clock products from a regional or global network to aid ambiguity resolution and faster convergence (Khodabandeh et al., 2015). The so-called PPP-AR is also known as RTK-aided PPP. It is essentially a hybrid of the well-established PPP and RTK strategies (Wübbena et al., 2005; B. C. Zhang et al., 2010). Researches are on-going to provide PPP-AR corrections in the state space representation where all the parameters in the positioning model are completely modeled and broadcast as a correction service to users

Gill et al. (2018) applied the International GNSS Service (IGS) global ionospheric model (GIM) in addition to real-time precise orbits and clocks as external corrections to GPS L1 C/A observations from Nexus 9 - Broadcom BCM4752, and ublox NEO-M8T to achieve sub-meter accuracy (25 and 51 cm vertical RMS for ublox and Nexus9 respectively) in precise point positioning (PPP) solution. Jokinen et al. (2018) also demonstrate sub-meter level performance with the regional ionospheric model from TerraStar-X as external corrections to achieve 2-minute convergence for L1 C/A observations using mass-market receivers in kinematic PPP. The authors did not include the vertical component's performance as their focus was on the autonomous driving application. Nie et al. (2020) discuss simulated real-time kinematic PPP results with the ublox F9P receiver and a mass-market patch antenna. They claim that 1-sigma RMS value in the vertical component ranges between 0.117 and 0.654 m, while the biases

range from -0.05 m to +0.62m for a proposed dual-frequency (DF) PPP method and the conventional DF-PPP when using different sets of satellites.

2.3 Previous Studies on PPK and RTK Performance

Kirkko-Jaakkola et al. (2015) used a ublox receiver for short-baseline RTK and network RTK solutions (GPS-only) and achieved a 0.5 m vertical accuracy at 92.6% and 90.4% confidence level, respectively. The technical report on low-cost experiments conducted by the University of Minnesota Department of Aerospace Engineering and Mechanics (Gebre-Egziabher et al., 2018) shows the superior performance of mid-range over low-cost receivers. The experiment involved Hemisphere Eclipse P307 (discontinued but replaced by P326 and 327), Swiftnav Piksi Multi, NVS Technologies NV08C-RTK, Emlid Reach, ublox NEO-M8P, and Skytraq S2525F8-RTK. According to the report, RTK testing in different scenarios, using a survey-grade antenna, shows only the DF units (Eclipse P307 (mid-range) and Piksi Multi) are capable of cm-level accuracies (50% of their RTK solutions were fixed at 10 cm accuracy). However, the authors did not discuss the performance in the vertical component.

2.4 Previous Studies on Low-Cost Antennas

The GNSS antenna is crucial to the positioning and navigation performance of any set of hardware, and as such, a quick review is provided here. (Teunissen & Montenbruck, 2017) provides a concise introduction and discussion on GNSS antennas, their characteristics, as well as the classifications (pp. 505-534). The characteristics of a GNSS antenna, which includes center frequency, bandwidth, radiation pattern, polarization, gain, impedance, axial ratio, and multipath rejection ratio, phase center offset (PCO), and phase center variation (PCV) stability, play a significant role in the

quality and application of the antenna. Antenna classification could be design- or application-specific. According to the design technology, an antenna could be a microstrip patch (or simply patch), helix, spiral, etcetera; see Chen et al. (2012) for more antenna classifications. Pesyna et al. (2014) classified GNSS antennas properties, as adapted here in Table 2.1. The classification shows that a geodetic-grade antenna is about the same quality as a mid-grade and better than a high-quality patch antenna, while the ultra-low-cost antenna could be more than ten times worse than a geodetic-grade antenna. Note that most mass-market GNSS antennas are patch antennas. For geodetic grade antennas, multipath rejection and PCV stability are the key factors considered in their designs (Teunissen & Montenbruck, 2017). Depending on the application purpose, an antenna could be navigation, surveying, remote sensing, or anti-jamming type. Overall, those classifications suggest that antennas are intended for different purposes and may not meet the expected performance when used otherwise.

Table 2.1 *Antennas properties (adapted from Pesyna et al. 2014)*

Antenna type	Axial ratio	Polarization	Relative loss
Geodetic grade	1 dB	Circular	0 dB
Mid-grade (patch)	2 dB	Circular	0 - 0.5 dB
Low-grade (patch)	3 dB	Circular	0.6 dB
Ultra-low (smartphone)	10+ dB	Linear	11 dB

The relative loss number indicates the average loss in gain relative to a geodetic-grade antenna. The axial ratio refers to the ratio of the minor and major axis of the antenna polarization ellipse.

Studies (as mentioned in Section 2.2) show that the achievable vertical accuracy is at the sub-meter level for externally-aided PPP when using a low-cost receiver and a patch antenna, in contrast to the 10-cm precision achieved by Banville & Diggelen (2016), with a Samsung Galaxy S7 running the Broadcom 4774 GNSS chip and using a

linearly polarized antenna. It is important to stress here that Banville & Diggelen (2016) did not calibrate their results with an established control and did not demonstrate what accuracy is achievable on a dynamic platform, as would be the typical scenario hydrographic operations. However, Odolinski & Teunissen (2017) shows that cm-level accuracy (less than 10 cm at 97% ambiguity resolution success rate) is achievable in all components when using a low-cost receiver (single frequency GPS-BDS) and a patch antenna for (7-km baseline) RTK positioning. Note also that their receivers remained stationary throughout the experiment, and the author did not discuss the performance when the antenna undergoes high dynamic motions.

In addition to the linear polarization of ultra-low-cost antennas and their sensitivity to multipath resulting in measurement noise; carrier-phase discontinuities caused by the so-called duty cycle mechanism for power conservation is another impediment to exploiting ultra-low-cost GNSS receivers (W. Liu et al., 2019; Pirazzi et al., 2018; Siddakatte et al., 2017; X. Zhang et al., 2018). Note that polarization refers to the electric field vector's orientation, and when the field oscillates in the horizontal or vertical direction, an antenna is said to be linearly polarized. Although continuous carrier phase observation is possible with the linearly polarized antenna of the Nexus 9 tablet, carrier phase ambiguity resolution remains a daunting task (Håkansson, 2019; W. Liu et al., 2019). Håkansson (2019) associated the inability to resolve Nexus-9-tablet ambiguity with the initial phases' arbitrary nature, while W. Liu et al. (2019) associated it with the linearly polarized antenna and frequent phase lock loss. To an extent, this review on different types of antennas implies that users seeking high accuracy performance with

LM3GNSS hardware are limited to the mass-market circularly polarized antennas. Again, this dissertation shows that their performances vary as well.

2.5 LM3GNSS and Vertical Uncertainty Requirements

The literature review suggests that the vertical accuracy when using a ublox receiver and a patch antenna for instantaneous kinematic PPP at 1 Hz ranges between 0.25 and 0.5 m RMS (Gill et al., 2018; Parkins et al., 2018). However, 0.1m accuracy at a 95% confidence level is possible when using low-cost receivers for short (7-km) baseline RTK and externally-aided PPP (Banville & Diggelen, 2016; Odolinski & Teunissen, 2017). The 0.1-m low-cost RTK and PPP accuracy are yet to be shown possible for longer baselines and consistent with established calibration stations. While the vertical accuracies discussed in some literature may suffice for autonomous driving, a more demanding performance is required in some nearshore hydrographic applications. In most of the reviewed literature, the experiment designs, primarily where the vertical uncertainty is discussed, did not factor in the positioning and navigation dynamics on typical marine platforms.

2.5.1 Total Vertical Uncertainty in Shallow Waters

Given the critical importance of vertical accuracies to nearshore bathymetric mapping and its repeatability, regulatory organizations establish the survey standard and specifications for survey products. An example is a minimum standard set by the IHO that requires a total vertical uncertainty (TVU) at a 95% confidence level, for Special Order bathymetric surveys, that has a depth-independent factor of 0.25 m and a depth-dependent factor that is 0.75% of water depth (IHO, 2008). This dissertation shows in Figure 2.1 a concise interpretation of the TVU tolerance at a 95% confidence level that

must include all the uncertainties from depth-dependent parameters. For example, the ellipsoid-to-chart datum method of sounding reduction must account for the uncertainties associated with but not limited to the ellipsoid-chart-datum separation model, GNSS vertical positioning, sensor lever-arms (up/down) relative to the vessel reference point, sensor frame misalignment relative to vessel frame, and sounding depth.

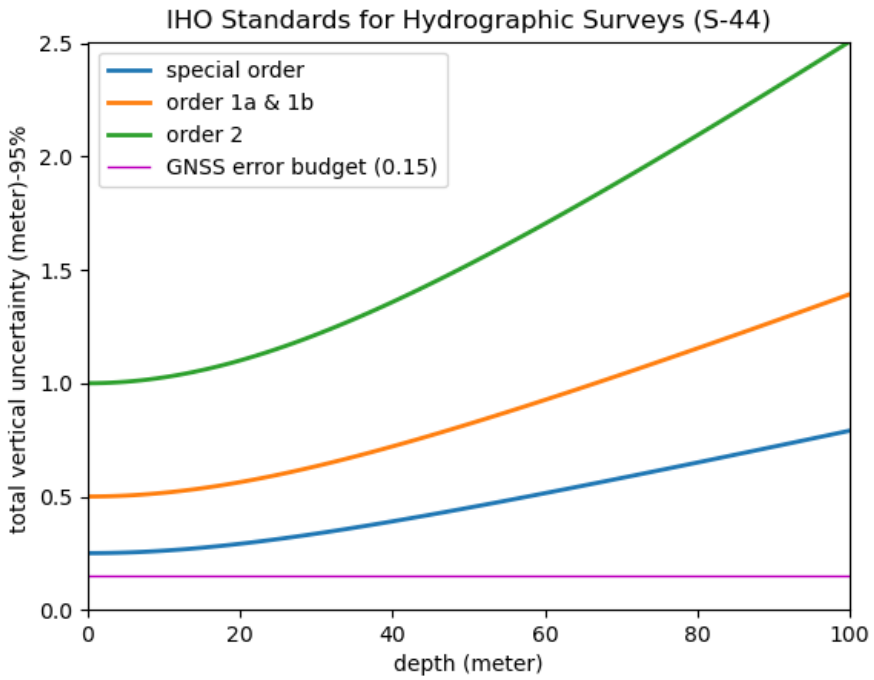

Figure 2.1 *Maximum allowable total vertical uncertainty (TVU) requirements*

This dissertation imposes a conservative criterion of 0.15 m at a 95% confidence level on the LM3GNSS positioning results to determine whether LM3GNSS receivers will meet the stringent requirements for nearshore coastal mapping. That criterion is derived by considering the ERS's reasonable uncertainty values for depth-independent parameters adapted from the Hydrographic Survey Specifications and Deliverables (HSSD) published yearly by National Ocean Services (NOS) and from Kongsberg's EM

Technical Note 2001. The parameters and the imposed criterion are discussed in detail in Section 2.5.2.

2.5.2 GNSS Error Budget in ERS Strategy

This subsection briefly discusses the criterion imposed on the vertical positioning uncertainty of LM3GNSS as the standard for deciding whether they can meet hydrographic survey specifications, especially in shallow waters. According to the discussion in Section 2.5.1, the reasonable threshold for the LM3GNSS component of the TVU error budget should not exceed 0.15 m at a 95% confidence level, also confirmed by Rice & Riley (2011). Those estimates accounted for various uncertainty estimates, especially in the ERS strategy, as discussed in the next few paragraphs.

In the ERS strategy, soundings are reduced to chart datum by applying the ellipsoid-chart-datum separation (Sep value/model). Mills & Dodd (2014) discussed the established procedures for determining a separation model that varies for different locations and the chosen ellipsoid reference surface. A separation model may be determined from an existing model like the VDatum used in the United States or via direct measurements. Whatever strategy is adopted in determining the separation model, an error budget scheme must account appropriately for all the uncertainties associated with the relevant parameters.

This dissertation assumes a simple direct measurement scenario, as shown in Figure 2.2, for separation model determination. Hence, the uncertainties will include the following parameters: (1) tidal datum reduction to the permanent benchmark (PBM) which comprises, leveling procedure between PBM and tide staff, pressure sensor (tide gauge) measurements, sensor calibration, dynamic effect (due to wave, current, and

density), barometric pressure correction, tide-staff-to-gauge reading, and the chart datum transfer from existing tidal stations; (2) ellipsoid-reference-to-PBM separation; (3) GNSS navigation uncertainty, especially in the vertical component (that is the error budget this Section estimates as a criterion in determining whether the performance of LM3GNSS hardware will meet stringent hydrographic specifications), the lever-arm offsets of the antenna, and the inertial measuring unit (IMU); (4) depth-measurements which includes, the mounting angles of both the IMU and the multi-beam sonar relative to the vessel reference frame, beam steering angle, roll, pitch, sound speed in water column and at the surface, and most importantly the sonar sounding error in the outer beams.

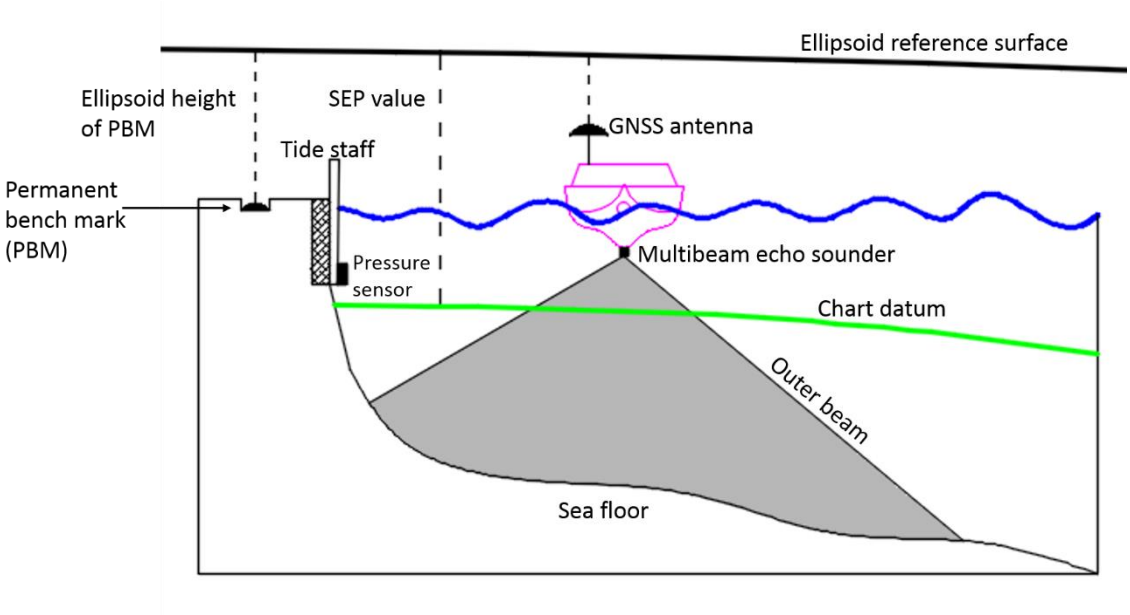

Figure 2.2 *ERS scenario and TVU*

Readers interested in the mathematical models for estimating all multibeam-related uncertainties should refer to Hare et al. (1995). The expected cumulative uncertainties (95% confidence level) for all parameters highlighted in (1) to (4) are discussed in HSSD, 2019, pp 19 – 21, pp 72 – 74, and summarized here in Table 2.2. From the reasonable values of those parameters listed in Table 2.2, the estimated GNSS

vertical uncertainty is 0.18 m. Thus, it is reasonable to impose the conservative criterion of 0.15 m, similar to the 0.14m value reported by Rice & Riley (2011).

Table 2.2 *ERS-related uncertainties from NOAA's HSSD and EM Technical Note*

Parameter	**Range of Uncertainty Estimates**	**Reasonable values**
Timing	0.010 — 0.02 s (approx. 2 to 6 cm at 5 knots)	0.04
Vessel offsets	0.002 — 0.2 m	0.05
IMU alignment	< 2 degree (better than 10 cm for short lever arms)	0.10
Sound speed	0.6 m/s (up to 1 cm for depths up to 25 m)	0.01
Ellipsoid-chart datum separation (SEP)	0.17 m	0.10
Sonar dept resolution	0.06 to 0.08 m	0.08
GNSS component	Not explicitly specified	0.18 m (for depths between 1 and 20 m)

Note that the uncertainty estimate for sonar dept resolution is extracted from Hammerstad (2001).

CHAPTER III – DATA COLLECTION METHOD

This dissertation collected kinematic datasets with different antenna-receiver pairings to simulate dynamic and less dynamic environments typical in hydrographic survey operations to address the research questions. The data collected at a calibration station simulates the less dynamic environment while those collected in a minivan simulates the dynamic environment. This chapter describes the receivers and antennas used, the data acquisition techniques, the experiments, and their locations.

3.1 Experiment Design

Five pairs of receivers (Table 3.1) and antennas (Table 3.2) are involved in the LM3GNSS hardware experiments discussed in this dissertation. ZED-F9P, Duro, Mosaic, and UB4B0M are new brands of LM3GNSS receivers released into the market between 2018 and 2019. Note that the Duro receiver is the ruggedized version of Piski Multi and that the GNSS boards for both are the same. All the receivers are capable of tracking the four global navigation systems, viz. GPS, GLONASS (GLO), Galileo (GAL), and Beidou (BDS). A zero-baseline (ZBL) setup permits multiple GNSS receivers to share a single antenna via a signal splitter. The ZBL setup was adopted for all observation sessions. It allowed the simultaneous tracking of GNSS signals arriving at the same position from the same path for all five receivers. Also, the ZBL setups allowed the comparison of instantaneous positioning solutions between different receivers. A single antenna fed the five receivers simultaneously using ALDCBS1X8 amplified splitter from GPS Networking (see Figure 3.1). The observation sessions with different antennas allowed the assessment of different antenna grades with LM3GNSS receivers. See Figure 3.1 for

a detailed wire diagram of the ZBL setup and APPENDIX A (Figure A.1a to Figure A.1d, Figure A.2, and Figure A.3) for the real-life images of the ZBL setups.

Table 3.1 *Receivers investigated*

Manufacturer	**Receiver**	**Price / unit**
Trimble	NetR9	$10,000.
Drotek	ZED-F9P (ublox)	$243
Swift Navigation	Duro*	$2,670
Septentrio	Mosaic	$895
Unicore Communications	UB4B0M	$575

The experiments used Trimble NetR9 (geodetic grade GNSS receiver) as the standard for characterizing the performances of LM3GNSS.receivers. * An equivalent of Piski Multi Evaluation Kit; standard delivery includes two pairs of receivers, two antennas, and accessories cost $2,295.00.

This dissertation classifies the patch antennas used during field experiments into three, namely: fully calibrated, partially calibrated, and uncalibrated. “Fully calibrated” implies the azimuth- and non-azimuth dependent PCV pattern, for at least two frequencies, are provided in the antenna exchange format (ANTEX) file. “Partially calibrated” means only the non-azimuth dependent PCV records are available in the ANTEX file. “Uncalibrated” implies neither IGS nor National Geodetic Survey (NGS) provides any calibration information for an antenna in their databases.

Table 3.2 *Antennas investigated*

Manufacturer	**Antenna**	**Price/unit**	**Description**
Trimble	Zephyr 3	$2,300	Fully calibrated
Drotek	DA910	$109	Uncalibrated
Swift Navigation	GPS500	$225	Uncalibrated
Septentrio	PolaNt-x MF	$660	Partially calibrated
Harxon Corporation	HXCCSX601A	$450	Partially calibrated

The LM3GNSS experiments involved PPP and PPK observation sessions in simulated-kinematic (antenna is stationary, but receiver and processing in kinematic mode - that is one position fix per epoch) and kinematic (antenna moving, and processing in kinematic) modes to address the question, whether LM3GNSS hardware can meet vertical accuracy requirements using the ERS technique. The PPP observation sessions simulate the scenario using LM3GNSS receivers at a remote location while the PPK sessions simulate the scenario nearshore. Given that the receivers have different tracking capabilities, the performances of the receivers are expected to differ. The receivers' measurement quality assessment is based on the dataset collected during the simulated-kinematic sessions, using SNR, multipath, and the number of satellites tracked as performance metrics.

NetR9, Mosaic, and UB4B0M tracked all the four global constellations on three frequency bands using 440, 448, and 432 channels, respectfully. Drotek / DP0601 (184 channels) and Duro also tracked the four global systems but only on two frequency bands per constellation. Section 4.4.5 provides further details on the datatypes tracked by the LM3GNSS receivers.

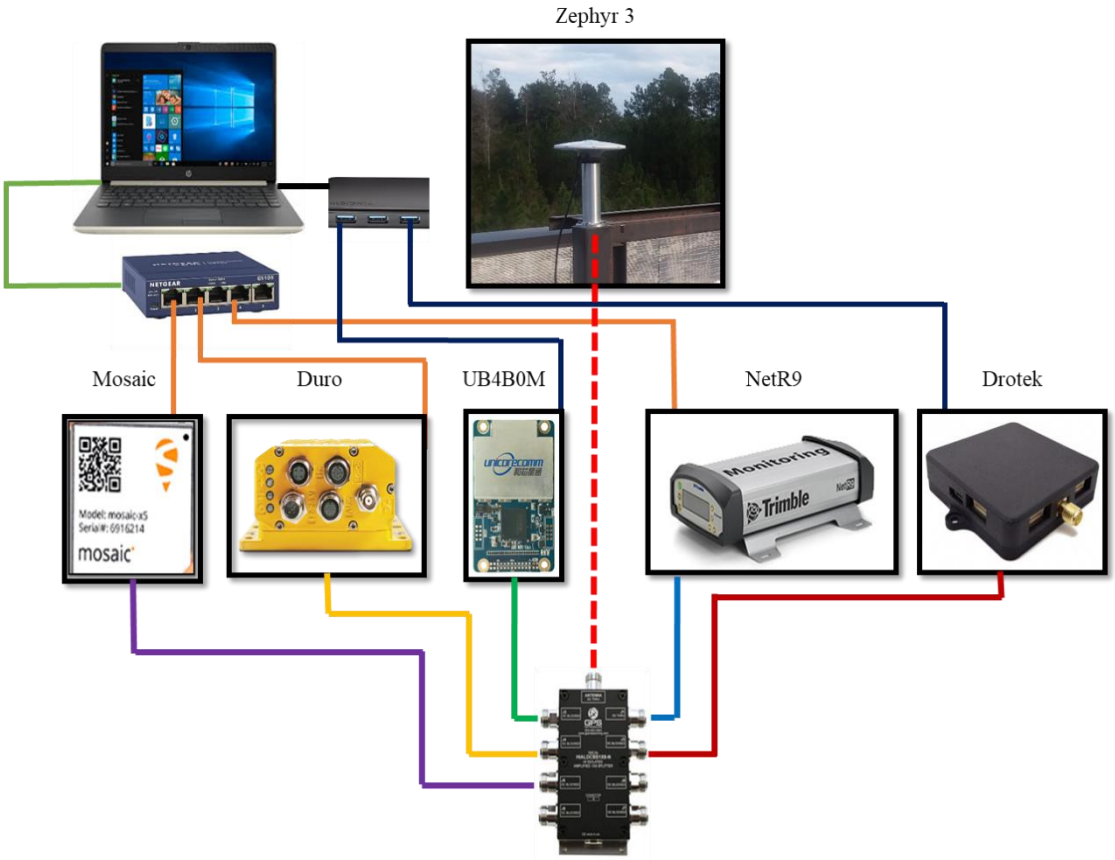

Figure 3.1 *LM3GNSS and NetR9 in a ZBL setup at USM calibration station*

1-m RG54 cables connected the receivers to the antennas splitter to keep measurement noise the same as much as possible. Unicore Communication supplied their GNSS hardware without enclosures; hence, the local construction with a pelican case provided the UB4B0M modules and carrier boards' encasement.

3.2 Data Acquisition

The experiment design required the establishment of a calibration station as the testbed for the LM3GNSS hardware. Established on the roof of Building 1029 (University of Southern Mississippi (USM) Ocean Support Facility) at Stennis Space Center, MS is a continuously operating reference station (CORS), designated USM Calibration Station (USMCS). Its coordinates (calibration coordinates) provided the ground validation of LM3GNSS PPP solutions. Moreover, LM3GNSS PPK used USMCS as the reference station in the double-differencing solution.

The establishment of USMCS occurred in 2017. Ever since a Trimble NetR9 and Zephyr 3 antenna had continuously acquired GNSS signals at 1 HZ. Although data outages occurred during antenna replacement, receiver configuration, system reboot, and troubleshooting, a 24-month simulated-kinematic dataset was collected with the Trimble hardware until late 2019 LM3GNSS observations began. That allowed for some preliminary studies of multi-GNSS (MGNSS) processing.

The first set of USMCS coordinates was determined on Jun 2, 2018, using the static dataset collected from Apr 2 to 8, 2018. As NGS transitioned from IGS08 to the ITRF2014 in September 2019 (National Geodetic Survey, 2019), a new computation of the coordinates of USMCS became necessary to ensure that USMCS is consistent with the NGS network. Nine sessions of static datasets, from Jan 1 to 9, 2020, were collected and used to determine a new set of ITRF2014 calibration coordinates. Section 4.3 further discusses the computation and uncertainty of the calibration coordinates.

3.2.1 Simulated-Kinematic PPP (SK-PPP) Data Acquisition

LM3GNSS receivers and Trimble NetR9 collected twelve GNSS data sessions at USMCS, in a ZBL setup, at a 1-Hz sampling rate. Each session used a different antenna, and the observations lasted three consecutive days to allow for GPS ground track repeat. Only a 24-hour period per session contributed to the LM3GNSS SK-PPP performance assessment. Note that the data collected at USMCS were used twice: for both SK-PPP and PPK solutions.

Table 3.3 list the datasets contributing to the LM3GNSS SK-PPP studies. For preprocessing trials and stochastic inference, this dissertation used the data collected on Dec 29, 2019. The data acquisition used receiver-specific control software is listed in Table 3.4.

Table 3.3 *SK-PPP data acquisition session*

Date	**Antenna**	**Comment**
Dec 29, 2019	Trimble Zephyr 3	Five receivers in ZBL setup; used data for stochastics estimation
Feb 6, 2020	Swift Nav. GPS500	Five receivers in ZBL setup
Feb 10, 2020	Septentrio PolaNt-x MF	Five receivers in ZBL setup
Feb 13, 2020	Harxon Corp. HXCCSX601A	Five receivers in ZBL setup
Feb 17, 2020	Trimble Zephyr 3	Five receivers in ZBL setup
Mar 11, 2020	Drotek DA910	Five receivers in ZBL setup

Table 3.4 *Receiver firmware and control software*

Receiver	**Firmware version**	**Control software**
NetR9	5.44	Trimble browser interface
ZED-F9P (ublox)	27.11	U-Center 19.08.01
Duro	PiksiMulti-v2.3.17	Swift Console v2.3.17
Mosaic	4.7.1	Septentrio browser interface and *RxControl
UB4B0M	**	U-Precise 1.6, Build 11357

*RxControl is a desktop software utility that offers many of the features in its web browser version. ** Not retrievable from control software

3.2.2 Kinematic PPP and PPK Data Acquisition

In a ZBL configuration, two sets of LM3GNSS and NetR9 receivers tracked signals, simultaneously at USMCS and in a minivan, at 1 Hz during the kinematic sessions (see the setups in APPENDIX A). The Kinematic PPP solutions used only the dataset collected in the minivan, while the PPK solutions, relative to USMCS, used the dataset from matching pairs of receivers at USMCS and in the minivan. The minivan traveled about 35 km on US Highway 90, at an average speed of 80 km per hour, between Stennis Space Center (SSC) and Pass Christian, Mississippi. Figure 3.2 shows the route in solid red. SSC is to the west of Diamondhead and on the border between Louisiana and Mississippi, and Pass Christian is southeast of Diamondhead. When roving the highway, the open sky condition simulates the typical access to GNSS signals during a marine survey.

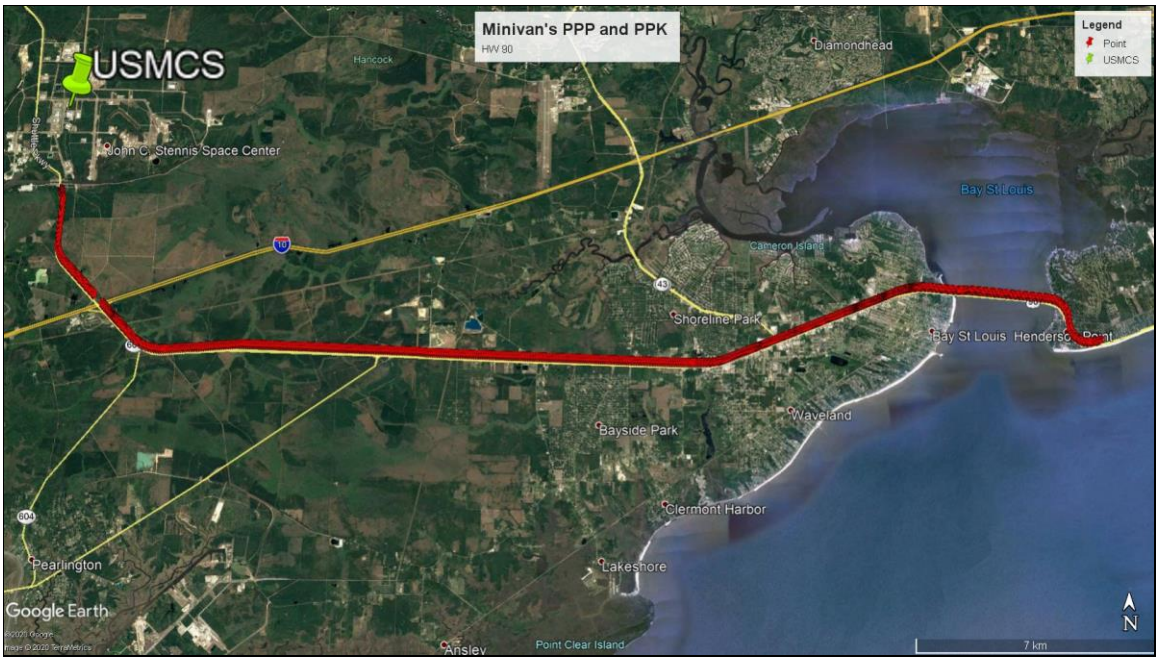

Figure 3.2 *Minivan data acquisition route*

GNSS receiver pairs collected data simultaneously at USMCS and aboard a minivan. The roving receivers collected ten sessions of kinematic datasets on different days with different antennas. However, only five sessions (Table 3.5), coincident with the 24-hour SK-PPP sessions at USMCS, are selected to contribute to the minivan's kinematic positioning analysis. The following reasons explain the non-inclusion of the other five kinematic sessions in the minivan's positioning analysis. The dataset collected on Feb 4, 2020, was incomplete. Only half of the trajectory was recorded for most receivers as the computer entered hibernation mode due to a power supply outage from its battery. During subsequent data acquisition, the solution was to purchase two additional units of DC-to-AC converters to provide sufficient in-car power outlets for the ethernet hub, GNSS receivers, and laptop. The other four sessions were collected between Oct 30, 2019, and Nov 10, 2019. Those sessions did not include the UB4B0M roving receiver because the modules require carrier boards that were not delivered until

the middle of December 2020. Additionally, the fabrication of the enclosures for those receivers was completed in mid-January 2020.

Table 3.5 *Kinematic PPP and PPK data session*

Date	**Time**	**Duration (min.)**	**Antenna**
Feb 06, 2020	20:12 – 20:40	28	Swift Nav. GPS500
Feb 10, 2020	17:46 – 18:16	30	Septentrio PolaNt-x MF
Feb 13, 2020	16:47 – 17:14	27	Harxon Corp. HXCCSX601A
Feb 17, 2020	16:51 – 17:17	26	Trimble Zephyr 3
Mar 11, 2020	16:43 – 17:14	31	Drotek DA910

CHAPTER IV – DATA PROCESSING METHODS

This chapter describes the data processing methods for the GNSS processing packages used in determining the vertical positioning uncertainties possible with different antenna-receiver pairings in kinematic PPP and PPK positioning strategies. The dissertation introduces a newly developed software for data quality characterization.

4.1 Data Processing Overview

Section 4.2 describes the leading software suites (Table 4.1) involved throughout the GNSS data processing and analysis of this dissertation. Section 4.2.2 introduces GPM as in-house software development and as a significant contribution to this work. Relevant sections of this chapter discuss GPM features, and the full highlights of its capabilities are documented in APPENDIX B. The determinations of USMCS coordinates used for the validation of LM3GNSS performances are the focus in Section 4.3. Sections 4.4 and 4.5 describe the processing strategy adopted in answering the research questions posed in Section 1.2. Sections 4.6 and 4.7, respectively, provide brief discussions on the stochastic model and what to expect from receiver-dependent multipath mitigation capabilities of all the receivers involved in the dissertation experiment.

Table 4.1 *Software packages and tools*

Software packages and tools	**Purpose**
GipsyX version 1.2	SK-PPP
GrafNav version 8.9	Kinematic PPP and PPK
GipsyX Project Manager version 1	Automated scripting
	Data analysis
	Data management
RINEX tools *	Pre-processing

*See Section 4.2.2.6 for further details on Receiver Independent Exchange (RINEX) tools

4.2 Software Overview

Jet Propulsion Laboratory (JPL) GipsyX software (version 1.2) offers features that are not openly available in commercial software. As such, it was preferred above the Hexagon-Novatel's GrafNav suite for SK-PPP processing. The following subsections describe the software packages used in this dissertation.

4.2.1 GipsyX

Bertiger et al., 2020 describes GipsyX as the JPL's software for positioning, navigation, timing (PNT), and earth science measurements utilizing a variety of techniques, which includes Global Navigation Satellite Systems (GNSS), Satellite Laser Ranging (SLR), and Doppler Orbitography and Radiopositioning Integrated by Satellite (DORIS). JPL developed GipsyX as the C++ and python replacement for the famous GNSS Inferred Positioning System (GIPSY) and Real-Time Gipsy (RTG), leveraging the pioneering works of GIPSY-OASIS (Bertiger et al., 2020; Yoaz, 2017). Variants of GIPSY software dates back to 1980, starting with Proto GIPSY (Yoaz, 2017). The core computational part of GipsyX is written in C++, while the scripting part is written in Python3 (Bertiger et al., 2020). GipsyX's license is royalty-free, and it is available to hundreds of academic and research institutions for non-profit use. It supports a wide range of GNSS processing, including precise orbit determination, ephemeris prediction, real-time orbit determination, and Multi-GNSS (GPS, GLO, BDS, GAL) PPP solutions for ground receivers. (Villiger, A., Dach, 2017). GipsyX is Linux-based and open-source. The input and output are ASCII-based, offering easy modifications to files as necessary, making it an essential processing package for LM3GNSS PPP studies.

4.2.2 GipsyX Project Manager (GPM)

Motivated by the extensive data collected for analysis, GipsyX Project Manager (GPM) version 1 was developed for this dissertation in MATLAB from scratch, in the quest to ease the record-keeping, processing steps, and analysis. The software runs 91 functions, a total of 8,692 lines of codes, including the Graphic User Interface (GUI). Note that the GUI design implementation alone consists of 1,323 lines of codes. The software supports automated scripting of GipsyX command-line operations for onward use in the Linux environment. It supports a structured repository unique to the observation mode and hardware used during an observation session and automated extraction of information from GipsyX and GrafNav ASCII and binary files (see APPENDIX C for GrafNav (Waypoint) binary documentation). It also supports the automated call on POTSDAM's GFZRNX tool for the extraction of metadata. It supports the automated plotting of data, generating scripts for plotting in the AutoCAD environment, data output in Google Earth kml format, and generating summary reports for analysis. It supports RINEX3 and Standard Product 3 orbit (SP3) file reading and conversion to CSV format. GPM is essentially an application program interface for running forty-two geodesy-related functions, which also supports multipath and SNR analysis from RINEX3 and SP3 file ingestion, as well as PPP and PPK analysis of GipsyX and GrafNav solution files. Table 4.2 lists and briefly describes the function classes in GPM. It has a GUI for implementing unattended operations. Almost all the main functions are callable from the MATLAB command line. There is an ambitious goal to evolve GPM into a complete GNSS processing software in the future. More details

about GPM's main features are in the following sub-sections and brief descriptions of each function in Table B.1 of **APPENDIX B**.

Table 4.2 *GPM function classification and description*

Function Classification	**Number of functions**	**Description**
DataMatching	6	Matches time variable for two and up to seven GNSS data files
FileReaders	2	Reads CSRS PPP and GrafNav output files
Geodesy	20	Handles geodetic computations, i.e., GNSS calendar computation (GPS week, day of the year), curvilinear coordinates to projected UTM grid for any zone, UTC past year 2000 in seconds to civil time, Cartesian coordinates to curvilinear; all geodetic computations are capable of batch processing
GipsyX	28	Writes scripts for unattended processing of GipsyX in Linux, unattended file management, GipsyX output file ingestion, data analysis, and time series and histogram plotting of residuals
GrafNav	8	Statistics, data filter, plotting, report, AutoCAD scripting of analyzed GrafNav data; the AutoCAD scripts enable automated plotting in an AutoCAD environment
GrafNavBinary	3	Translates GrafNav binary file and calculates statistics
Maths	2	Interpolates polynomials based on Lagrange Interpolation algorithm
NMEA	3	Reads standard and proprietary NMEA strings

Function Classification	**Number of functions**	**Description**
Orbits	13	Reads SP3 files, identifies gaps and known positions on either side of data gaps, passes those to the main Lagrange interpolation routine, sorts GNSS orbital positions into their constellations, and individual SVs a single structured variable, and plots orbits. Other routines in the Orbit group ingest GipsyX orbit format (pos_goa) and retrieves PRN corresponding to active SVN from the GipsyX constellation database, compares orbits between MGEX ACs
ProductsDownload	2	Automated download of all MGEX products from the CDDIS repository. It is GUI-ready for downloading products from any other repository
Rinex3Jinex	14	Reads RINEX 3 data and sorts into constellations and individual SV. Identifies all signal types, frequency band per signal from a database built according to RINEX3 documentation, extracts SNR per satellite and groups those in a plot per constellation, estimates code-multipath for different pairings of hardware
Statistics	1	Calculates 95^{th} percentile of ordered statistics

4.2.2.1 GPM Scripting Feature

GipsyX is 100% command-line operated. It allows PPP processing for a single station per time series, making it somewhat challenging to handle multiple datasets for multiple sessions. Thus, GPM simplifies the operating procedure with its GUI features. The GUI for GPM (Figure 4.1) is implemented in a single form that hosts the main tools for triggering project directories' automated creation at a chosen path. Once the antenna, receiver, antenna dynamics, a CORS or local station, observation date of a session are defined in the interface, and the scripting feature is activated, GMP will generate eleven Linux-based scripts that call GipsyX PPP's processing commands.

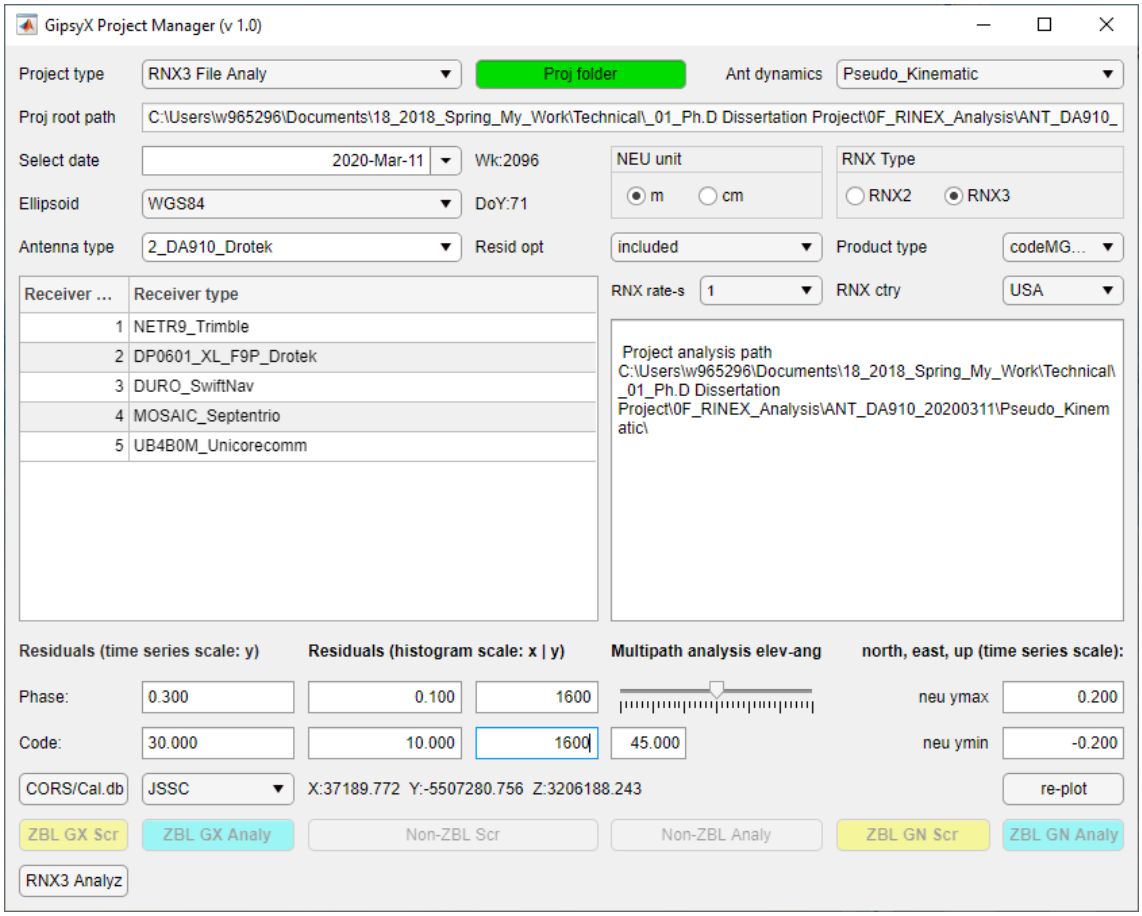

Figure 4.1 *GUI for GPM*

One of the Linux-based scripts calls GipsyX igs2GipsyX.py module for product download and conversion to GipsyX native format, including the clock wide-lane phase bias (WLPB). Eight of the scripts generated by GPM are glued together in a “master” script callable from the Linux shell to handle RINEX data conversion to GipsyX native format, PPP processing, a graphical preview of results, and data archiving in a folder that is automatically named to reflect the session’s attributes for onward analysis in GPM. The antenna and receiver types are customizable to include new hardware or a complete replacement of the default hardware database via a text file.

GPM scripting feature prepares callable shell scripts that support PPP processing of RINEX2 and RINEX3 files in GipsyX. The “RNX-ctry” tool manages a database of country codes for all IGS Multi-GNSS Experiment (MGEX) observation files, thus making it possible to auto-process RINEX file for any IGS MGEX station. The “Product-type” tool prepares shell scripts for product downloads in GipsyX using a database containing nineteen resource locators. The current GPM version supports direct product download within the GPM environment from two of those resource locators, namely, CODE and JAXA IGS Analysis Center (AC). See Appendix B.2 for more on how GPM GUI works.

4.2.2.2 GPM RINEX3 Feature

Currently, GPM supports only the ingestion of RINEX3 files. The GPM RINEX3 feature runs 25 different functions in the background. The software self-navigates the different paths hosting the RINEX files for different LM3GNSS observations, ingests data in succession for processing, and dumps the RINEX data in a CSV format named “JINEX.” Once the RINEX data is ingested, GPM sorts that into different constellations

and space vehicles (SV) based on pseudo-random noise (PRN) number in a single structured variable.

GPM RINEX3 functions are meticulously written, such that signal types and modulations for all global constellations are correctly identified. The RINEX3 functionality extracts and plots SNR as a function of time. GPM extracts the station global Cartesian coordinates in the header of a RINEX3 file, transforms it to local Cartesian using the geodesy tools highlighted in Table 4.6, including the computations of azimuth and elevation of all SVs in view. APPENDIX B (Table B.1) lists and describes all the RINEX3 functions in GPM.

4.2.2.3 GPM Orbit Feature

GPM ingests SP3 files and also dumps the data as an exported CSV file for user review. Similar to the RINEX3 feature of GPM, the orbit feature sorts the data into a structured variable. That allows for easy reference to any SV in any constellation at any epoch. The global Cartesian coordinates of the SV are transformed into local Cartesian and stored in a structured variable for onward transmission to the Lagrange interpolation routine.

4.2.2.4 GPM Coordinate Transformation Feature

The coordinate transformation from geodetic earth-centered to the topocentric system, as implemented in GPM's geodetic computations, follows the right-handed system's basic formula. The relationship between the local (u, v, w) and global (x, y, z) Cartesian coordinates of any point, related by an origin on an ellipsoid normal and the geodetic local meridian plane passing through that origin on an ellipsoid, is given as $(u, v, w)^T = E(\Delta x, \Delta y, \Delta z)^T$ where E is the rotation matrix given in Equation (1) as:

$$E = \begin{pmatrix} -\sin\lambda & +\cos\lambda & 0 \\ -\sin\varphi\cos\lambda & -\sin\varphi\sin\lambda & +\cos\varphi \\ +\cos\varphi\cos\lambda & +\cos\varphi\sin\lambda & +\sin\varphi \end{pmatrix} \quad (1)$$

GPM also implements coordinate transformations from the geodetic curvilinear to grid coordinates of the Universal Transverse Mercator (UTM) projection system. This transformation feature moves the latitude and longitude coordinates provided by the tdp2llh.py module in GipsyX and the Cartesian coordinates of CORS or a local station defined by CORS/Cal.db tool of GPM to the easting and northing equivalent during LM3GNSS data analysis. All the coordinate transformation features are callable in the MATLAB command window for either batch or single point processing.

4.2.2.5 GPM Lagrange Interpolation Feature

Lagrange interpolation algorithm (Hofmann-Wellenhof et al., 2007; Kreyszig et al., 2011; Stroud & Booth, 2003; Teunissen & Montenbruck, 2017), as implemented in GPM, use eleventh-order polynomials, keeping six consecutive known SV positions on either side of a target orbit gap. The known SVs positions do not include any of the previously interpolated points in GPM's computations. The implementation is conceptualized as a moving window on the orbit. The assessment of GPM's orbit interpolation, as discussed in Section 4.2.2.6, shows it is capable of cm-level (1 cm) accuracy, which was sufficient for pseudorange multipath analysis. Besides, Pustoshilov & Tsarev (2017) suggest the uncertainty should be better than 1 cm when using 11th order polynomials for GPS and GLO constellations. The Lagrange interpolating polynomials (l_i) at the desired time (t) for nth-order polynomials, where $i = 0\ldots$ n, and the position vector $\boldsymbol{r}(t)$ are given, respectively, in Equation (2) and Equation (3).

$$l_i(t) = \prod_{\substack{j=0 \\ j \neq i}}^{n} \frac{(t - t_j)}{(t_i - t_j)} \qquad (2)$$

$$\boldsymbol{r}(\boldsymbol{t}) = \sum_{i=0}^{n} \boldsymbol{r_i}\ l_1(t) \qquad (3)$$

4.2.2.6 GPM Interpolation Consistency with GipsyX

This section discusses the orbit interpolation accuracies achievable within the GPM orbit interpolation tool. GPM interpolation accuracy presents a processing challenge in that timestamps and satellite names in GipsyX are different from the standard convention of the SP3 files, which GPM ingests to compute satellite positions, altitude, and azimuth during multipath estimations. Since GipsyX's interpolation output file (also known as satellite-state output file) uses a native file format called "pos_goa," it is necessary to ensure that interpolation output files from GPM and GipsyX are in the same time system.

GipsyX's pos_goa time stamps are referenced to an epoch called J2000GPS (in seconds), and J2000GPS is distinct from the epoch J2000.0. Note that the International Astronomy Union (IAU) Resolution C7 recommends that epoch J2000 be defined at date 2000 January 1.5 (mid-day) Terrestrial Time (Soffel et al., 2003). J2000GPS, as defined by GipsX's documentation, is also distinct from the date 2000 January 1.5 UTC, which GipsyX documentation referred to as J2000UTC. The relationship between J2000GPS and J2000UTC according to GipsyX documentation is J2000GPS = J2000UTC - 13 = 2000-01-01 11:59:47.000 UTC. Recall that GipsyX's pos_goa time stamps are seconds

past J2000GPS. To get seconds past GPS week 0 and second 0, referenced to January 6, 1980, 00:00:00.000, add 630763200; i.e. GPS Time = J2000GPS + 630763200 s.

As mentioned earlier, the GipsyX satellite naming convention in the satellite state output file is different from the standard convention of the SP3 file. In GipsyX, the satellite names refer to the satellite vehicle number (SVN), while SP3 refers to PRN. Both are distinct in that SVN is a unique and continuous numbering system for all SVs that ever exist in the constellation, while PRN is a repeating identification (ID) number for an active satellite. Repeating implies that a PRN becomes the ID for an active SV once a previous SV using the same PRN has reached its end-of-life or decommissioned from service. GipsyX maintains a database providing attributes that allow the conversion between GipsyX and SP3 satellite naming conventions.

A direct comparison of the interpolation results of GPM to the interpolation results of GipsyX provides the GPM interpolation accuracy assessment. Note that GipsyX's interpolation of CODE orbit was the reference for this assessment. Using interpolation of CODE orbits did provide a reference and an overview of orbits' consistency between ACs. In the first set of the assessments (Figure 4.2), both software used CODE's MGEX orbit for GPS week 2092, day 044 (2020-02-13). The results in Figure 4.2are also presented in Table 4.3, which indicates that GPM interpolation achieved 0.008 m consistency for GipsyX at the 95^{th} percentile of the ordered statistics for 3-dimensional distances for all constellations. Note that the scale for Figure 4.2, showing GPM and GipsyX consistency, was chosen deliberately to match the scale for Figure 4.6, showing the inconsistencies of orbits from different MGEX ACs.

Table 4.3 *CODE orbit interpolation with GPM versus GipsyX*

95th percentile	**GPS COD / COD**	**GAL COD / COD**	**GLO COD / COD**	**BDS COD / COD**
dX_95% (m)	0.004	0.004	0.004	0.004
dY_95% (m)	0.003	0.003	0.003	0.003
dZ_95% (m)	0.006	0.006	0.006	0.006
3D_95% (m)	0.008	0.008	0.008	0.008

GPM versus GipsyX interpolation of the up vector shows much tighter consistency for all orbits than the X, Y, vectors – compare Figure 4.3 with Figure 4.4. As shown in Figure 4.3, the orbit differences are an exact match, but at a much larger scale than Figure 4.4, there are consistent differences.

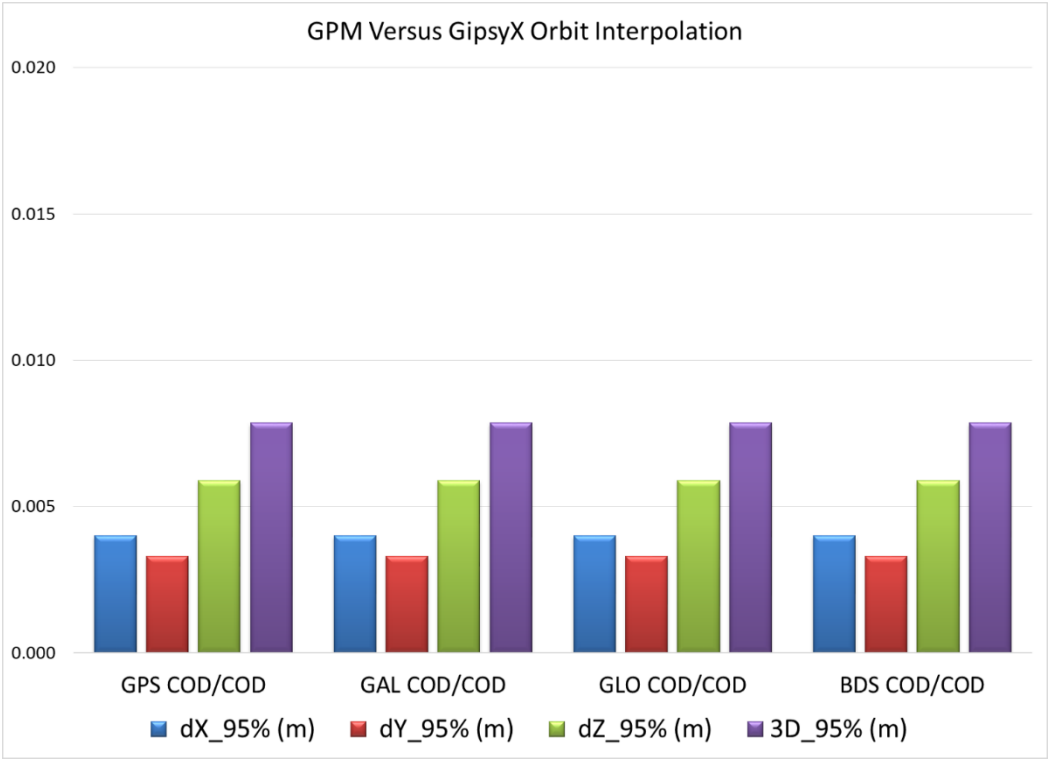

Figure 4.2 *GPM and GipsyX Interpolation Consistency*

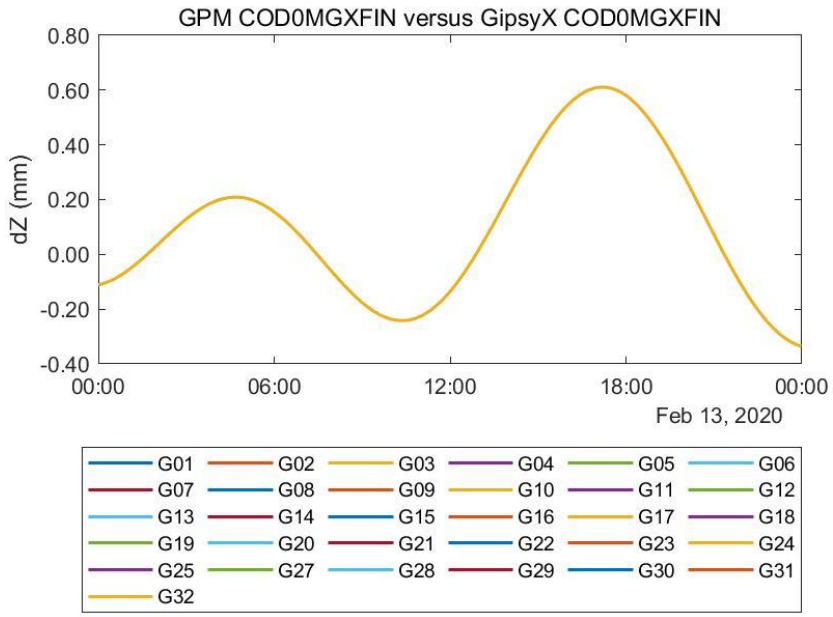

Figure 4.3 *GPM versus GipsyX interpolation in the Z component*

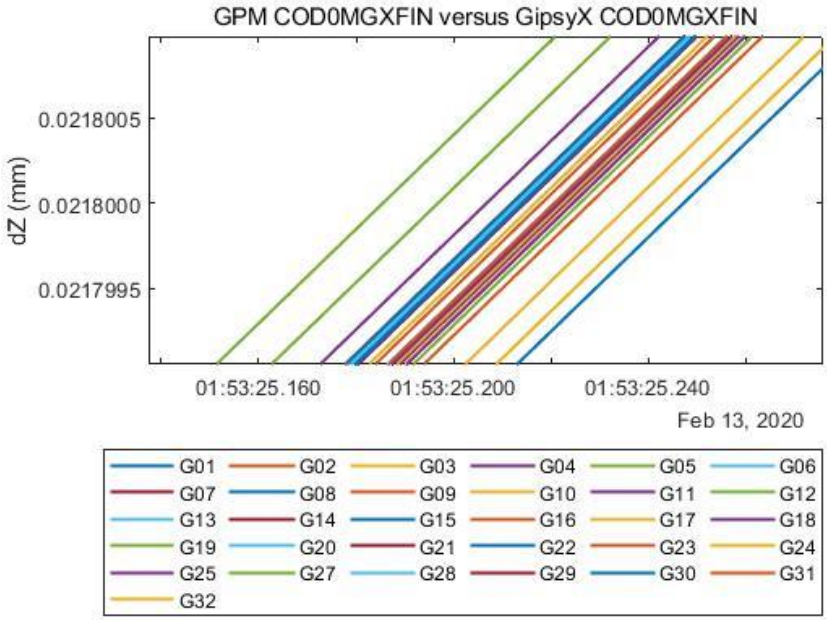

Figure 4.4 *GPM versus GipsyX interpolation in Z component (zoom-in scale)*

4.2.2.7 Inconsistencies Between MGEX Products

In further effort to validate GPM interpolation consistency, this Section compares the GPM's interpolation of orbits from different MGEX ACs relative to GipsyX's interpolation of CODE's orbit for the Year 2020, DOY 044. The results confirm the inconsistencies between products from different ACs, as noted in similar studies (Guo et al., 2017; Kazmierski et al., 2018; Steigenberger et al., 2015; Zhao et al., 2018). Figure 4.6 shows the assessments of GPM interpolations of orbits from CNES, JAXA, and GFZ (see Section 4.4.6 for more information about MGEX ACs) relative to GipsyX's interpolation of CODE. While the GPM versus GipsyX interpolation of CODE orbit is generally less than 0.01 m, the 3D distance consistency at the 95^{th} percentile varies for other ACs and ranges between 0.07 and 0.30 m, depending on the constellation. A snippet of the thirty-nine orbit analysis plots generated in GPM (Figure 4.5) shows the orbit's differences between GPM and GipsyX interpolations. Figure 4.5a confirms the interpolation consistency with some excursions at the day boundaries. Those excursions are edge-effects related to using a day file for the interpolation. The future update to GPM interpolation will use three consecutive orbits for interpolation to minimize day-boundary errors. Figure 4.5b indicates the bias between GFZ and CODE BDS orbits.

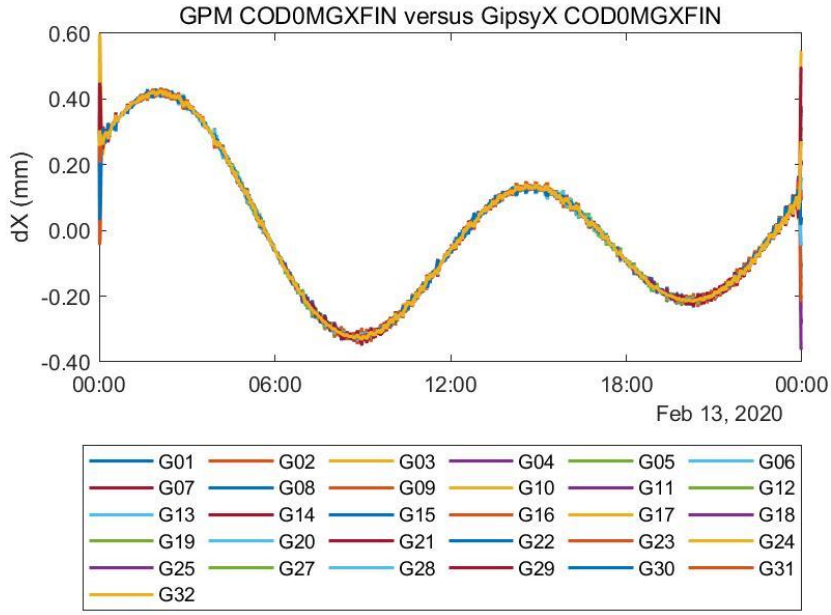

Figure 4.5a *dx GPS*

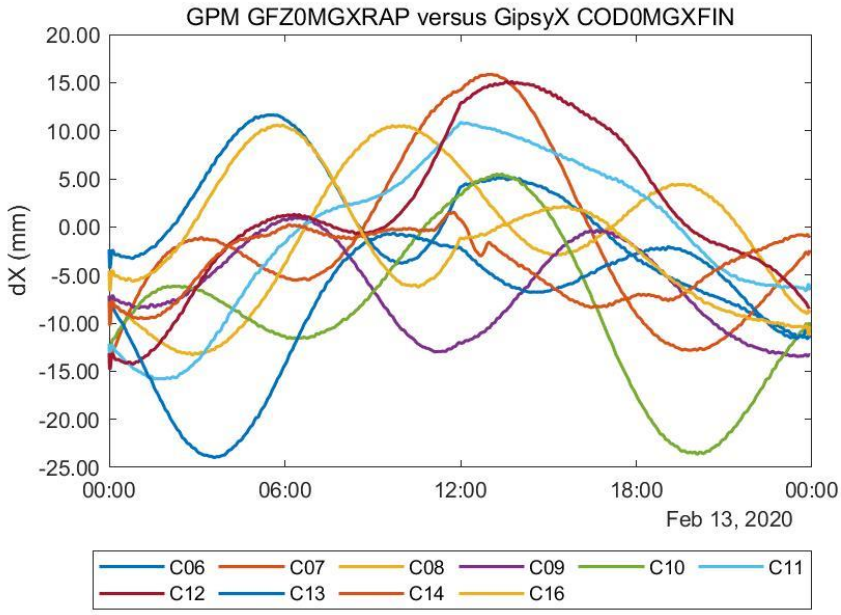

Figure 4.5b *dX BDS*

Figure 4.5 *GPM versus GipsyX interpolation results*

GPM's results indicate between-AC inconsistencies, as reported in previous MGEX orbit assessments. For instance, Guo et al., 2017 report that MGEX orbit consistency ranges between 0.1 - 0.25 m for GAL, 0.1 - 0.2 m for BDS medium earth orbit (MEO) SVs, 0.2 - 0.3 m for BDS inclined geosynchronous orbit (IGSO) SVs, and 0.2 - 0.4 m for QZSS. Their study assessed the GAL orbits from other ACs relative to CODE and observed that 3D RMS GFZ and CNES were 0.215 and 0.23 m, respectively. GPM interpolations for GAL orbits in similar comparison shows 3D distance at the 95^{th} percent ordered statistics did not exceed 0.07 and 0.10 m. Similarly, Guo et al. (2016) validated 2014 GPS orbits from IGS MGEX ACs, relative to IGS final (operational) products, and noted that WUM orbits have the best consistency, showing better stability and smallest RMS values (1D RMS: 0.0115 m). The authors ranked GFZ (old product ID: GBM/GFM) and COD (old ID: COM) next to WUM and classified JAX (old ID: QFZ) as the worst. Steigenberger et al. (2015) also report that individual ACs have orbit consistency between 0.05 – 0.3 m. While GPM's orbit interpolation validation using a single-day orbit may not be sufficient to determine relative orbit performance between MGEX ACs, the results, compared to previous orbit accuracy, are sufficient to validate the GPM interpolation technique.

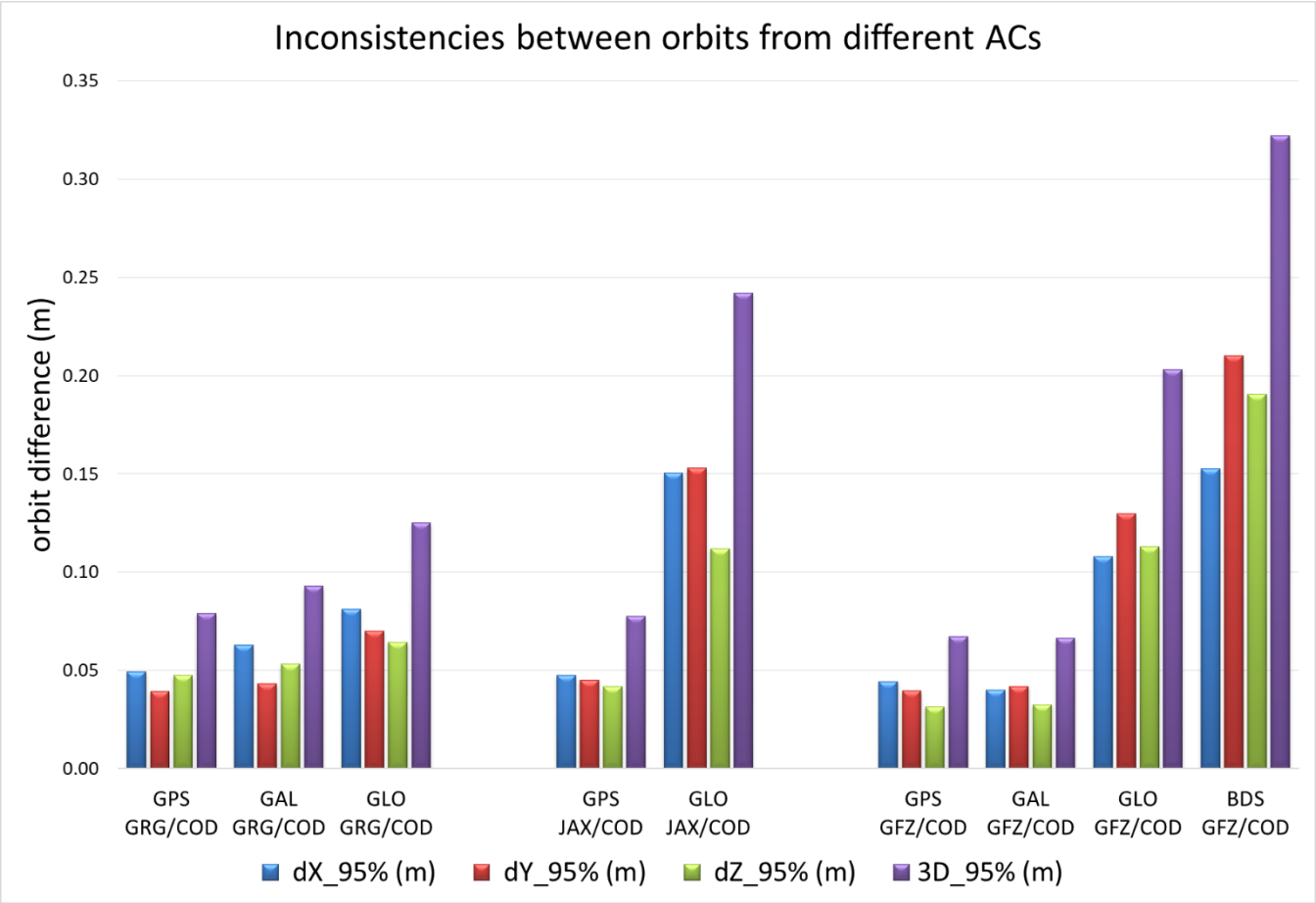

Figure 4.6 *Comparing interpolations of GPM to GipsyX*

A comparison of GPM and GipsyX interpolation using CODE orbit as reference: the SP3 file prefixes for the respective ACs are COD (CODE), GRG (CNES), JAX (JAXA), and GFZ (GFZ). For example, CNES versus CODE, in the legend, is written as GRG/COD.

4.2.3 GrafNav

NovAtel's Waypoint Products Group developed GrafNav as one of its commercial software portfolios for static and kinematic data processing in PPP and PPK strategies. In April 2020, Hexagon-Novatel released GrafNav version 8.9.2428, following the first release of 8.9 announced in January 2020. GrafNav version 8.9 supports all the four global constellations and third frequency bands during PPP and PPK processing. PPK processing with GrafNav can use up to 40 satellites. Its new PPP-AR engine supports NovAtel receivers with the TerraStar-NRT service subscription. In this dissertation, all the PPK and kinematic PPP processing were performed in GrafNav version 8.9.

4.2.4 RINEX Tool

GNSS file conversion from proprietary to RINEX format required hardware-specific conversion tools for some receivers. Table 4.3 lists the RINEX tools used in this dissertation. Post-RINEX conversion with the hardware-specific tool also required editing the station name and apriori station coordinates to support the smooth running of GipsyX's PPP engine. Other manipulations such as splicing, splitting, and file renaming provided consistency for record-keeping. GipsyX is very strict with data conventions and crashes at the slightest inconsistency it encounters. Data splitting was necessary for RINEX files larger than 24 hours; hence the GFZRNX became the "master" RINEX tool for handling those processes. While RTKCONV from RTKLIB claims to support the RINEX conversion of Swift Navigation data, a conversion attempt was unsuccessful. Hence, the conversion of Swift Navigation's native to RINEX format used the command-line sbp2rinex tool. The conversion from Septentrio's native format to RINEX was

successful using RTKCONV. However, the command-line sbf2rinex tool was more efficient for multiple file processing.

Table 4.4 *Receiver and RINEX tools*

Receiver	**RINEX tool**
NetR9	Trimble
ZED-F9P (ublox)	RTKCONV from RTKLIB
Duro	sbp2rinex
Mosaic	SBF converter / sbf2rinex
UB4B0M	Converter 3.0.6

4.3 USMCS Static Solution

The establishment of USMCS achieved a positional accuracy comparable to the NGS CORSs in that the uncertainties are 1 mm or better (one sigma) in all components, using the beta version of the Online Positioning User Service (OPUS) Project of NGS. Access to the software is web-based, and it is open only to trained and registered users. OPUS Project's processing strategy is based on double-differencing, relative to a network of NGS CORS. With the product identification string and manager keyword created as required by the software standard operating procedure, 30-second 24-hour static files collected between 2020-01-01 and 2020-01-09 were uploaded via the publicly accessible OPUS (different from OPUS Project). Only GPS observables are included in the solution since the OPUS Project does not support non-GPS data types. APPENDIX D provides further details on the network adjustment of USMCS coordinates which includes, session information (Table D.1), Baseline information (Table D.2), a priori coordinate shifts (Table D.3), USMCS coordinates in Cartesian (Table D.4), and grid coordinates (Table D.5).

4.4 SK-PPP Processing Strategy

In GipsyX, it was necessary to make modifications to ANTEX, receiver file, as well as the Global and Station Information branch of GipsyX's input tree. Additionally, station-dependent information provided in the ocean loading file improved the LM3GNSS PPP solutions. It was noted that an average of 2 hr. 15 min of processing time is required for a 24-hour-1-Hz observation file when using the ionospheric-free strategy and computer hardware available for this dissertation; VMWare Workstation 15 (a virtual machine running CentOS), allotted 8 GB RAM, and 120 GB HDD of the host machine DELL (Intel(R) Core(TM)i7-7700 CPU @ 3.60GHz, 64.0 GB RAM), running Windows.

4.4.1 Antenna Calibration Files

LM3GNSS PPP with GipsyX required modifications to default files, namely, antenna, receiver, ocean-loading, and input tree (an indentation-sensitive file). As classified earlier in Section 3.1, DA910 and GPS500 are uncalibrated antennas since their PCO and PCV pattern are unavailable either in IGS or NGS ANTEX database. The cloning, using the default ANTEX files for antenna CHCA220GR from China HuaCe Technology Co. Ltd (available on the NGS website) offered a means of mitigating the uncertainties that would, otherwise, propagate into the solutions.

Cloning implies replacing the published PCOs for CHCA220GR with the manufacturers' values for the uncalibrated antennas, leaving the PSV unchanged. The justification for selecting the CHCA220GR ANTEX file is that its PCO, on the GPS L1 frequency band, is about 1.6 cm longer in the vertical component than the uncalibrated antennas. Table 4.4 lists the published PCOs for CHCA220GR and the manufacturer's PCOs inscribed on the uncalibrated antennas.

Table 4.5 *CHCA220GR ANTEX PCOs versus DA910 and GPS500 PCOs*

Antenna	GPS L1 North (mm)	GPS L1 East (mm)	GPS L1 Up (mm)
CHCA220GR	2.56	-1.33	62.24
DA910	0.86	-0.83	46.00
GPS500	0.36	-0.93	57.64

Though the PCV pattern for the CHCA220GR ANTEX file and the uncalibrated antennas may be dissimilar, the ANTEX cloning, *particularly with the PCO modification*, yields better PPP results than a solution with a zero PCO file. Figure 4.7 shows the improvement when using a cloned ANTEX as opposed to using a zero-PCO. The average improvements in the vertical positioning for DA910 antenna (Figure 4.7a) and GPS500 antenna (Figure 4.7b) are, respectively, 0.062 and 0.041 m. There are insignificant differences in the easting and northing components between using a cloned and a zero-PCO for the uncalibrated antennas (see APPENDIX F).

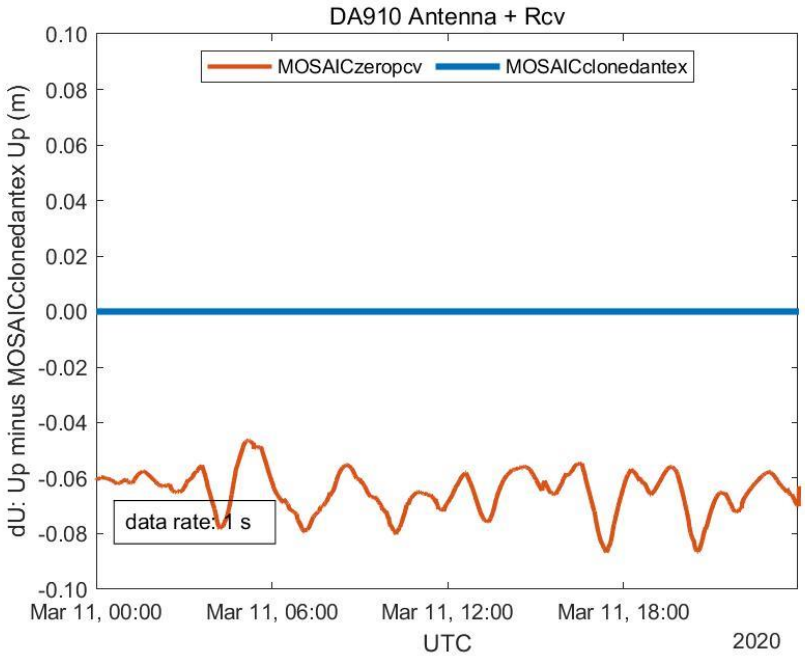

Figure 4.7a

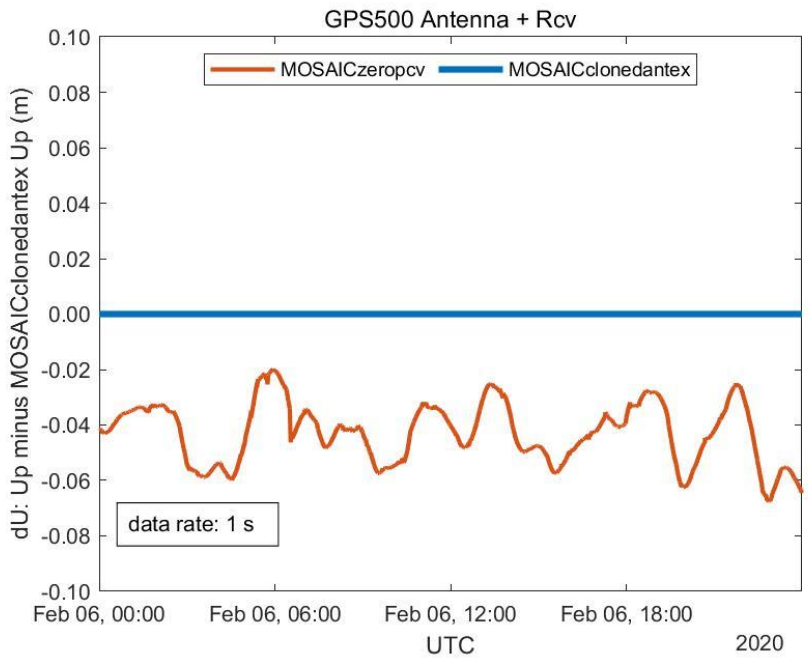

Figure 4.7b

Figure 4.7 *Cloned ANTEX and zero-PCO*

The blue line represents the solutions with cloned ANTEX, while the red line represents the solution with zero-PCO.

4.4.2 Receiver File

In this dissertation, the LM3GNSS receivers are classified as non-IGS. It implies the receivers do not exist in the GipsyX database as retrievable from the "goa_var" repository of the software. One step towards successfully processing the LM3GNSS data using GipsyX is the inclusion of the LM3GNSS receiver names and attributes in the database. That must be consistent with the names in the RINEX header of the observation files since GipsyX is very strict and will abort processing at the slightest inconsistency it encounters. Table 4.5 lists the receivers and their classification in the GipsyX database.

Table 4.6 *Receiver classification of LM3GNSS in GipsyX*

Receiver Type	C1-P1	Fixtags	IGS
DROTEK DP0601	1	0	0
SWIFTNAV DURO	1	0	0
SEPT MOSAIC	3	1	1
UNICORE UB4B0M	1	0	0

The classification of a receiver in GipsyX, as contained in the database remarks, is based on differential code biases (C1-P1), "fixtags," and "IGS" codes C1-P1 class indicates whether C1 or P1 bias needs to be removed. C1 (C/A) and P1 (unencrypted P-code) are pseudorange measurements on the L1 frequency. For bias classification, a value set to "0" indicates unknown classification; a value set to "1" means code bias corrections are required for C1 and P2; value set to "2" indicates that only C1 is reported and would require a bias correction; value set to "3" means L1, L2, C1, P1, P2 are reported as a consistent set, and would not require further corrections. IGS codes entry "1" or "0" implies a yes or no to indicate whether a receiver is an exact match to strings documented in ftp://ftp.igs.org/pub/station/general/rcvr_ant.tab. The "fixtag" parameter is a redundant classification parameter as the latest version of GipsyX does not require this information but may be relevant for format consistency.

4.4.3 Solid, Pole, and Ocean Modeling

GipsyX PPP engine models solid-tide, pole-tide, and ocean loading, and they are applied to all SK-PPP processing. Modeling the ocean loading at a non-IGS station requires injecting into GipsyX externally generated ocean loading values for such station. The station-specific ocean tide loading (OTL) deformation values were interpolated using SEGAL's software (Bos & Scherneck, 2005). The software is accessible as an online service at the Free OTL Provider webpage (http://holt.oso.chalmers.se/loading/). For LM3GNSS PPP solutions, the OTL grid for USMCS was interpolated from the FES2014 ocean tide model. When OTL correction is switched off (Figure 4.8, left), the systematic error induced by the ocean loading effect reaches an amplitude of 15 cm, within 3 hours, in the vertical component. The plot on the right in Figure 4.8 represents the positioning performance when OTL is switched on. That reinforces the need to apply OTL

corrections when high accuracy positioning becomes critical to a marine application near shore. Further studies on the impact of OTL on nearshore surveys may be warranted.

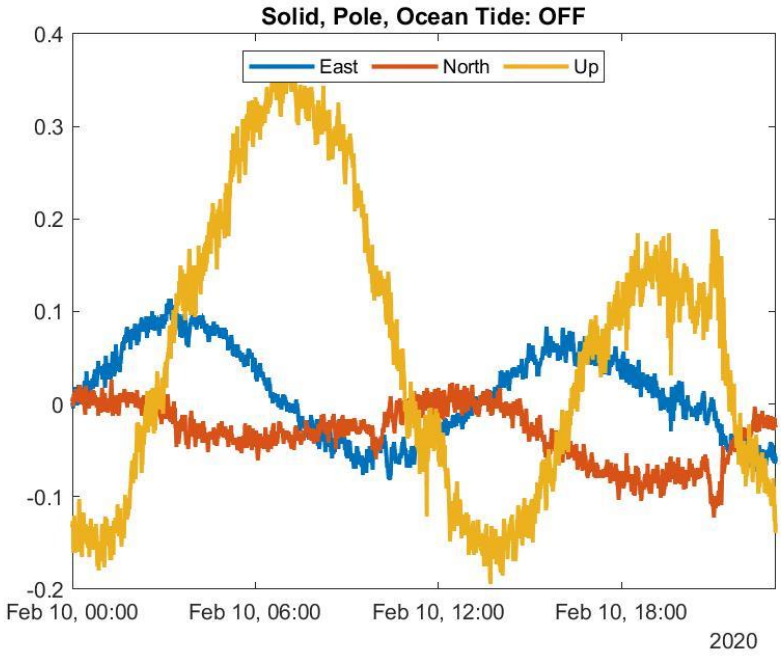

Figure 4.8a Tide modeling turned off

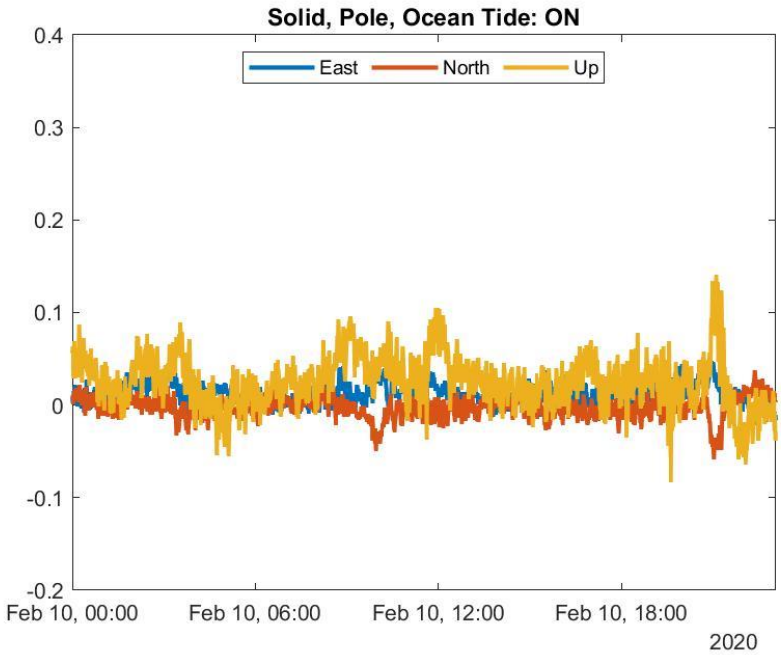

Figure 4.8b Tide modeling turned on

Figure 4.8 *Solid, pole, and ocean tide modeling turned off and on*

4.4.4 Zenith Tropospheric Delay

Since GipsyX is point positioning, the estimation of tropospheric delay is only possible by relying on mapping functions such as the Niel mapping functions (NMF), global mapping function (GMF), Vienna mapping functions 1 (VMF1), global pressure, and temperature 2 (GPT2), according to GipsyX documentation – see Lagler et al., (2013) for a brief discussion on some of those models. Although the SK-PPP processing for this dissertation used the GMF mapping function as apriori input in the PPP filter, future work will investigate whether any comparative advantage exists in choosing a model, especially in PPP-AR processing. Epoch-wise variability in the vertical component required activating the tropospheric zenith delay estimation only as a random-walk while the horizontal tropospheric gradient remained switched off.

4.4.5 Ionospheric-Free Combination

GipsyX PPP strategy applies the ionospheric-free combination to estimate the frequency-dependent path delay. Some LM3GNSS receivers tracked modulations that are different from the commonly tracked modulations. That necessitated the appropriate combination of code and phase data type and the modification to the GipsyX input tree specific to each receiver. Note that GipsyX ionospheric-free configuration in the input tree does not automatically read the datatypes from ingested files. GipsyX input tree is not a one size fits all, suggesting that typical PPP software may require an upgrade to support the datatypes tracked by LM3GNSS receivers. An example of such a software upgrade became evident during a trial processing where a sample data (Swift Navigation Duro with Zephyr3 antenna) was submitted on Oct 11, 2019, to CSRS PPP service of Natural Resources Canada. The kinematic PPP solution report indicates that the CSRS

PPP processing engine rejected 42.97% of the epochs. Figure 4.9 shows a snippet of the report, and the footnote contains the error report, which lists the modulation supported at that time. Another report from CSRS PPP for Zephyr3 plus Duro, 2020, DOY 63, submitted on June 13, 2020, shows their processing engine now supports the following GPS modulations: C2W, C2C, C2L, C2S, and C2X (CSRS PPP, 2020). Whereas the data submitted on June 13, 2020, included all the four global constellations (GPS, GLO, GAL, and BDS), CSRS-PPP returned solutions only for GPS and GLO.

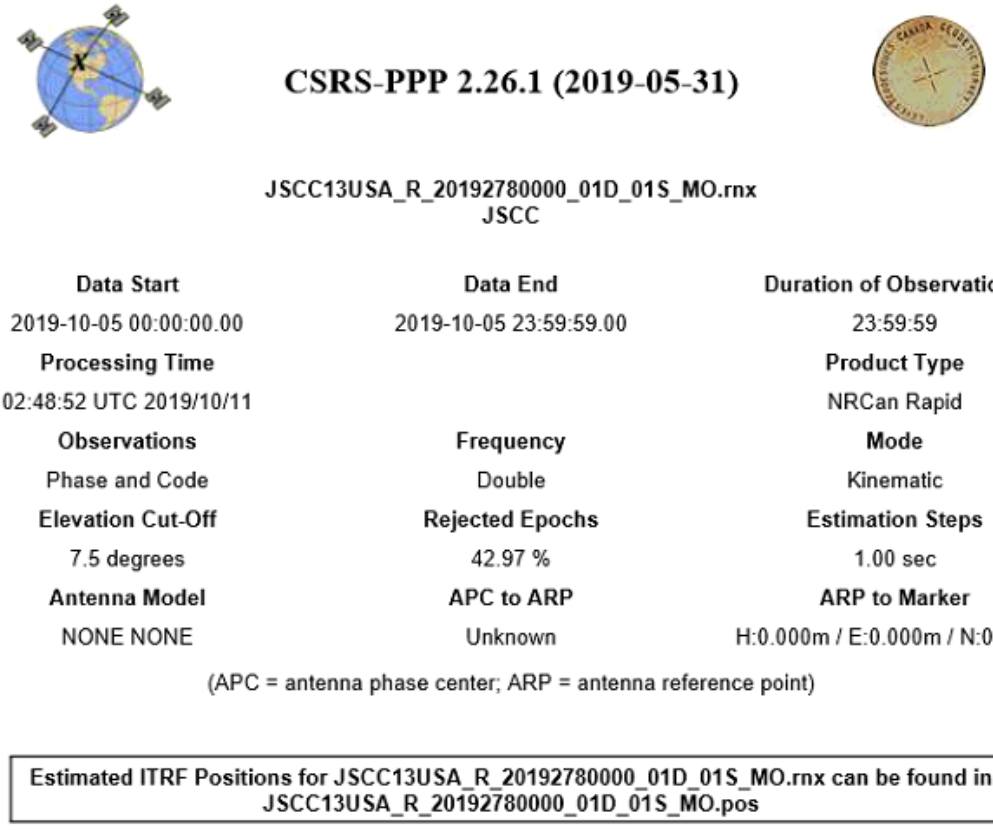

CSRS-PPP 2.26.1 (2019-05-31)

JSCC13USA_R_20192780000_01D_01S_MO.rnx
JSCC

Data Start	Data End	Duration of Observations
2019-10-05 00:00:00.00	2019-10-05 23:59:59.00	23:59:59
Processing Time		**Product Type**
02:48:52 UTC 2019/10/11		NRCan Rapid
Observations	**Frequency**	**Mode**
Phase and Code	Double	Kinematic
Elevation Cut-Off	**Rejected Epochs**	**Estimation Steps**
7.5 degrees	42.97 %	1.00 sec
Antenna Model	**APC to ARP**	**ARP to Marker**
NONE NONE	Unknown	H:0.000m / E:0.000m / N:0.000m

(APC = antenna phase center; ARP = antenna reference point)

Estimated ITRF Positions for JSCC13USA_R_20192780000_01D_01S_MO.rnx can be found in JSCC13USA_R_20192780000_01D_01S_MO.pos

Figure 4.9 *CSRS PPP sample report on Oct 11, 2019*

JSCC13USA_R_20192780000_01D_01S_MO.rnx | Warning: CSRS-PPP does not currently support some or all the GPS signal(s) in your RINEX file. A dual-frequency GLONASS only solution has been processed. The currently supported signals for GPS are C1C L1C C2C L2C C1W L1W C2W L2W and for GLONASS: C1C L1C C2C L2C C1P L1P C2P L2P. Other modulations are planned for support once specific code biases become available. JSCC13USA_R_20192780000_01D_01S_MO.rnx | Warning: Although an antenna record was in the RINEX file, no phase center information could be found in the

IGS/NGS file for the submitted antenna model. Estimated height should be used with caution. Ensure that both the antenna type and the RINEX header record "ANT # / TYPE" is valid.

Table 4.7 shows the list of datatype encountered during this dissertation and the ionospheric-free combinations used in GipsyX for SK-PPP data processing. Comparing the list of constellations and modulations currently supported by CSRS PPP with the modulations listed in Table 4.7, it became evident that CSRS PPP was limited in processing the LM3GNSS dataset. Note that almost any combination of the listed data types is possible in GipsyX, and the phase and code combinations listed here show successful results as presented later in this dissertation.

Table 4.7 *Data types and the ionospheric-free combinations in GipsyX*

Receiver	**Const**	**Data type**								**Phase**	**Code**
NETR9	GPS	C1C	C2W	C2X	C5X	L1C	L2W	L5X		L_1C_2W	C_1C_2W
	GLO	C1C	C1P	C2C	C2P	L1C	L1P	L2C	L2P	L_1C_2P	C_1P_2P
	GAL	C1X	C5X	C7X	C8X	L1X	L5X	L7X	L8X	L_1X_5X	C_1X_5X
	BDS	C2I	C6I	C71	L2II	L6I	L7I			L_2I_6I	C_2I_6I
DP0601	GPS	C1C	C2L	C2L	L1C	L2L				L_1C_2L	C_1P_2L
	GLO	C1C	C1P	C2C	L1C	L2C				L_1C_2C	C_1P_2C
	GAL	C1C	C7Q	L1C	L7Q					L_1C_7Q	C_1C_7Q
	BDS	C2I	C7I	L2I	L7I					L_2I_7I	C_2I_7I
DURO	GPS	C1C	C1P	C2S	L1C	L2S				L_1C_2S	C_1P_2S
	GLO	C1C	C1P	C2C	L1C	L2C				L_1C_2C	C_1P_2C
	GAL	C1B	C7I	L1B	L7I					L_1B_7I	C_1B_7I
	BDS	C2I	C7I	L2I	L7I					L_2I_7I	C_2I_7I
MOSAIC	GPS	C1C	C1P	C2L	C2W	L1C	L2L	L2W		L_1C_2W	C_1P_2W
	GLO	C1C	C1P	C2C	L1C	L2C				L_1C_2C	C_1P_2C
	GAL	C1C	C5Q	C7Q	L1C	L5Q	L7Q			L_1C_5Q	C_1C_5Q
	BDS	C2I	C7I	L2I	L7I					L_2I_7I	C_2I_7I
UB40M	GPS	C1C	C1P	C2W	L1C	L2W				L_1C_2W	C_1P_2W
	GLO	C1C	C1P	C2C	L1C	L2C				L_1C_2C	C_1P_2C
	GAL	C1B	C5Q	C7Q	L1B	L5Q	L7Q			L_1B_5Q	C_1B_5Q
	BDS	C2I	C6I	C7I	L2I	L6I	L7I			L_2I_6I	C_2I_6I

The listed data are based on the RINEX3 convention. The phase combination starts with an "L_," followed by the number and modulation of the first frequency, i.e., "1C_", and ends with the number and modulation of the second frequency, i.e., "2W". Likewise, code combination starts with a "C_," and so on.

4.4.6 Orbit and Clock Products

In this dissertation, PPP processing utilized the IGS MGEX products (Table 4.7), mainly the CODE product, which enabled solutions with all constellations tracked by LM3GNSS receivers. Current MGEX CODE products are available at a faster rate than products from other ACs. It was assumed that the interpolation of products between shorter time steps should yield smaller interpolation errors than the interpolation of products between longer time steps. That explains the preference for CODE products.

Table 4.8 *MGEX ACs and products characteristics*

AC Product ID	Constellations	SP3 min	CLK	SNX	ERPs	BIA
COD0MGXFIN	GPS+GLO+GAL+BDS+QZS	5 / 15	30 s / 5 min	-	x	x
GFZ0MGXRAP	GPS+GLO+GAL+BDS+QZS	15	30 s / 5 min	-	x	x
GRG0MGXFIN	GPS+GLO+GAL	15	30 s	x	-	-
JAX0MGXFIN	GPS+GLO+QZS	5	30 s	x	-	-
SHA0MGXRAP	GPS+GLO+GAL+BDS	15	5 min	-	-	-
TUM0MGXRAP	GAL+BDS+QZS	5	-	-	-	-
WUM0MGXFIN	GPS+GLO+GAL+BDS+QZS	15	5 min	-	x	-

Institution name and product ID: CODE=COD0MGXFIN, GFZ=GFZ0MGXRAP, CNES/CLS=GRG0MGXFIN, JAXA=JAX0MGXFIN, SHAO=SHA0MGXRAP, TUM=TUM0MGXRAP, WUM=WUM0MGXFIN. For full names of ACs, refer to (International GNSS Service, 2020). SP3 is the standard product format for orbit and clock products. CLK is the MGEX's Receiver Independent Exchange (RINEX) format for clock products. SNX is the Solution Independent Exchange (SINEX) format for covariance information. ERP is the International Earth Rotation and Reference Systems Service (IERS) format for Earth rotation parameters (ERP). BIA is the Bias-SINEX format for intersystem biases (Montenbruck et al., 2017). In *Table 4.7*, "x" indicates an available product while "-, "indicates unavailable. CODE, GFZ, and WUM currently provide combined orbit and clock products that include GPS, GLO, GAL, BDS, and QZSS. The combined products from SHAO include GPS, GLO, GAL, and BDS, while the products from CNES/CLS include GPS, GLO, and GAL. The orbit and clock products from JAXA are limited to GPS + QZSS, while the TUM products include only GAL + QZSS.

PPP strategy is essentially a back-substitution positioning technique, in that an arbitrary position is determined from a global model defined by the orbit and clock products, generated from a network of globally distributed stations. It follows that high accuracy results are achievable, provided the user software can replicate the model as accurately as the case when the IGS Analysis Center generated the orbit and clock products. Additional information such as differential code biases (DCB), fractional phase biases, and hardware delays are required to fix PPP ambiguity, making the solution to converge much faster and consistently than otherwise (Choy et al., 2017).

In GipsyX, ambiguity fixing is not a straightforward task. It depends on the product type one intends to use. JPL products include a record of the wide-lane and phase bias estimates (station-specific) needed for ambiguity resolution (Bertiger et al., 2010; Chen et al., 2014). Constraining local phase bias in GipsyX requires the "WLPBLIST" file, which is usually generated while fetching JPL products. The drawback to using JPL's products for LM3GNSS PPP is its limitation to GPS-only or GPS+GLO dataset, as downloadable from the Crustal Dynamics Data Information System (CDDIS) (NASA, 2018). Consequently, the recourse to using the Multi-GNSS Experiment (MGEX) products for LM3GNSS processing in GipsyX. However, that comes with a tradeoff, in that the conversion of MGEX products to GipsyX's native format does not provide the JPL-specific WLPBLIST file for ambiguity fixing. The SK-PPP processing proceeded without the WLPBLIST and achieved accuracies better than 10 cm.

4.5 PPK Processing Strategy

PPK positioning strategy is based on the premise that most of the nuisance parameters, i.e., receiver and satellite clock errors, tropospheric and ionospheric delay, instrument delay, and fractional-phase bias, can be eliminated or minimized in double-differencing. The PPK processing used the dataset from identical pairs of receivers to ensure that the receiver noise and instrument delay are mitigated. All PPK solutions used USMCS coordinates as reference for baseline processing. The GrafNav PPK parameter settings were fine-tuned to reflect the measurement characteristics of LM3GNSS hardware derived from the stochastic model. The validation of LM3GNSS positions was relative to the NetR9 kinematic solutions, as all the receivers tracked GNSS signals in the ZBL setup. It was logical to choose the NetR9 as the reference receiver since this dissertation's primary goal is to determine whether LM3GNSS positioning results approach the geodetic-grade results.

4.6 Stochastic Model

In least-squares adjustment, a stochastic model is the observation weights determined from observation variances. According to Ghilani (2010), p. 182, the proper selection of a stochastic (weighting) model controls the correction magnitude applied to the parameters adjusted in a functional model. For instance, an observation with smaller variance indicates higher precision or higher accuracy (if unbiased), and it will have a higher weight and smaller correction magnitude compared to observations with higher variances. Such a proper weighting model is necessary to deweight observations with large variance magnitudes to ensure overall solution integrity. Since the quality of an observed parameter may vary with time, it follows that a stochastic model could be

adaptive for some applications. In other words, the model is allowed to vary from one interval to the other (Teunissen & Kleusberg, 1998). The two most common stochastic models used in precise GNSS geodesy are white noise and random walk models (Teunissen & Kleusberg, 1998).

This dissertation estimated the stochastics for the LM3GNSS hardware from the SK-PPP post-fit residuals from GipsyX. Since, in an adjustment sense, residuals indicate how well a functional model describes the modeled parameters and the observed quantities, the code and phase residuals become the proxy for stochastic estimation. It is expected that the stochastic model will slightly vary among the LM3GNSS receivers since they have different capabilities as implied by tracking channels, the number of frequencies tracked per constellation, tracking noise, SNR, and multipath mitigation capabilities. In order to infer meaningful a priori stochastics to be ingested into subsequent processing pipelines of both GipsyX and GrafNav, the data collected at USMCS on December 29, 2019, was processed in GipsyX. Table 4.9 summarises the code and phase residuals (95% confidence level). Note that the NetR9 BDS code residual for that solution shows 35 m bias and was, therefore, deleted.

Table 4.9 *Inferring stochastics from code and phase residuals*

	Code - 95%		Unit: m		Phase - 95%		Unit: m	
	GPS	GLO	GAL	BDS	GPS	GLO	GAL	BDS
ZEPHYR3_NETR9	4	4	3		0.03	0.02	0.02	0.03
ZEPHYR3_DP0601	7	4	4	5	0.03	0.03	0.02	0.02
ZEPHYR3_DURO	6	4	4	5	0.03	0.02	0.02	0.02
ZEPHYR3_MOSAIC	6	4	4	7	0.03	0.02	0.02	0.02
ZEPHYR3_UB4B0M	5	4	5		0.03	0.02	0.02	

4.7 Multipath Computations

Pseudorange multipath analysis for different hardware pairings is discussed to assess the hardware-based multipath mitigation capability of the LM3GNSS receivers. Attention is given to code-multipath since carrier-phase multipath is negligible compared to code-multipath. Expressing code multipath as a function of tracked SVs and their elevations required the implementation of some algorithms since the in-house software (GPM) was designed to handle all the data analyses. The geodetic algorithms implemented in GPM were part of the steps required for multipath estimation. The algorithms include: Lagrange interpolation (discussed in Section 0) of SP3, rotation matrix for the transformation of SV coordinates in the global Cartesian system to the local topocentric system at USMCS (Section 4.2.2.4) to enable azimuth and elevation computations for all satellites in view at a 60-s time step. The 60-second rate was chosen to minimize the multipath computation burden in GPM while processing datasets from all the hardware pairings.

Typically, pseudorange multipath is assessed on a single frequency using the geometry- and ionospheric-free multipath combination, popularly described as the code-carrier difference minus twice the ionospheric delay (Bisnath & Langley, 2001; Seepersad & Bisnath, 2015; Teunissen & Montenbruck, 2017). A simple derivation of the mathematical model for characterizing multipath is presented here mainly to show the modeled parameters' relationship. The pseudorange functional model can be written as:

$$\begin{aligned} P_{r,j}^{s}(t) = {} & \rho_r^s(t) + \xi_{r,j}^{s}(t) + c(d_{r,j} - d_j^s) + c(dt_r(t) \\ & - dt^s(t) + \delta t^{rel}(t)) + I_r^s(t) + T_r^s(t) \\ & + MP_{code} + e_{r,j}^{s}(t) \end{aligned} \qquad (4)$$

P is the apparent range otherwise known as pseudorange observable from satellites *s* to receiver *r* as a function of time *t*, ρ is the true-range also known as the geometric range, ξ is line-of-sight-dependent group delay variation, also known as the code-phase pattern, *c* is the speed of light, d_r is receiver code delay or bias, d^s is satellite code bias, the subscript *j* is the frequency identifier, dt_r is the receiver clock offset, dt^s is the satellite clock offset, δt^{rel} is the combined relativistic correction term containing relativistic clock correction and the relativistic signal delay due to space-time curvature, *I* and *T* are respectively, ionospheric and tropospheric delays, MP_{code} is the code-multipath, and e_r^s denotes the receiver code noise and residual. The carrier-phase observable in units of length is given as:

$$\begin{aligned}\varphi_{r,j}^{s}(t) = {} & \rho_r^s(t) + \zeta_{r,j}^{s}(t) + c(\delta_{r,j} - \delta_j^s) + c(dt_r(t) \\ & - dt^s(t) + \delta t^{rel}(t)) - I_r^s(t) + T_r^s(t) \\ & + \lambda_j(\omega_r^s + N_{r,j}^s) + MP_{phase} + \epsilon_{r,j}^s(t)\end{aligned} \qquad (5)$$

Carrier-phase observable φ_r^s, is the sum of the geometric range, phase center offset and variation $\boldsymbol{\zeta}$, instrument phase biases δ, clock correction terms, the ionospheric and tropospheric corrections, phase windup ω, and the unknown integer number of cycles *N* scaled to units of length by the signal wavelength λ, carrier-phase multipath MP_{phase}, and the receiver carrier-phase noise and residual $\boldsymbol{\epsilon}$. Note that the geometric range and clock offsets are the same for both pseudorange and carrier-phase observables. With the time argument dropped for all the time-dependent parameters, the code-carrier difference can be written as:

$$\begin{aligned}P_{r,j}^{s} - \varphi_{r,j}^{s} = {} & \xi_{r,j}^{s} - \zeta_{r,j}^{s} + c(d_{r,j} - d_j^s) - c(\delta_{r,j} \\ & - \delta_j^s) + 2I_r^s - \lambda_j(\omega_r^s + N_{r,j}^s) + e_{r,j}^s \\ & - \epsilon_{r,j}^s + MP_{code} - MP_{phase}\end{aligned} \qquad (6)$$

Rearranging and re-writing the equation gives:

$$MP_{code} - MP_{phase} = P_{r,j}^{s} - \varphi_{r,j}^{s} - 2I_{r}^{s} + \lambda_{j}\left(\omega_{r}^{s} + N_{r,j}^{s}\right) - \xi_{r,j}^{s} + \zeta_{r,j}^{s} - c\left(d_{r,j}^{s} - \delta_{r,j}^{s}\right) - e_{r,j}^{s} + \epsilon_{r,j}^{s} \quad (7)$$

Note that d_{r}^{s} and δ_{r}^{s} are, respectively, the combined satellite-receiver code and the satellite-receiver phase biases. Since carrier-phase multipath is small compared to the pseudorange multipath, the approximate multipath observable can then be written as:

$$MP_{code} \approx P_{r,j}^{s} - \varphi_{r,j}^{s} - 2I_{r}^{s} + \lambda_{j}\left(\omega_{r}^{s} + N_{r,j}^{s}\right) - \xi_{r,j}^{s} + \zeta_{r,j}^{s} - c\left(d_{r,j}^{s} - \delta_{r,j}^{s}\right) - e_{r,j}^{s} + \epsilon_{r,j}^{s} \quad (8)$$

Hence the definition of code-multipath is code-carrier difference minus twice the ionospheric delay. Note that the observable is biased by constant and time-varying terms discussed in the next paragraph.

Under the assumption that no cycle slips occurred, the resulting multipath observables are biased by a set of constant and varying terms for a static receiver. As shown in Equation (8), the constant terms include ambiguity, instrument code, and phase delays, while the magnitude-varying terms include code and phase noise, PCV, and phase wind-up. Using the ionosphere- and geometry-free linear combination, a mathematical model - Equation (9)- analogous to Equation (8) and is derivable as presented in Teunissen & Montenbruck, 2017, pp. 583-592. That model allows for the effective removal of the ionospheric delay via the wide-lane combination. In this dissertation, the pseudorange multipath was estimated using Equation (9) and (10) where $(O_{MP})_{\rho A}$ and $\rho_{r,A}^{s}$ are the multipath observable and pseudorange measurement on carrier frequency A, respectively; $\varphi_{r,A}^{s}$ and $\varphi_{r,B}^{s}$ are carrier-phase measurements on frequencies A and B, respectively;

$$(O_{MP})_{\rho A} = P^s_{r,A} - \varphi^s_{r,A} - 2k(\varphi^s_{r,A} - \varphi^s_{r,B}) \quad (9)$$

where k is:

$$k = \frac{f_B^2}{f_A^2 - f_B^2} \quad (10)$$

The final step in tuning the multipath estimation, as implemented in GPM, is removing biases induced by phase ambiguity. It is known that the phase ambiguity term will change with arc discontinuities as satellites disappear and later appear in the receiver's horizon, the bias removal becomes necessary (Teunissen & Montenbruck, 2017). In GPM, the multipath biases are removed by differencing the observables and its mean on an arc-by-arc basis (Figure 4.10 b). As a means of validating GPM multipath estimation, APPENDIX E (Figure E.1 to Figure E.4) presents a comparison relative to GrafNav's code-carrier difference.

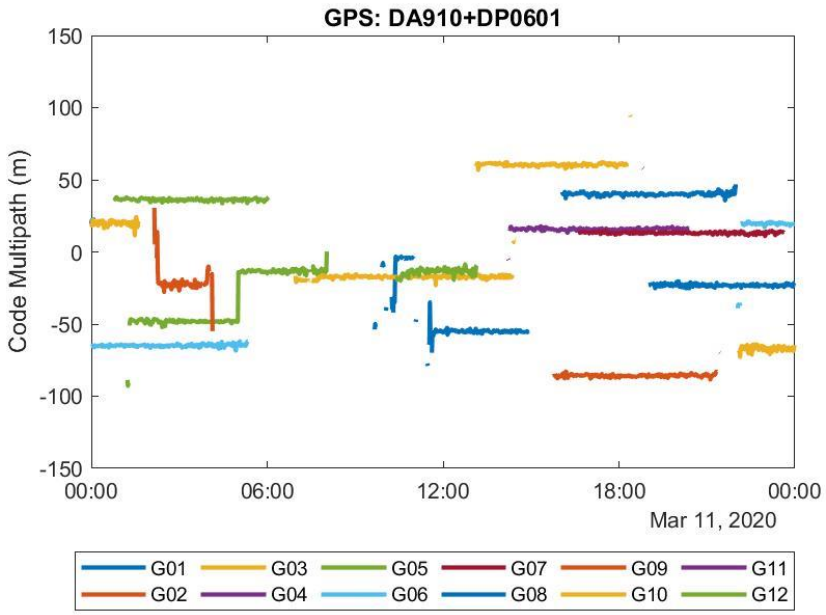

Figure 4.10a Biased code-multipath estimates

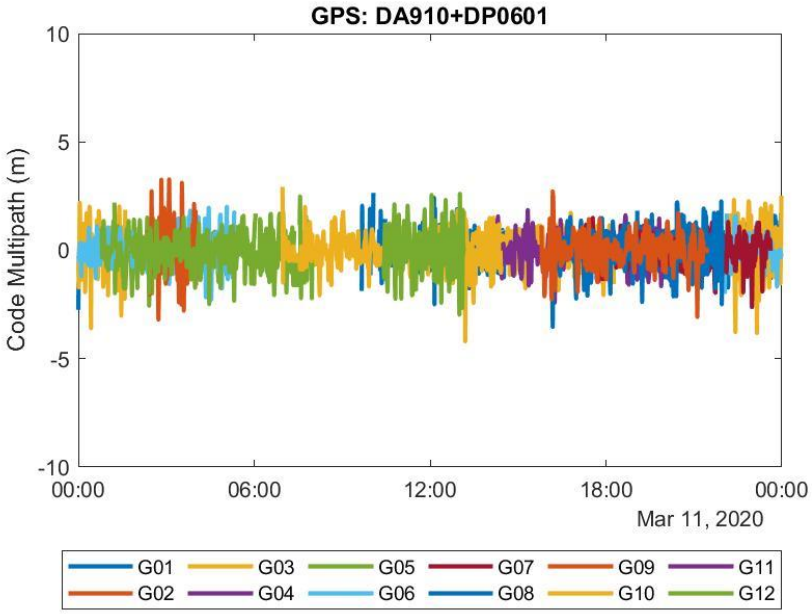

Figure 4.10b Unbiased code-multipath estimates

Figure 4.10 *Biased and unbiased code-multipath estimates using GPM*

CHAPTER V – RESULTS AND ANALYSIS

This chapter presents multipath characterization, SNR characterization, pseudorange, and carrier-phase residuals as data quality metrics. The chapter ends with a processing scenario where the reference data used for PPK processing is GPS and GLO only, and the data rate was 30 s. The results show that a 30-s reference data rate does not yield optimum PPK results, even when the data is at 1 s rate for a rover.

5.1 Results Overview

The following results, analysis, and discussions about LM3GNSS hardware for high accuracy surveys and its prospects for PPK and PPP strategies are based on the 835 figures generated by GPM software-using the Matlab library ({plus three other figures generated in Microsoft Excel} available as an external appendix). The external appendix is available on request (see APPENDIX F for contact details). The external appendix's filing structure is as shown in Figure 5.1 (it follows this dissertation outline).

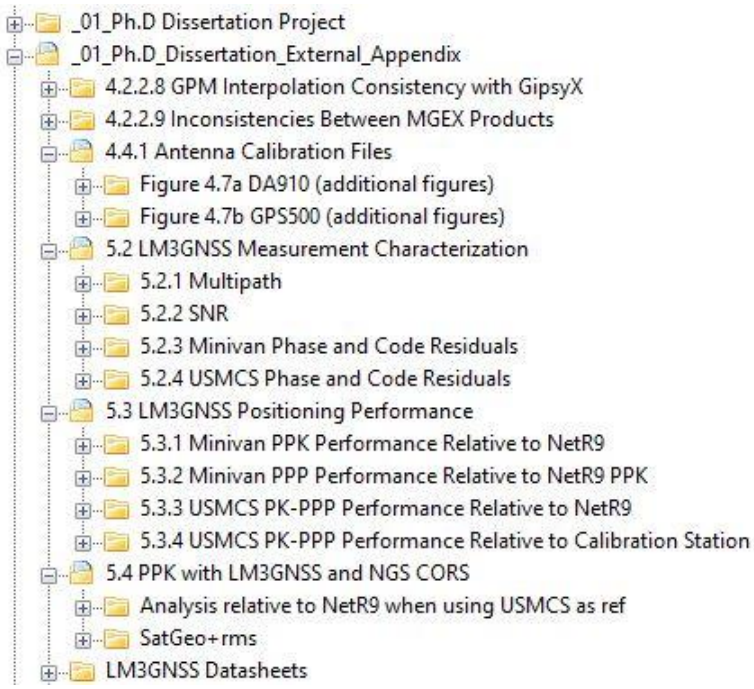

Figure 5.1 *External Appendix*

This chapter presents the PPP and PPK results of the processing scheme shown in Table 5.1. As discussed in CHAPTER IV, this scheme is used to assess PPP and PPK solutions aboard the minivan (rover) while the reference dataset (24-hour) contributes to the SK-PPP processing and analysis. The minivan results simulate the dynamic performance of LM3GNSS hardware aboard a mobile platform while the SK-PPP result simulates the performance on an offshore platform, i.e., offshore buoy.

Table 5.1 *PPK processing scheme*

Date/	Reference		Rover	
Week / DOY	Antenna	Receiver	Antenna	Receiver
Feb 06, 2020 2091 / 37	GPS500	NETR9 MOSAIC UB4B0M DURO DP0601	GPS500	NETR9 MOSAIC UB4B0M DURO DP0601
Feb 10, 2020 2092 / 41	POLANT-X MF	NETR9 MOSAIC UB4B0M DURO DP0601	POLANT-X MF	NETR9 MOSAIC UB4B0M DURO DP0601
Feb 13, 2020 2092 / 44	HXCCSX601A	NETR9 MOSAIC UB4B0M DURO DP0601	HXCCSX601A	NETR9 MOSAIC UB4B0M DURO DP0601
Feb 17, 2020 2093 / 48	ZEPHYR 3	NETR9 MOSAIC UB4B0M DURO DP0601	ZEPHYR 3	NETR9 MOSAIC UB4B0M DURO DP0601
Mar 11, 2020 2096 / 71	DA910	NETR9 MOSAIC UB4B0M DURO DP0601	DA910	NETR9 MOSAIC UB4B0M DURO DP0601

5.2 LM3GNSS Measurement Characterization

Three parameters are used in this dissertation to characterize the measurement performance of LM3GNSS hardware (receivers and antennas). They are SNR, multipath and postfit residuals. One reason for choosing multipath as a performance metric for LMGNSS hardware is because multipath degrades carrier phase measurement quality (Bisnath & Langley, 2001; Seepersad & Bisnath, 2015; Smolyakov et al., 2019) and thus leads to cycle slips if it remains, largely, unmitigated. Also, SNR has been suggested as a weighting function to mitigate multipath. As expected, multipath signals should have relatively reduced signal strength than signals arriving directly at the antenna. Since multipath is elevation-dependent, low-elevation satellites are more susceptible to multipath than high-elevation satellites. Thus, a correlation exists between SNR, multipath, and elevation weighting scheme; thus, SNR is employed in mitigating both multipath and tropospheric delay effects at lower elevations. The postfit residuals suggest how well the parameters are modeled in any parametric equation. Hence, this dissertation expects that the code and phase residuals will mirror each LM3GNSS receiver's performance.

5.2.1 Multipath with Different Patch Antennas

GPM software characterizes code-multipath for all LM3GNSS hardware pairings on GPS and GAL constellations only. The BDS constellation was excluded in the characterization since the receivers rarely tracked more than three SVs. GLO exclusion from the characterization is related to the current version of the GPM software, in that its RINEX3 decoding feature currently supports the constellations using the code division multiple access (CDMA) technique for signal transmission. Since extra care is required to

decode and process frequency division multiple access (FDMA) data, the implementation for GLO is suspended until the future development of the GPM version.

LM3GNSS characterization evaluates code multipath as a function of elevation and time for all satellites per constellation. It involves ninety-six multipath plots (5 antennas x 5 receivers x 2 constellations x {time + elevation plot} — 4 {corrupt files}). That implies a different antenna per ZBL session produced twenty-five elevation-dependent code-multipath characterization plots for GPS constellation only. The characterization plots are color-coded such that the satellites are in different colors. The legend showing SV PRN and their color codes is omitted on the plots to enhance the multipath figures' legibility. Note that the characterization for POLANTXMF+UB4B0M is not available since the RINEX3 data is not retrievable from the raw data.

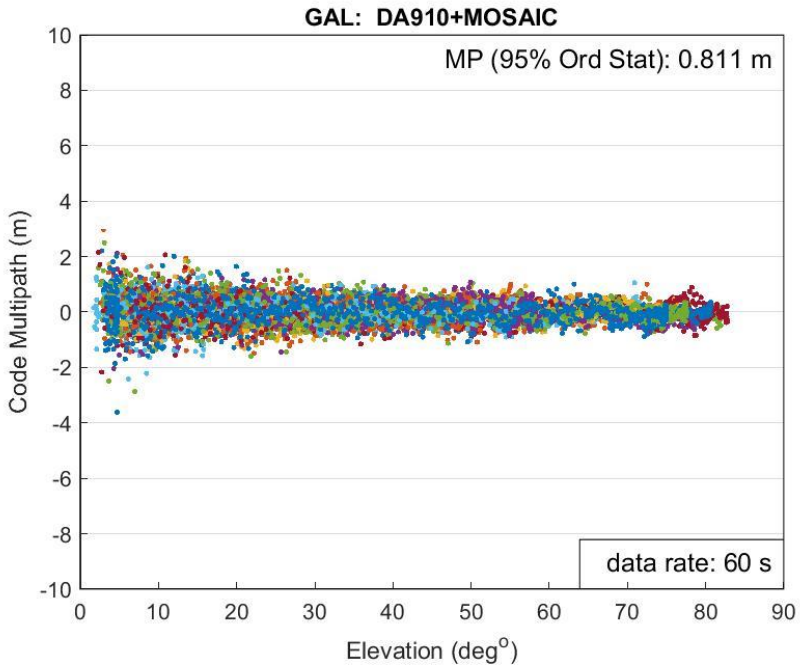

Figure 5.2 *A distinct multipath pattern (DA910 antenna and Mosaic receiver)*
Note the color code indicates different satellites.

The multipath characteristics of LM3GNSS receivers are more evident in the elevation plots than the time-series plots. Hence the focus here is on the elevation-dependent characteristics. As expected, multipath increases as satellite elevations decrease. Some LM3GNSS receivers show broader multipath distribution patterns at lower elevations. Since it is impossible to show all the elevation plots here, information distillation becomes necessary. Therefore, 48 elevation-dependent plots per constellation (recall that POLANT+UB4B0M is unavailable) showing the 95% ordered statistics contributed to the code multipath characterization. Figure 5.2 shows the multipath pattern for GPS500 antenna pairing with the Mosaic receiver. The data rate is 60 s, and the ordered statistics imply that code multipath for this hardware pairing is better than 0.89m 95% of the time.

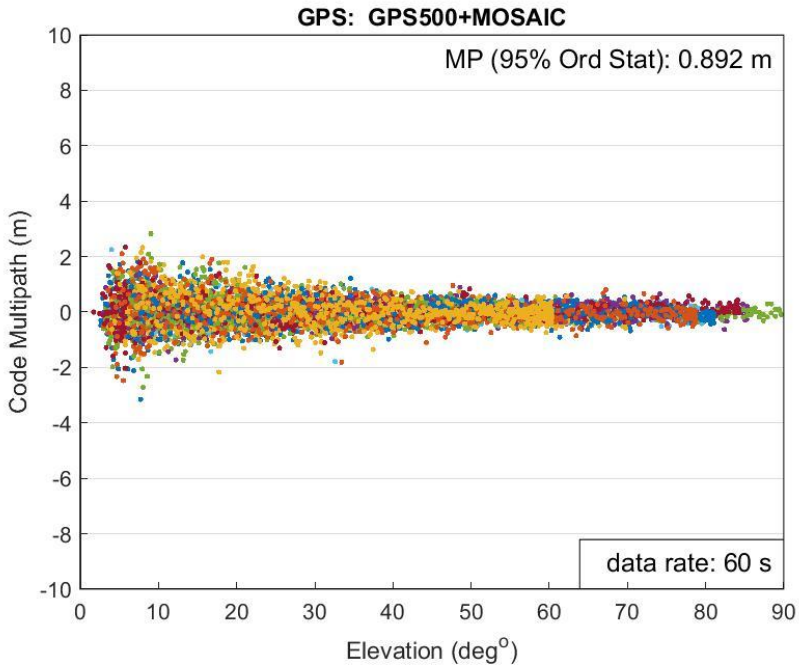

Figure 5.3 *Elevation-dependent code multipath pattern for GPS500 antenna and Mosaic receiver pairing*

Note the color code indicates different satellites.

Figure 5.4 is the code multipath time-series equivalent of Figure 5.3, showing only 12 SVs per plot and a legend to identify the satellites. Prior to the elevation-dependent characterization in Figure 5.3, the biases are induced by the ambiguity term, and cycle slips shown in Figure 5.4a was removed to produce the results in Figure 5.4b.

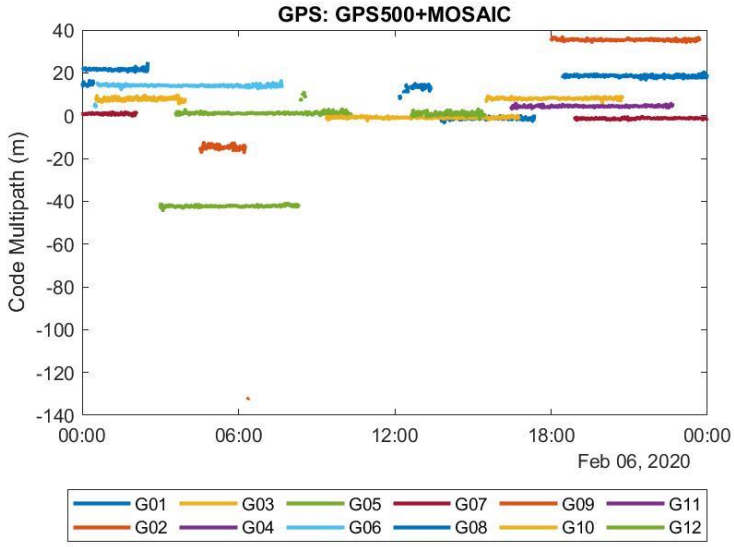

Figure 5.4a

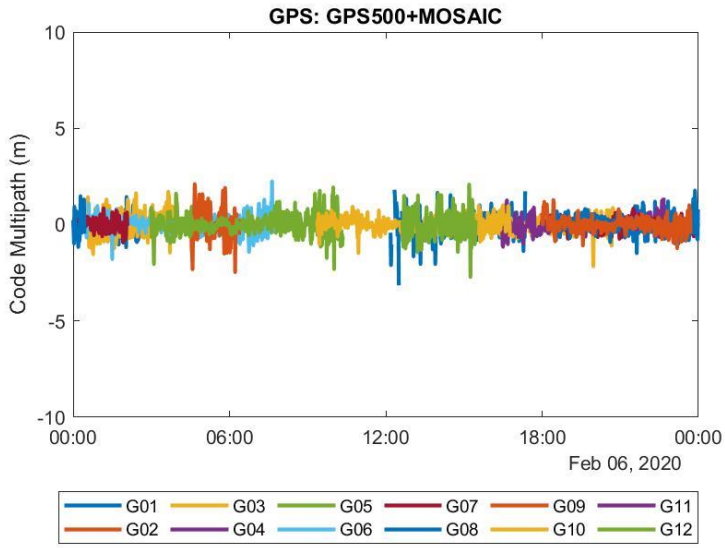

Figure 5.4b

Figure 5.4 *Multipath time-series pattern (GPS500+MOSAIC)*

Figure 5.5 shows a snippet of the characterization when using a native antenna (supplied by the manufacturer) for the respective receiver. The antenna pairings with Septentrio Mosaic and Trimble NetR9 show the least magnitude of code-multipath, and that trend is the same for non-native antenna pairings (see Figure 5.6 and APPENDIX F). Code-multipath is about 1 m for Mosaic and NetR9 on GPS constellation when using native. Unlike the other hardware pairings, Duro and DP0601 receivers show the worst code-multipath in native antenna pairings (approximately 2m). Those receivers rarely show any improvement when paired with non-native antennas. In the GPS constellation, SwiftNav Duro's multipath is often worse in comparison with DP0601's multipath.

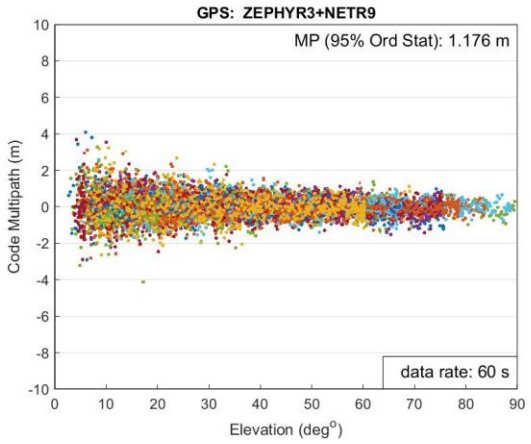

Figure 5.5a

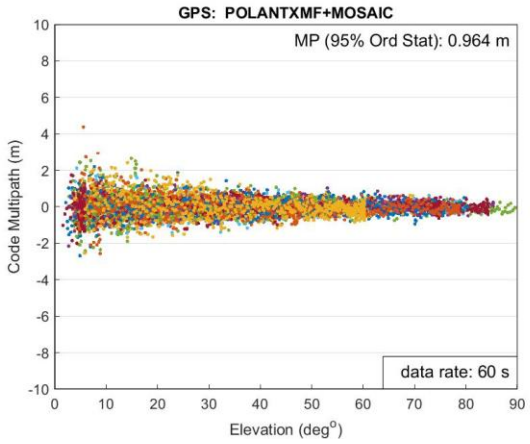

Figure 5.5b

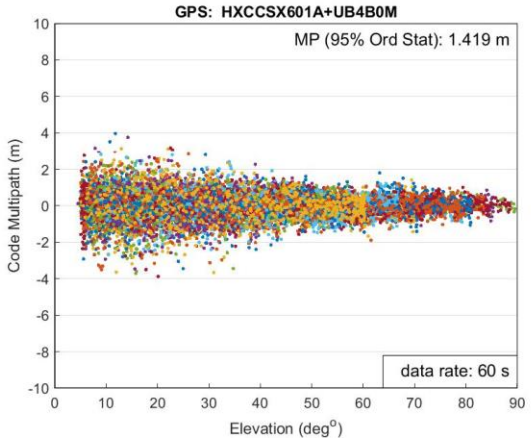

Figure 5.5c

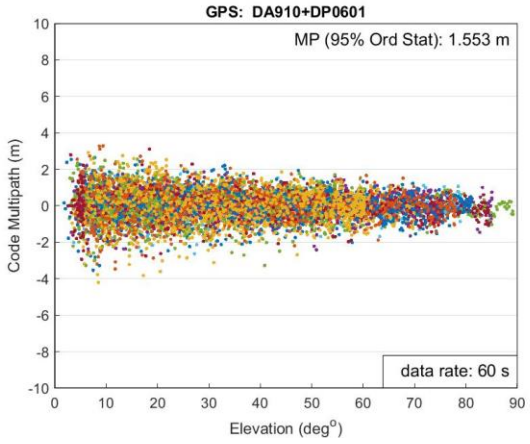

Figure 5.5d

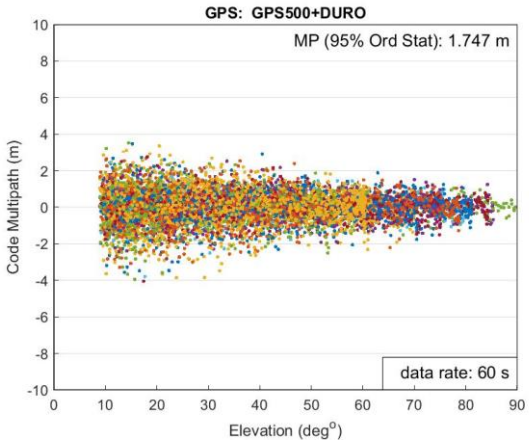

Figure 5.5e

Figure 5.5 *Multipath characterization with respective native antenna*

Note that MP in the figures means multipath. Comparing the native antenna-receiver pairings shows the multipath characterization for the Mosaic's pairing with Polant antenna offers the least noisy multipath characterization.

Figure 5.6 shows the compressed representation of code multipath characterization for all antenna-receiver pairings in both the GPS and the GAL constellations. There are five columns in the figure, and each represents the multipath characterization with a particular antenna pairing. Each node in that figure represents the 95% ordered statistics for a specific antenna-receiver pairing. The following can be summarized from that figure:

1. Code multipath varies between the receivers.
2. The antenna pairings are not so significant to the observable code multipath as the receivers.
3. For any antenna-receiver pairing, the observed code multipath is between 0.70 and 2.29 m at 95% ordered statistics.
4. In GPS and GAL constellations, the smallest code multipath (about 1 m) occurred in the Mosaic and NetR9 receivers.

5. The largest multipath (about 2m) occurred mostly with the Duro and UB4B0M receivers on the GPS and the GAL constellation.
6. In GPS constellation, code multipath is similar (approximately 1.5 m) for both the UB4B0M and the DP601 receivers.
7. Multipath is often smaller in the GAL than the GPS constellation.

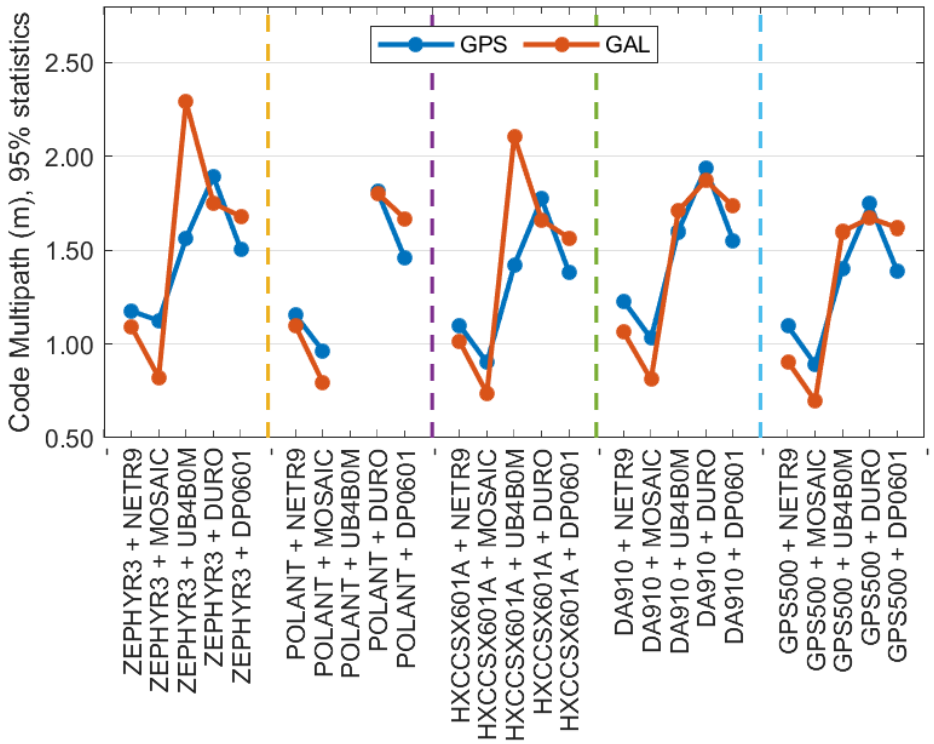

Figure 5.6 *Multipath characterization summary*

Each column in the figure represents different experiments with different antenna pairings. The nodes represent the code multipath's 95% ordered statistics.

The code multipath characterization suggests the highest quality antenna may not necessarily improve the performance of an LM3GNSS receiver if such a receiver does not support receiver-based multipath-mitigation. As such, the signal tracking may be noisy, and it would impact carrier-phase measurements. The characterization also suggests that the code measurement quality for some receivers is better in the GAL

constellation. That indicates higher weights should be assigned to GAL than GPS in MGNSS processing.

5.2.2 SNR with Different Antennas

Similar to the code-multipath characterization discussed in Section 5.2.1, SNR characterization involved ninety-six plots (5 antennas x 5 receivers x [GPS + GLO + {GAL / GPS / GLO+GAL as one composite}]) generated by the GPM software from the RINEX files (collected on five different days) for all hardware pairings. GPM software grouped the SNR characterization plots into GPS-only, GLO-only, GAL-only, and GPS+GLO+GAL. The software also isolates the datatype tracked per receiver-antenna pairings in each plot. For an individual receiver, the SNR values are almost the same for different antenna pairings. Figure 5.7 shows a sample of DP0601's SNR characterization. Irrespective of the antenna pairing for a specific receiver, the signal strength rarely varies. The characterization suggests that the signal strength variation among hardware pairings mainly depends on the constellation, datatypes, signal modulations tracked, and the response to the antenna gain by the receivers.

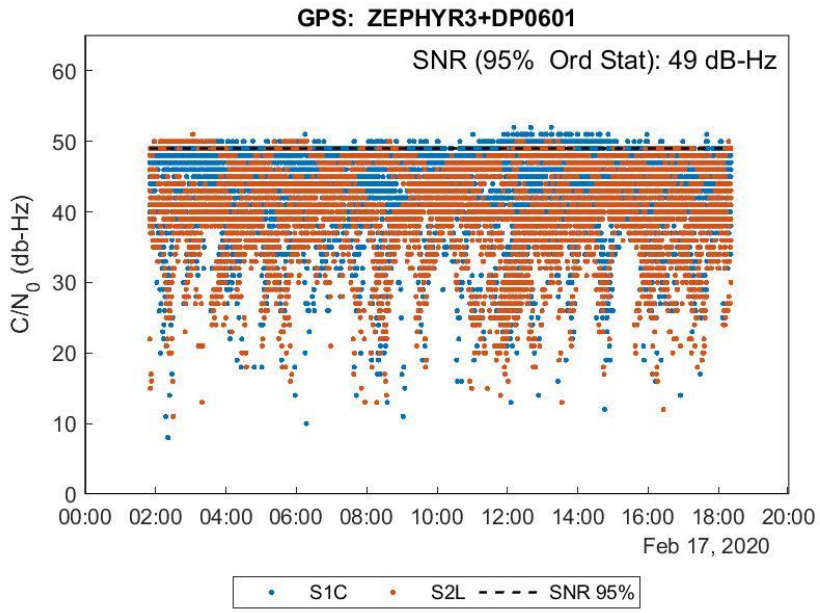

Figure 5.7a SNR with Zephyr3

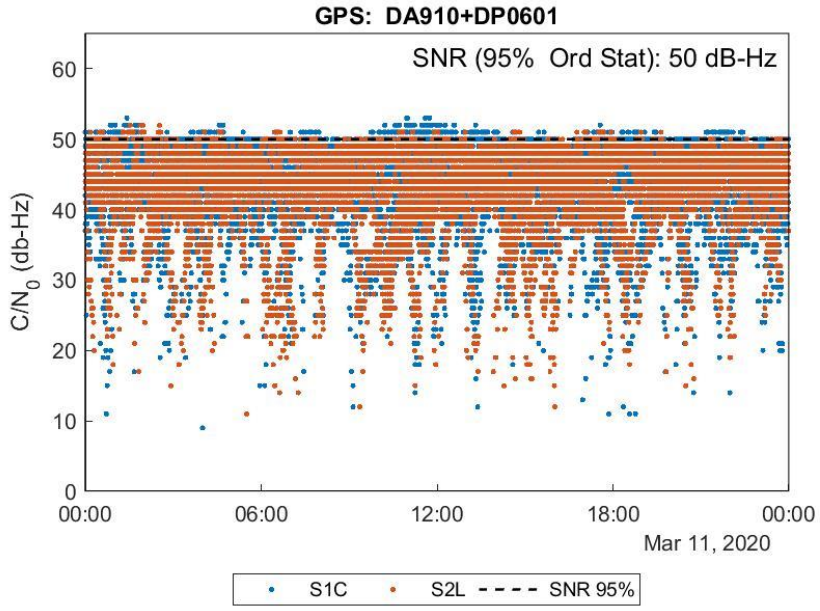

Figure 5.7b SNR with DA910

Figure 5.7 *DP0601 SNR with Zephyr3and DA910 antennas*

Note that the black broken line marks the 95% ordered statistics (Ord Stat). For example, in Figure 5.7b, the signal strength for the DA910 antenna paired with the DP0601 receiver is not better than 50 dB-Hz 95% of the time.

All the antenna pairings with DP0601 receiver show the lowest signal strength (between 49 and 50 dB-Hz), approximately a 5-dB-Hz difference compared to the rest of the receivers in all antenna pairings. The characterization also suggests that DURO and UB4B0M applied SNR filter of about 28 and 25 dB-Hz, respectively, in their tracking solutions (Figure 5.8), since the RINEX data collected at zero-elevation did not show any record below those values. Studies related to ultra-low-cost GNSS processing have shown that a correlation exists between SNR and elevation weighting schemes (Banville et al., 2019; Wanninger & Heßelbarth, 2020), thus suggests the SNR weighting method. Hence, it is presumed that Swift Navigation and Unicore Communications might have implemented SNR masking in the acquisition domain as a data clipping technique to minimize multipath and noise from low-elevation SVs.

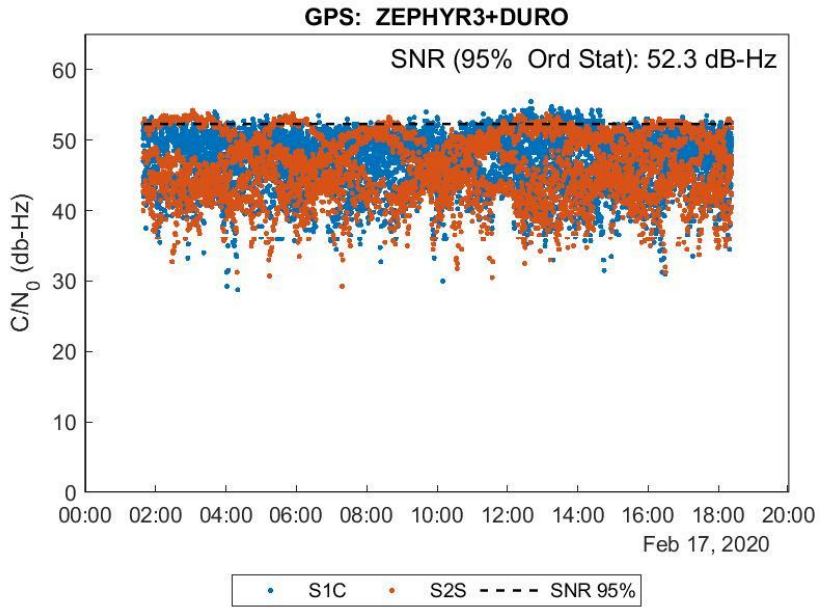

Figure 5.8a Zephyr3 plus Duro

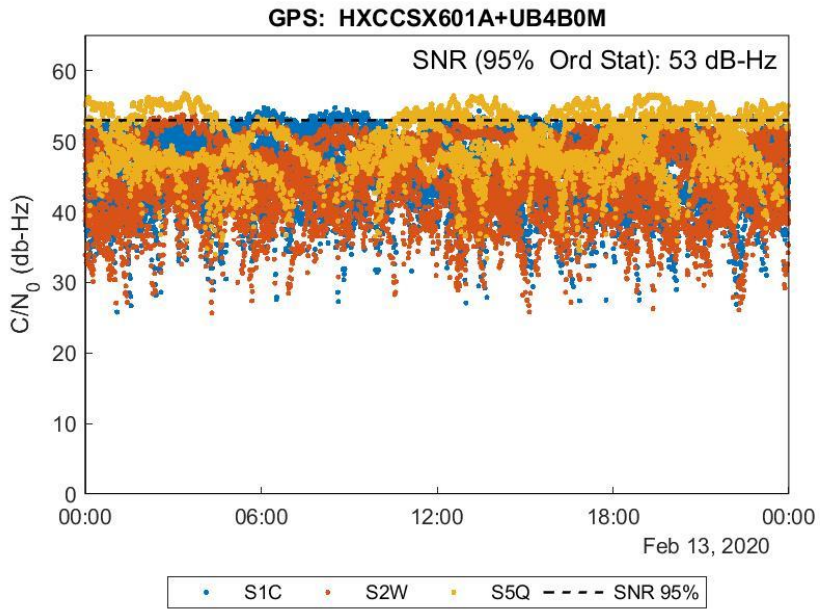

Figure 5.8b HXCCSX601A plus UB4B0M

Figure 5.8 *SNR for Zephyr3 plus Duro and HXCCSX601A plus UB4B0M*

Figure 5.9 shows the SNR characterization summary for all LM3GNSS antenna-receiver pairings in the GPS, GLO, and GAL constellations. Each column represents pairings with different antennas. Overall, SNR varies between the constellations. It is highest in the GLO and lowest in the GPS constellation. It varies between the receivers but not as significant with the antenna pairings for a specific receiver. However, a significant improvement in signal strength is noted with the HXCCSX601A antenna pairings compared to other antennas. It is counter-intuitive to note that signal strength is generally slightly better with low-cost antenna pairings than with the high-grade (Zephyr3) antenna. Figure 5.7 is an example of that trend.

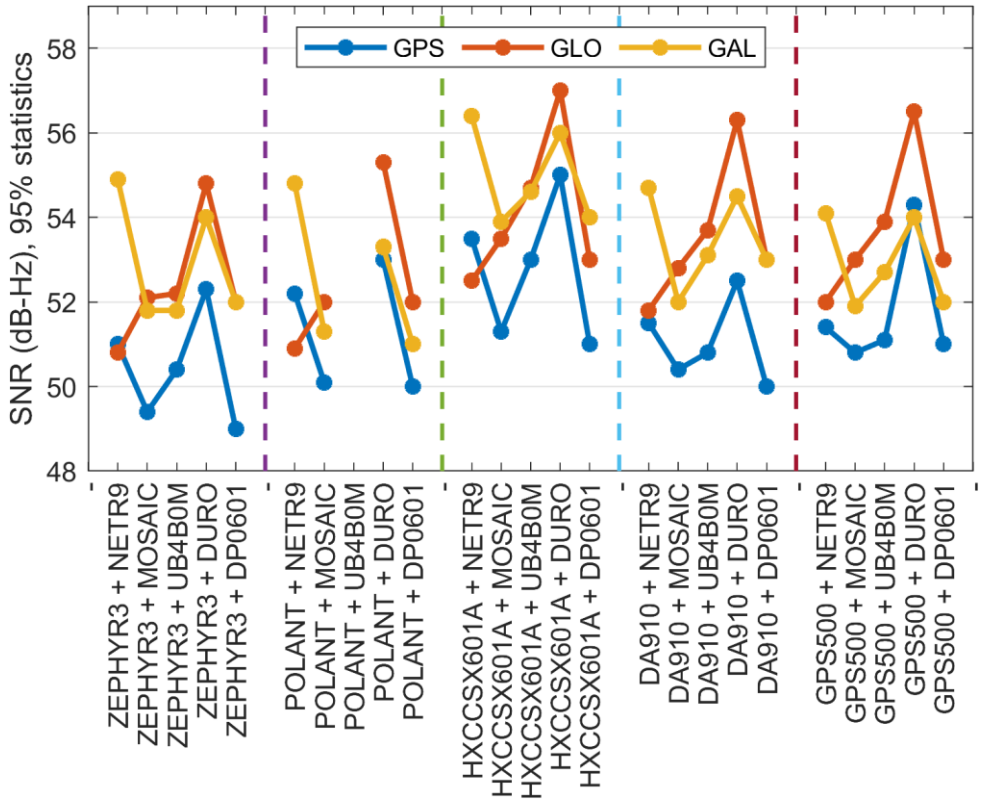

Figure 5.9 *SNR for all LM3GNSS antenna-receiver pairings*

5.2.3 Minivan Phase and Code Residuals

The compressed representation of phase and code residuals shown in the subsequent sections are ordered by the antenna type, receiver type, and constellation type. The plots are separated into five pairings, starting with the three calibrated antennas, namely, Zepyr3, PolantXMF (labeled Polant), and HXCCSX601A. The figures end with the uncalibrated antenna groups (DA910 and GPS500) in the rightmost columns.

5.2.3.1 PPK Phase Residuals

Figure 5.10 is the compressed representation of the PPK phase residuals for the five minivan sessions while roving with the GNSS hardware. Each dot in the figure represents the 95% ordered statistics for each antenna-receiver pairing. The solid lines in

blue, red, and gold indicate the change in the 95% percentile value of phase residuals between hardware pairings.

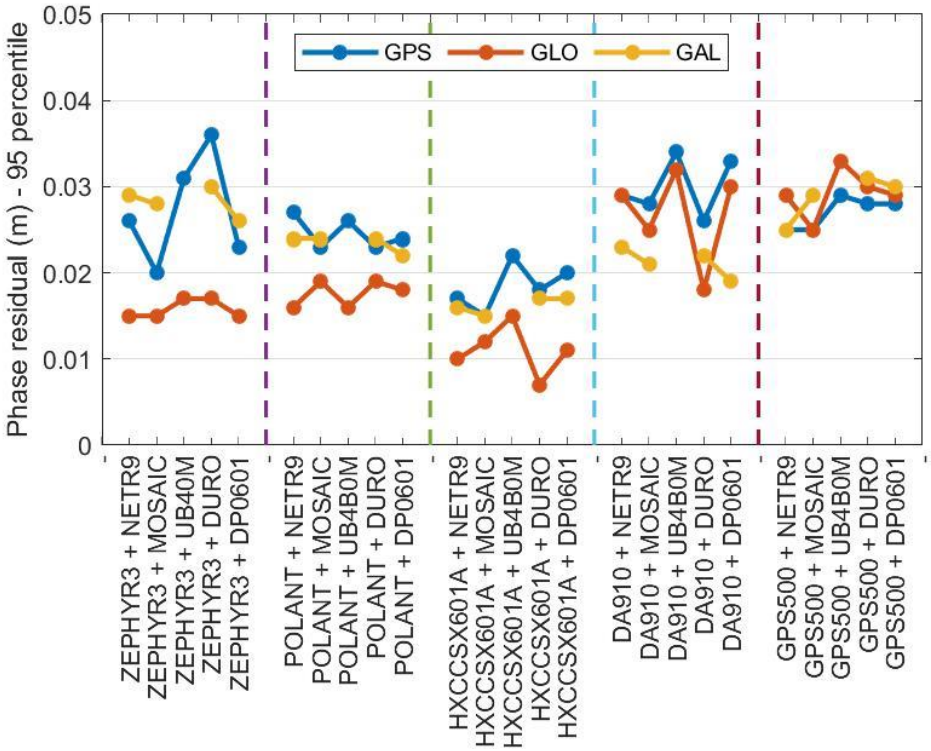

Figure 5.10 *Minivan GrafNav PPK phase residuals*

The summary shows that phase residuals did not exceed 0.04 m for any hardware pairing and constellation. The GLO constellation shows the best carrier phase measurement performances (less than 0.02 m), especially when using the calibrated antennas (the first three groups). For uncalibrated antennas, carrier phase residuals on the GLO constellation reaches about 0.035 m. According to the PPK residuals presented in Figure 5.10, the HXCCSX601A antenna shows the best antenna-receiver pairings in that the residuals are lowest on all the constellations. All the LM3GNSS receivers using low-cost calibrated antennas (Polant and HXCCSX601A) tightly compete with the carrier phase performance of Trimble NetR9 when combined with the Zephyr3 antenna. That is

contrary to expectation. For instance, the better performance of HXCCSX601A-Mosaic compared with Zephyr3-NetR9 is evident in the precision of the phase residual histogram, shown in Figure 5.11.

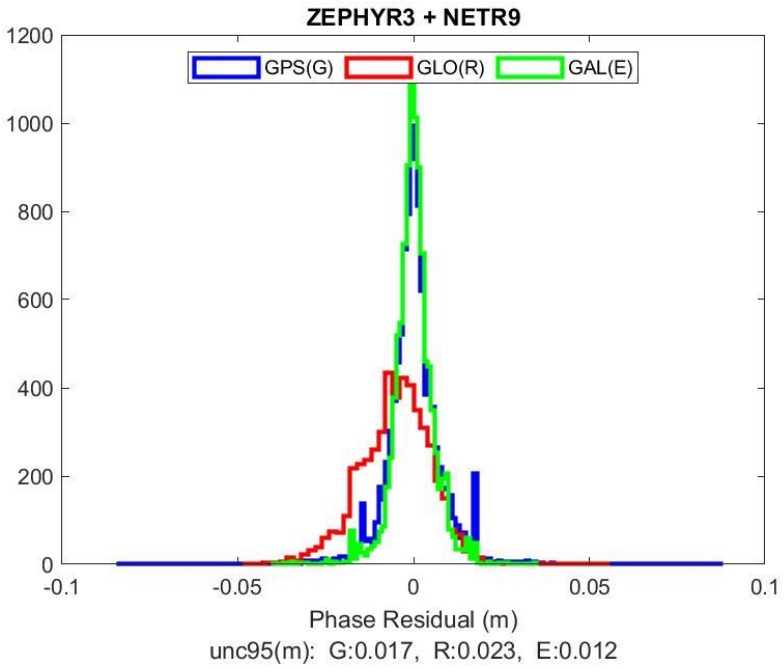

Figure 5.11a Zephyr3+NetR9

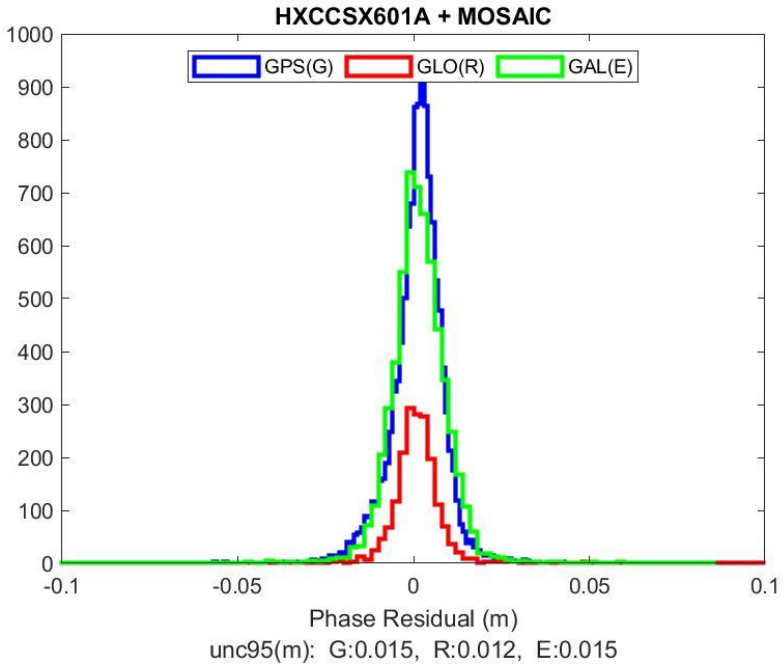

Figure 5.11b HXCCSX601A+Mosaic

Figure 5.11 *Minivan phase residuals for Zephyr3+NetR9 and HXCCSX601A+Mosaic*

An overview of phase residuals, captured by 25 histograms plots (5 receivers x 5 antennas) for all hardware pairings (not shown here), indicates that hardware pairings with the Zephyr3 antenna show between-constellation biases that are larger than most other pairings. The most significant bias is noted in the GAL constellation. Again, that trend is unexpected, and it explains why the two low-cost calibrated antennas show better phase-residual precision and accuracy. Note that UB4B0M rarely tracked GAL SVs during the minivan PPK experiment (due to an acquisition blip**)**; hence, the receiver's residual information is missing. A tracking investigation conducted after the minivan experiments suggests that UB4B0M tracks and logs measurement data for GAL SVs more reliably with a warm restart.

5.2.3.2 PPK Code Residuals

In contrast with the previous carrier phase residuals, which shows the best performance in the GLO constellation, pseudorange performance (Figure 5.12) is best in the GPS and GAL constellations with residual values rarely beyond 3 m for all hardware.

The worst residual is noted in the GLO constellation. For the GNSS hardware, which tracked the GAL SVs, their code residuals are slightly better than the GPS residuals. In the GAL and GPS constellations, the code residuals are smaller for Mosaic than NetR9. Overall, the performances of Mosaic and UB4B0M are similar to NetR9 when using a calibrated antenna. The results discussed in Section 5.3.1 and Section 5.3.2 simulates the expected performances on a more dynamic platform.

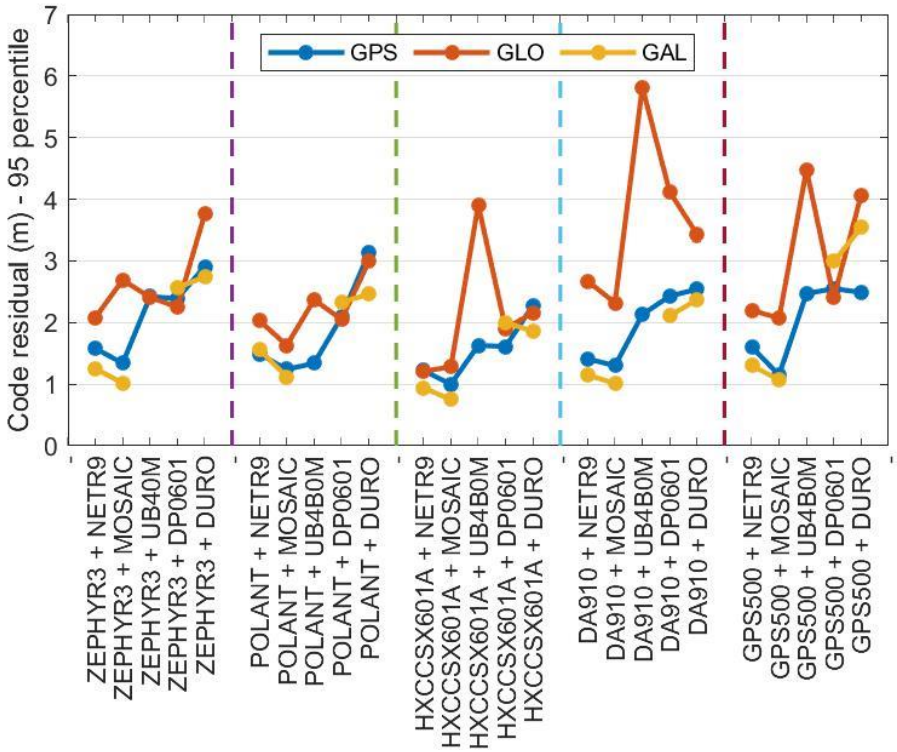

Figure 5.12 *Minivan GrafNav PPK code residuals*

5.2.3.3 PPP Phase Residuals

Figure 5.13 shows that the minivan's GrafNav PPP phase residuals did not exceed 0.05 m for all hardware. The results provide insight into the expected performance of LM3GNSS PPP at a remote location where relative positioning is rarely accessible. The Zephyr3, HXCCSX601A, and DA910 antennas show a little bias in the GLO, GPS, and BDS PPP phase residuals. The results and those presented in Section 5.2.3.4 could be used for MGNSS PPP stochastics design.

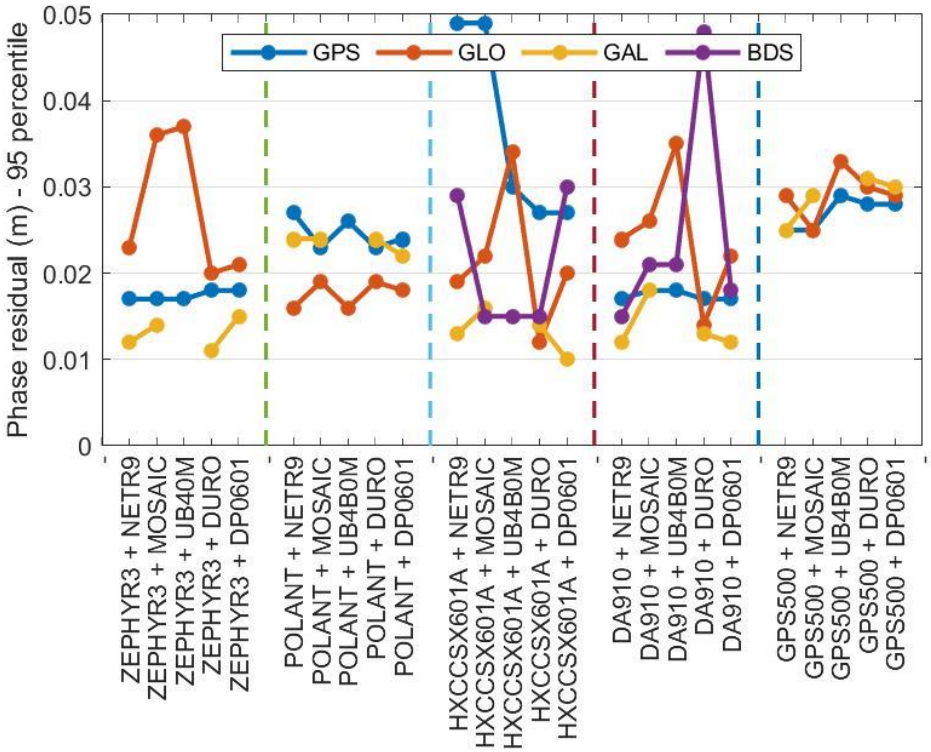

Figure 5.13 *Minivan GrafNav PPP carrier phase residuals*

5.2.3.4 GrafNav PPP Code Residuals

Figure 5.14 shows a distinct bias (about 4 m) in the GLO PPP code residual when using the Zephyr3 antenna with all GNSS hardware. The bias is mitigated in the Mosaic-Zephyr3 pairing. A similar performance is noticed in the Zephyr3 PPP phase residuals, shown in Figure 5.13, whereas the hardware pairings with other antennas show better performances than Zephyr3. That suggests the Zephyr3 antenna is not the best choice for LM3GNSS kinematic PPP, considering positioning quality and cost.

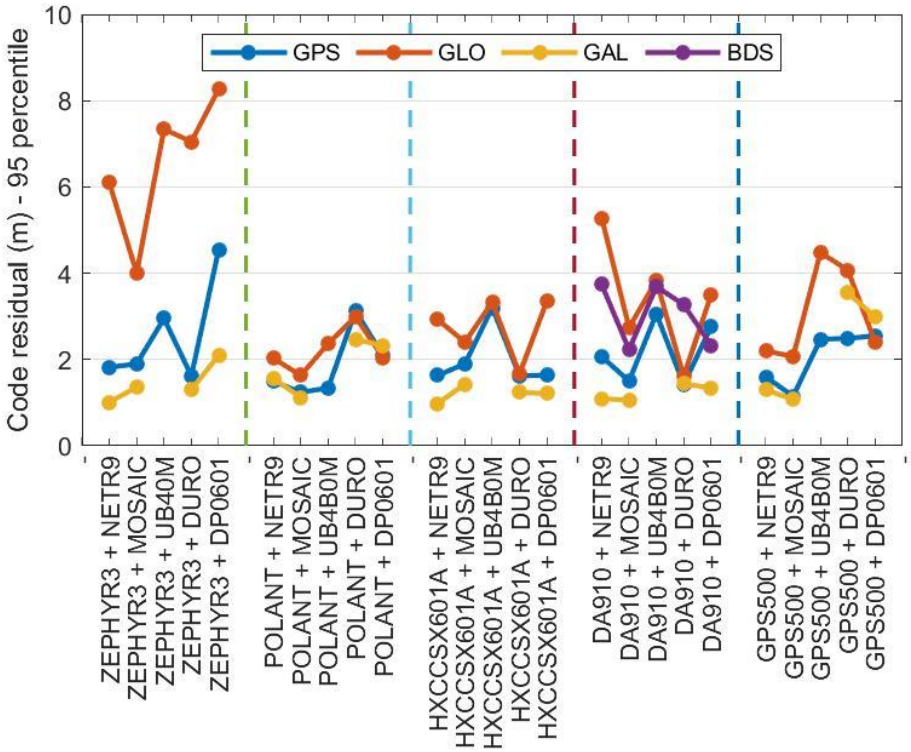

Figure 5.14 *Minivan GrafNav PPP code residuals*

A histogram version of the compressed report is shown in Figure 5.15 for minivan PPP code residuals for Zephyr3 and Polant antenna pairings. The Zepyr3 antenna shows the largest code bias in all hardware pairings for the GLO constellation. In some cases, the Zephyr3 histograms are bimodal, and the biases are up to 7 m. Similar bimodal biases (less than 7m) exist in other antennas except for the Polant antenna, which shows a near-zero bias.

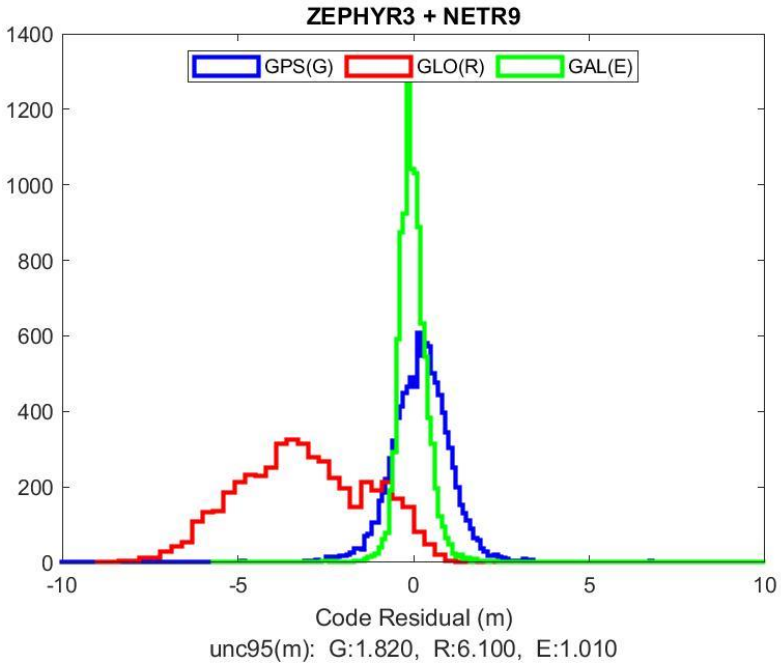

Figure 5.15a Zephyr3+NetR9

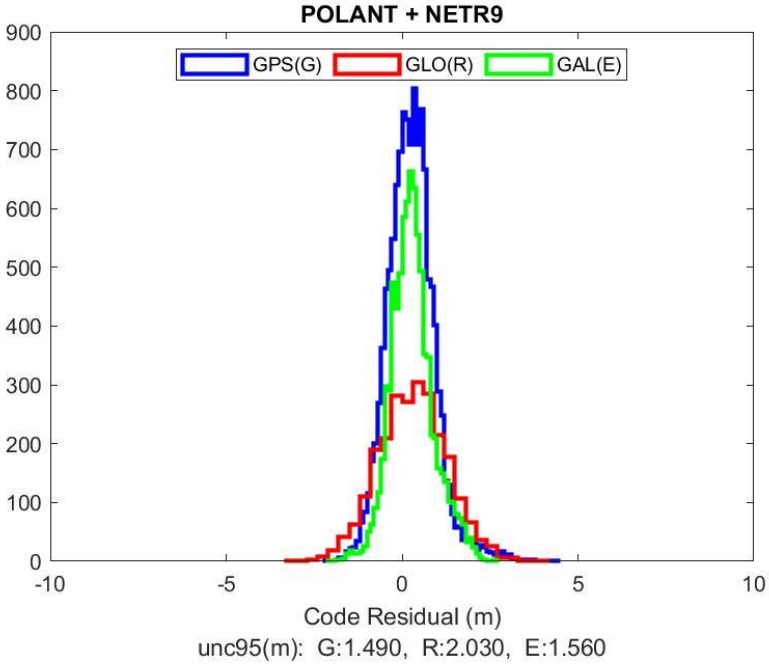

Figure 5.15b Polant+NetR9

Figure 5.15 *GrafNav Code residuals for Zephyr3+NetR9 and Polant+NetR9*

5.2.4 USMCS GipsyX Phase and Code Residuals

Figure 5.16 and Figure 5.17 show the SK-PPP phase and code residuals at USMCS. As mentioned earlier, the antennas were stationary, and they operated in kinematic mode during the SK-PPP data acquisition. The results shown in those figures indicate the positioning performances that would be expected on platforms operating offshore (i.e., GNSS buoy) while using LM3GNSS receivers for precise positioning. The carrier phase residuals indicate that the GAL constellation offers the best SK-PPP solution irrespective of the hardware. The performance of Zephyr3 in the SK-PPP strategy, in contrast with the kinematic PPP discussed in Section 5.2.3.4, supports the submission made earlier that a Zephyr3 antenna is not the best choice for kinematic PPP; however, it is a reasonable option for less dynamic applications.

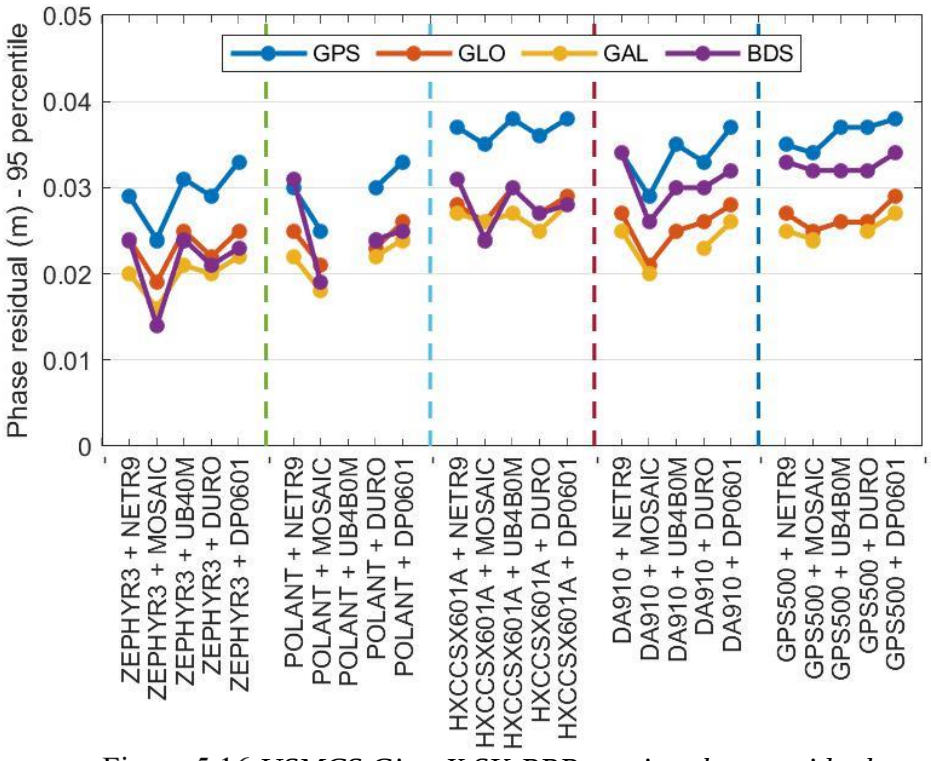

Figure 5.16 *USMCS GipsyX SK-PPP carrier phase residuals*

The Polant antenna shows the closest performance to the Zephyr3 antenna when operating in the SK-PPP strategy. Though the DA910 and GPS500 are uncalibrated, their carrier residuals are somewhat like the calibrated antenna. The reason could be attributed to the cloned ANTEX files used for the uncalibrated antennas, which implies that the proper calibration of their PCOs and PCVs will yield better positioning better performances, as noted in a study by Hauschild et al. (2020).

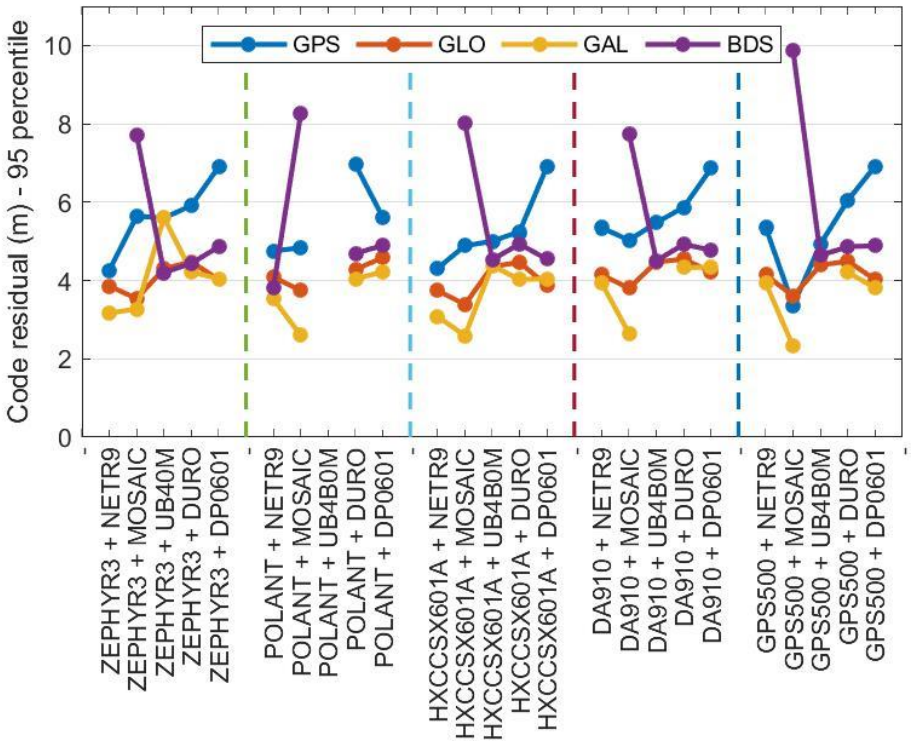

Figure 5.17 *USMCS GipsyX SK-PPP code residuals*

5.3 LM3GNSS Positioning Performance

This section compares LM3GNSS relative to NetR9 PPK (minivan) solutions. At USMCS, SK-PPP solutions using LM3GNSS receivers are compared relative to both NetR9 and the calibration coordinates. The minivan's PPK vertical results, relative to NetR9, indicate that the 95th percentile of the ordered statistics for solutions with

calibrated and uncalibrated antennas range between 0.03 and 0.15 m. That implies certain pairings of LM3GNSS hardware will provide performance similar to a high-end GNSS receiver while meeting special-order survey specifications, provided that the cumulative uncertainty, in addition to those arising from depth-dependent parameters, such as sounding and ellipsoid-chart-datum separation, does not exceed the specified tolerance (i.e.0.29 m in shallow water). In order to evaluate the performance of LM3GNSS PPP aboard the minivan, that assessment was relative to NetR9 PPK. The vertical results vary from 0.05 to 1.2 m at a 95^{th} percentile. Subsequent sections note some factors that impact PPP solutions when using LM3GNSS receivers.

5.3.1 Minivan GrafNav PPK Performance Relative to NetR9

In determining the PPK uncertainty of the LM3GNSS receivers, the adopted strategy compares the minivan's PPK results for each antenna-receiver pairing relative to NetR9's results (Figure 5.18). The histograms in each row represent different experiments with a particular antenna pairing with the receivers. Each column represents the differences in the PPK results of a particular receiver relative to NetR9's results.

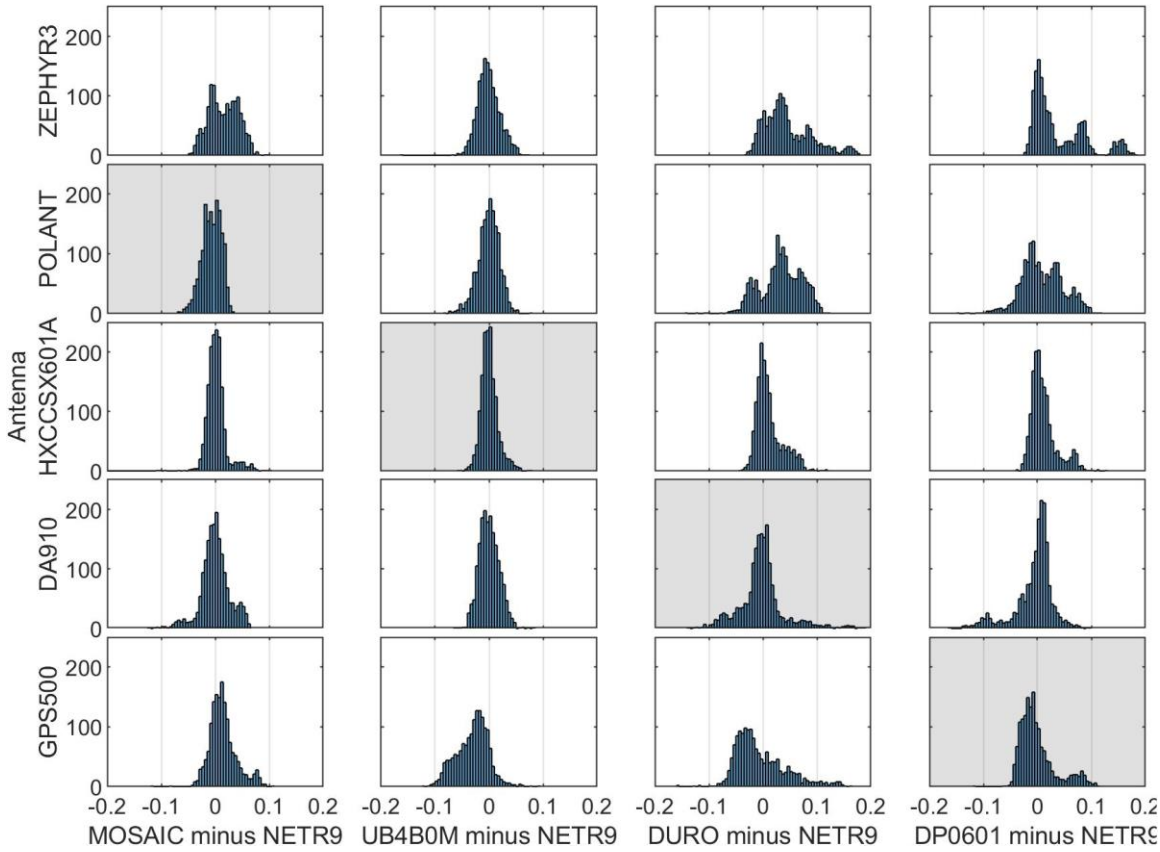

Figure 5.18 *Histograms of GrafNav PPK results for each antenna-receiver pairing.* Recall that the top three rows (Zephyr3, Polant, and HXCCSX601A antennas) are calibrated or partially calibrated in the ANTEX database, while the two bottom rows are antennas for which a generic elevation-only cloned ANTEX file was used.

Choosing NetR9 as the reference is predicated upon one of the questions this dissertation seeks to answer: should high-end GNSS hardware on survey platforms be replaced with LM3GNSS hardware? Figure 5.18 and Figure 5.19 partly answers that question as follows:

1. Almost every antenna/receiver pairing resulted in a histogram that was within 10 cm of the NetR9 reference geodetic results, the exceptions being the Zephyr3 antenna with the two rightmost receivers.

2. The “Mosaic minus NetR9” and “UB4B0M minus NetR9” receiver columns show histograms that are generally narrower and unskewed, in comparison with the “DURO minus NetR9” and “DP0601 minus NetR9” columns.
3. The HXCCSX601A antenna provided the narrowest histograms, with some skewing for the two rightmost columns. The Polant antenna histograms were slightly worse for the two leftmost receivers and much worse for the two rightmost receivers. The Zephyr3 antenna is slightly worse for the UB4B0M receiver and much worse for the other three receivers.
4. Except for the “Mosaic minus NetR9” results, the GPS500 antenna, even with its cloned ANTEX file, performed worse than the other antennas.

As mentioned in Section 3.2.2, the minivan traveled at an average speed of 80 km per hour (43.4 knots), which is much faster than the typical hydrographic survey speed, ranging between 5 and 10 knots (National Ocean Service, 2018). Therefore, the minivan’s PPK results should represent the solution scenarios aboard a survey vessel.

Figure 5.19 is a compressed representation of the histograms where each dot shows the 95^{th} percentile of ordered statistics (vertical and horizontal components) for different antenna-receiver pairings. Each column in the figure represents different pairings (observation sessions on different days) with different antenna, and the broken lines in different colors delineate the sessions. It should be noted that the first three columns present the calibrated antennas while the other two are the uncalibrated antennas.

The Mosaic’s and UB4B0M’s vertical uncertainties approach NetR9’s results when using the HXCCSX601A antenna. The comparison of the calibrated antennas

shows that the HXCCSX601A antenna has the best vertical positioning performance as the relative vertical uncertainties (relative to NetR9) for all receivers do not exceed 0.05 m. The PPK carrier-phase residuals, presented in Figure 5.10 of Section 5.2.3.1, confirms the trend.

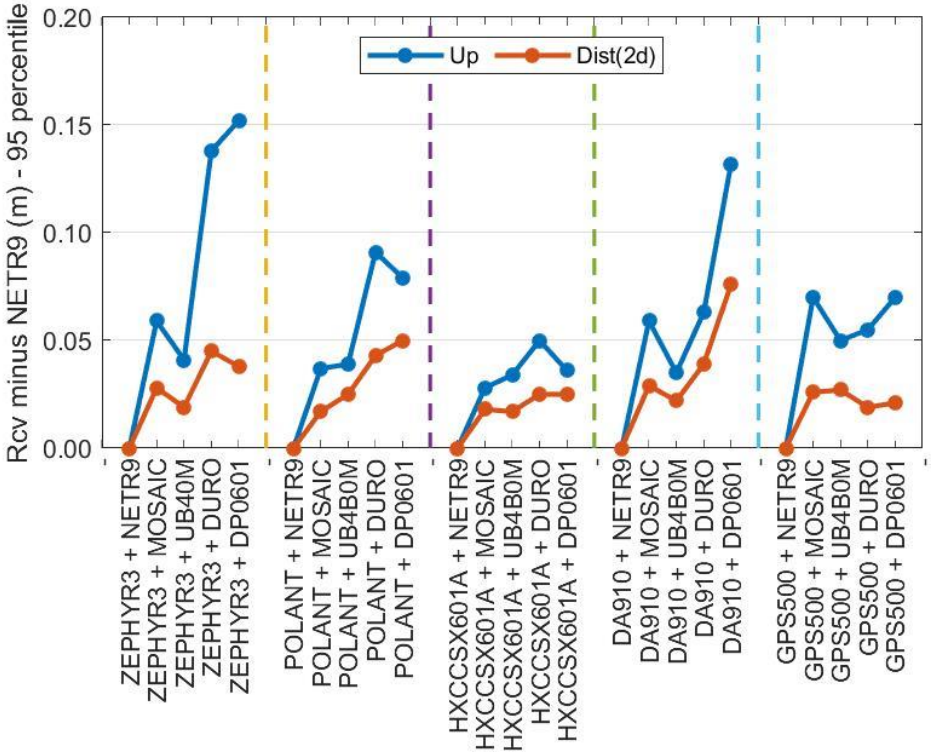

Figure 5.19 *Minivan GrafNav PPK performance relative to NetR9*

The Polant antenna shows the second-best performance while Zephyr3, contrary to expectation, shows the worst performance among the calibrated antennas. The reason is related to the observed inter-system bias of the carrier phase residuals, which is about 0.02 m larger than the other antenna pairings' biases. The positioning performances of the uncalibrated antennas (DA910 and GPS500) are reasonably close to those of NetR9. Those results are also validated by the phase and code residuals presented earlier in Sub-Sections 5.2.3.1 and Section 5.2.3.2, respectively.

Figure 5.20a shows the results relative to NETR9 of the Zephyr3 antenna pairing, and Figure 5.20b showsDA910 antenna pairing. The figure shows that ublox (DP0601 / Drotek) and the Duro receivers did not perform as good as others while using the Zephyr3 antenna. In contrast, it is also evident that Duro's performance significantly improves when using the DA910 antenna (uncalibrated). The DP0601receiver shows the same trend described for Duro. That reaffirms the earlier statement in Section 5.2.3.4 that a high-grade geodetic antenna (i.e., Zephyr3) designed for static observations may not be the best fit with LM3GNSS kinematic operations.

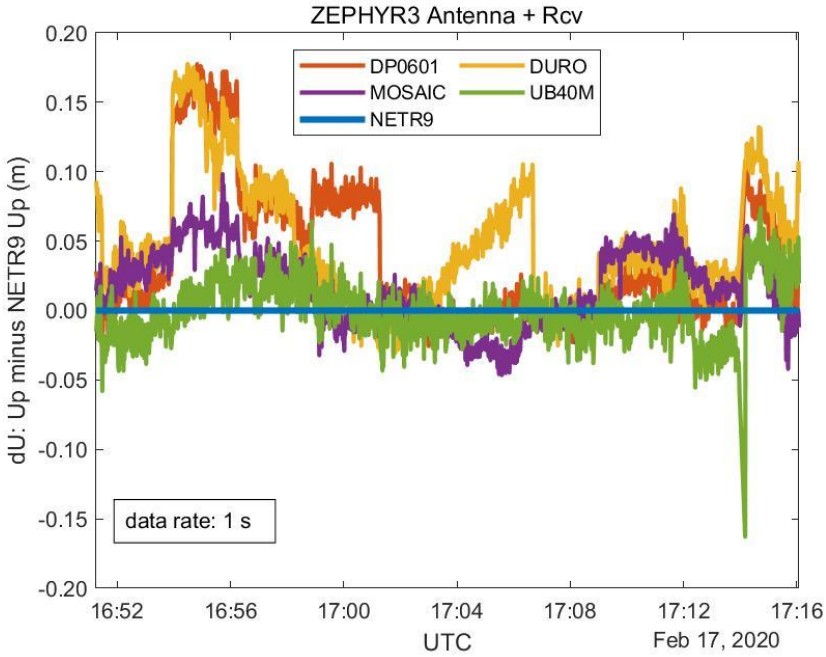

Figure 5.20a LM3GNSS with Zephyr3

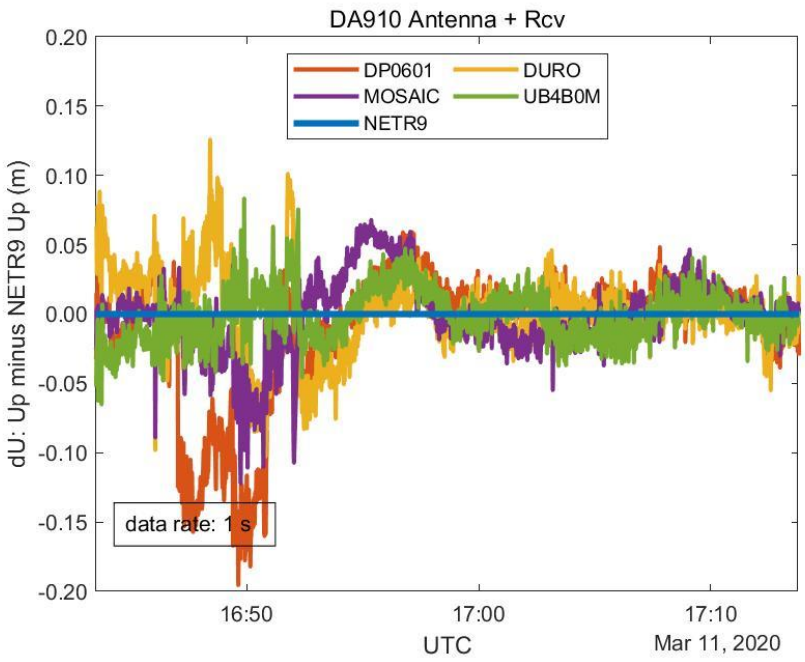

Figure 5.20b LM3GNSS with DA910

Figure 5.20 *LM3GNSS with Zephyr3 and DA910 up relative to NetR9*

5.3.2 Minivan GrafNav PPP Performance Relative to NetR9 (GrafNav PPK)

In the performance evaluation of the kinematic PPP solutions (Figure 5.21) for the minivan trajectory, the instantaneous positions of the LM3GNSS receivers are compared relative to the NetR9's PPK solutions. That provides a reliable assessment of LM3GNSS PPP solutions in that the uncertainty of NetR9 PPK solutions do not exceed 0.08 m (two sigmas) in the up component. Note that the processed trajectory is about 30-minutes long, but the results excluded the segment between the I-10 underpass and the Stennis gate (due to loss of lock). In Figure 5.21, the Mosaic vertical performance is often better than 0.20 m (2 sigmas). UB4B0M shows the worst performance, attributed to the acquisition blips leading to non-tracking of GAL SVs and reducing the total number of SVs included in PPP solutions. The exact reason for the acquisition blip was not fully established,

though a warm start after powering the receiver appeared to have enabled the continuous tracking of five GAL SVs.

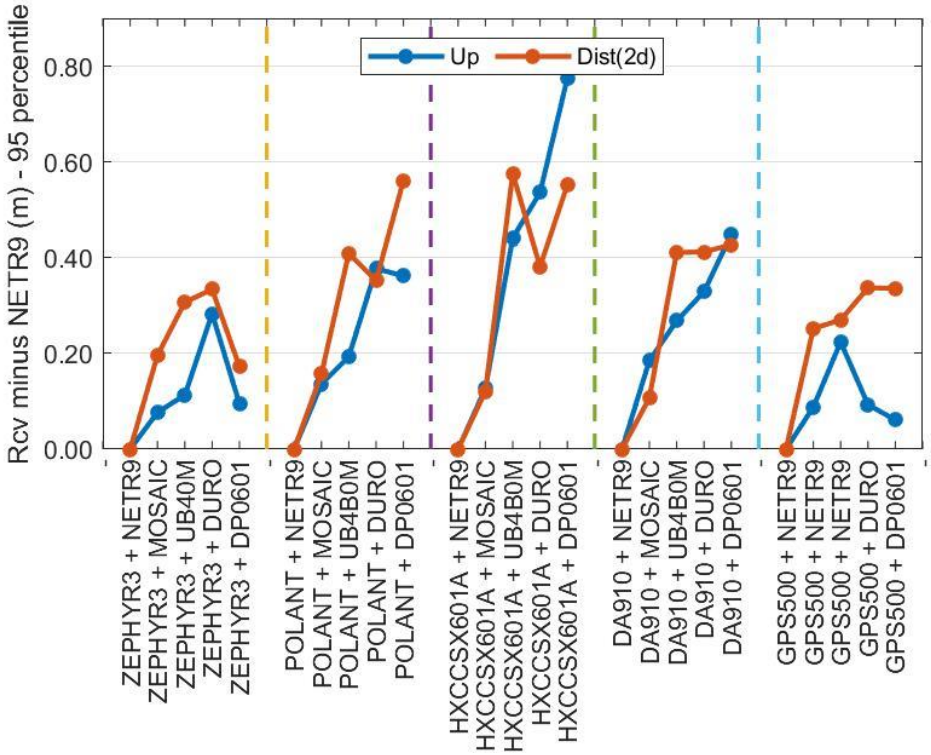

Figure 5.21 *Minivan GrafNav PPP performance relative to NetR9 (GrafNav PPK)*

The PPP performance with the GPS500 antenna exceeds expectations. That is attributable to the total number of satellites included in the PPP solutions for all the receivers. All receivers have about twenty-five satellites included in their PPP solutions except for Duro and UB4B0M, which have about twenty satellites. When using DA910 and GPS500 antennas, about three BDS SVs (PRN C11, C12, and C14) are included in the PPP solutions. In some instances, the number of BDS SVs in the PPP solutions drops to either one or zero. While roving with the HXCCSX601A antenna, only one BDS SV (PRN C14) was included in the PPP solutions for all receivers. For the rest of the calibrated antennas, the PPP solutions did not include any BDS SV.

It is worth mentioning that eight of the trackable BDS SVs (namely PRN C19, C20, C23, C27, C28, C32, C36, and C37) along the minivan route are excluded in CODE and GFZ SP3 files. Besides, BDS satellite availability differs for a given set of PRNs, over a given time at a given location because of orbital altitude. That is related to the ground track repeat cycle of BDS MEO SVs, seven sidereal days (thirteen revolutions), unlike the GPS constellation, which has a daily repeat cycle - two revolutions per sidereal day (Teunissen & Montenbruck, 2017, p. 221 and 281). For those reasons, the PPP solutions for the Zephyr3- and Polant-antenna sessions did not include any BDS SV since those trackable SVs are unavailable in the SP3 file. Again, that explains why the GPS500-antenna session shows a better performance than the sessions with Zephyr3- and the Polant-antenna. On average, LM3GNSS PPP performance is about 0.3 m (2 sigmas) in the up component for any hardware pairing without the BDS SVs. It is expected that PPP performance would improve once the trackable BDS SVs are included in the MGEX products.

5.3.3 USMCS GipsyX SK-PPP Performance Relative to NetR9

The SK-PPP performances of LM3GNSS relative to NetR9 (at USMCS) should simulate the expected PPP performance on a GNSS buoy or a monitoring platform, requiring accurate kinematic positioning while operating at a remote location. Again, the SK-PPP results should justify the use of LM3GNSS receivers as an alternative to using high-end receivers at a remote location in PPP mode. Figure 5.22 shows the SK-PPP positioning performances for all hardware pairings. The Zephyr3 antenna pairings suggest better performance when operating on less dynamic platforms than a fast-moving

body. Within the scenario described and using a calibrated antenna, all receivers are capable of kinematic PPP performances similar to NetR9.

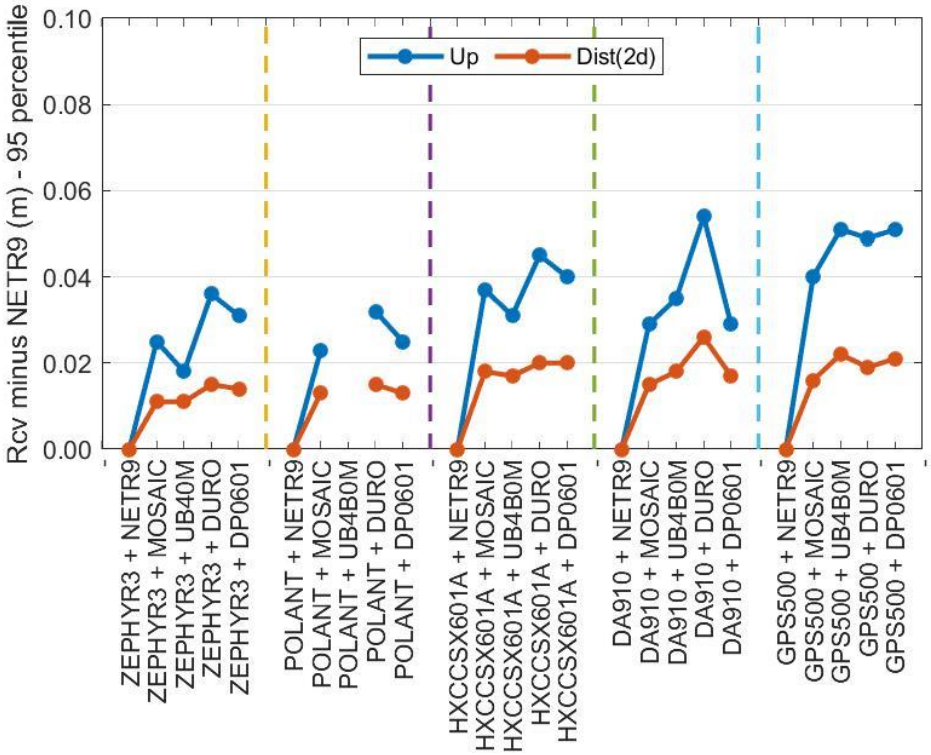

Figure 5.22 *USMCS GipsyX SK-PPP performance relative to NetR9*

5.3.4 USMCS GipsyX SK-PPP Performance Relative to Calibration Station

The SK-PPP results in Figure 5.23 are relative to USMCS coordinates, while those in Figure 5.22 are relative to NetR9. The SK-PPP performance adds weights to the performance metrics in favoring LM3GNSS as an alternative to high-end receivers for GNSS buoy and similar applications on static or near-static platforms. The Polant antenna performance is twice better than the Zephyr3 antenna (Figure 5.23), while the HXCCSX601A and GPS500 (uncalibrated) antenna show performances similar to Zephyr3. The quality of the ANTEX file used for the PPP computation in GipsyX is partly why the 0.1-m bias was noted in the up component of DA910.

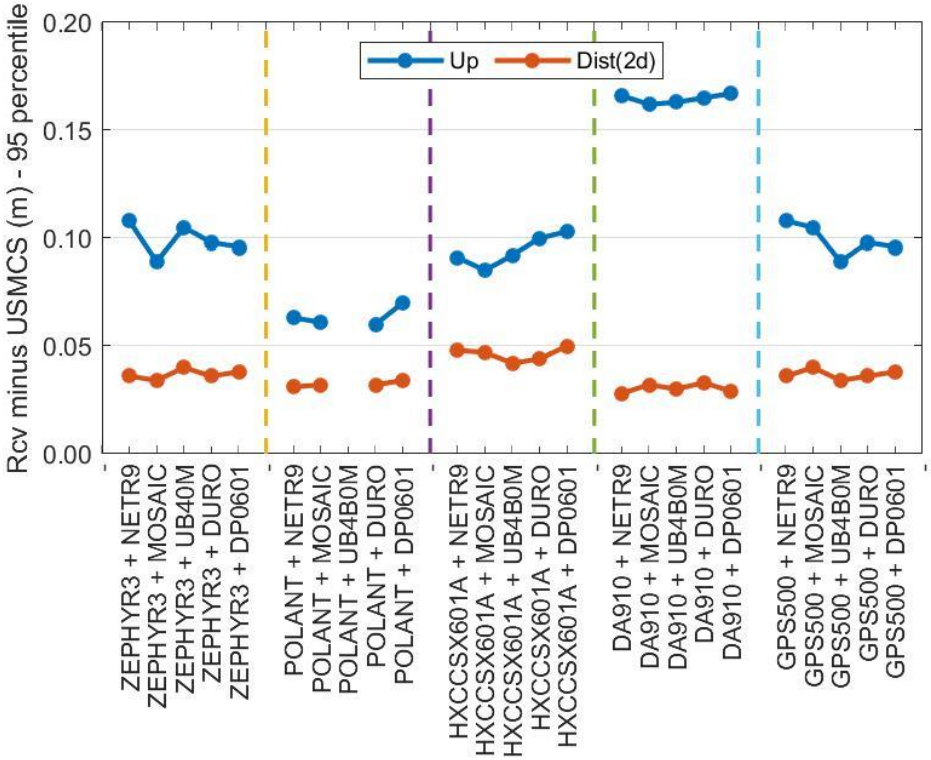

Figure 5.23 *USMCS GipsyX SK-PPP performance relative to calibration coordinates*

The time series of the PPP solutions relative to USMCS coordinates (Figure 5.24a) affirms the bias in the up component of the DA910 session (Figure 5.24b). Depending on the application requirements, an uncalibrated antenna may as well deliver the required results.

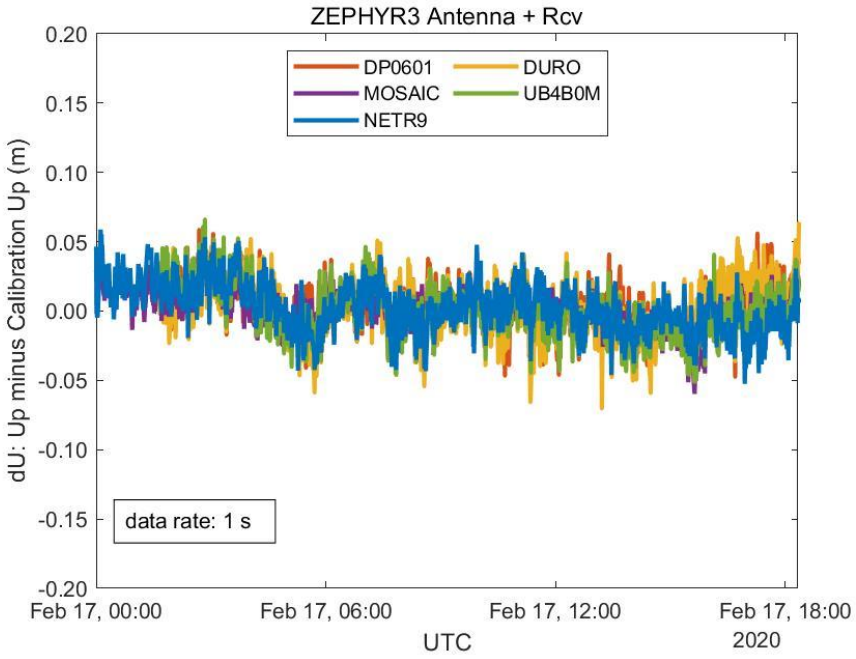

Figure 5.24a GipsyX PPP with Zephyr3

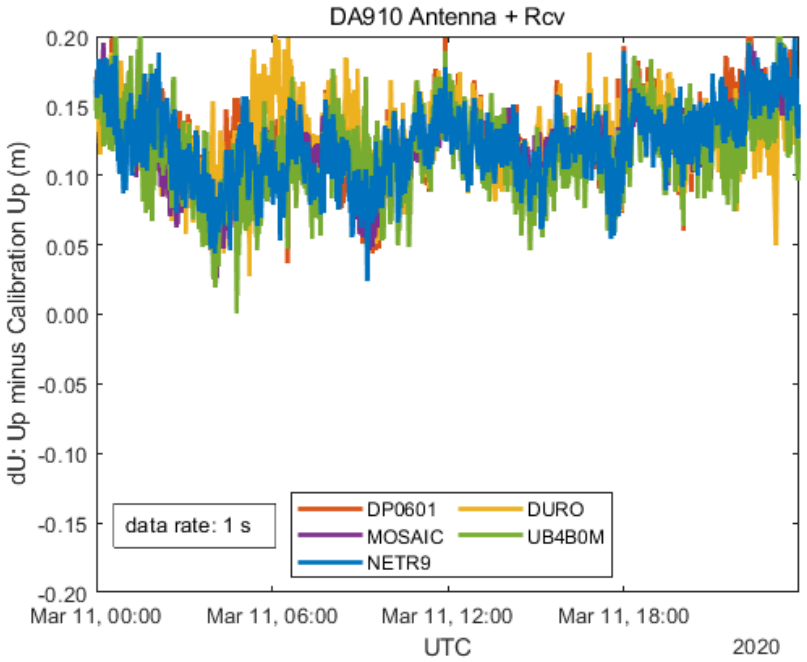

Figure 5.24b PPP with DA910

Figure 5.24 *USMCS GipsyX PPP with Zephyr3 and DA910*

5.3.5 Summary of Positioning Performance

In summary, the effect of antenna type on positioning accuracies of the different receivers is evident and depends on whether the antenna is calibrated. The results show that a high-grade antenna designed for geodetic network applications may not be the best pairing with LM3GNSS receivers for performance improvement. It is also clear that low-cost antennas, reasonably calibrated, will achieve performances similar to or better than the high-grade antennas in dynamic positioning applications. The LM3GNSS receivers consistently show performances comparable to NetR9 and even better in some cases.

5.4 PPK with LM3GNSS and NGS CORS

This section highlights some possible challenges a user might encounter while attempting to post-process the LM3GNSS dataset with an NGS CORS as the reference. The issues highlighted in this section are not limited to LM3GNSS processing but includes any scheme of kinematic solutions. Table 5.1 shows that the processing scheme was designed such that matching antenna-receiver pairs are post-processed. That is likely not the case in real-life when precise positioning is required, as most users would avoid deploying a local reference receiver and would prefer to use a standard CORS. Most times, the CORS receiver and antenna, the tracked constellation, and the sampling rate would be different from the user case scenarios. Hence, choosing to use a standard CORS as the reference comes with a cost, especially when high accuracy is desired with multi-frequency and MGNSS receivers like those discussed so far in this dissertation.

5.4.1 PPK Challenges with Existing NGS CORS

In order to demonstrate that this challenge exists and that it may portend some severe positioning degradation, the same set of minivan data was post-processed, but this time using MSIN, the nearest NGS CORS to the minivan route, as the reference station (the solutions later referred to as MSIN PPK). Three issues were identified, and they include the limited multi-constellation dataset (only GPS and GLO) currently available at most NGS CORS, limiting the advantages offered by multi-constellation processing. The second issue is the misleading information that MSIN's data sampling rate is 1 second, as indicated by the NGS CORS map (see Figure 5.25). Unfortunately, that was not the case. The data set collected for dates indicated in Table 5.1, directly from NGS FTP (NOAA, 2020), shows that MSIN observation files are archived at a 30-s sampling rate.

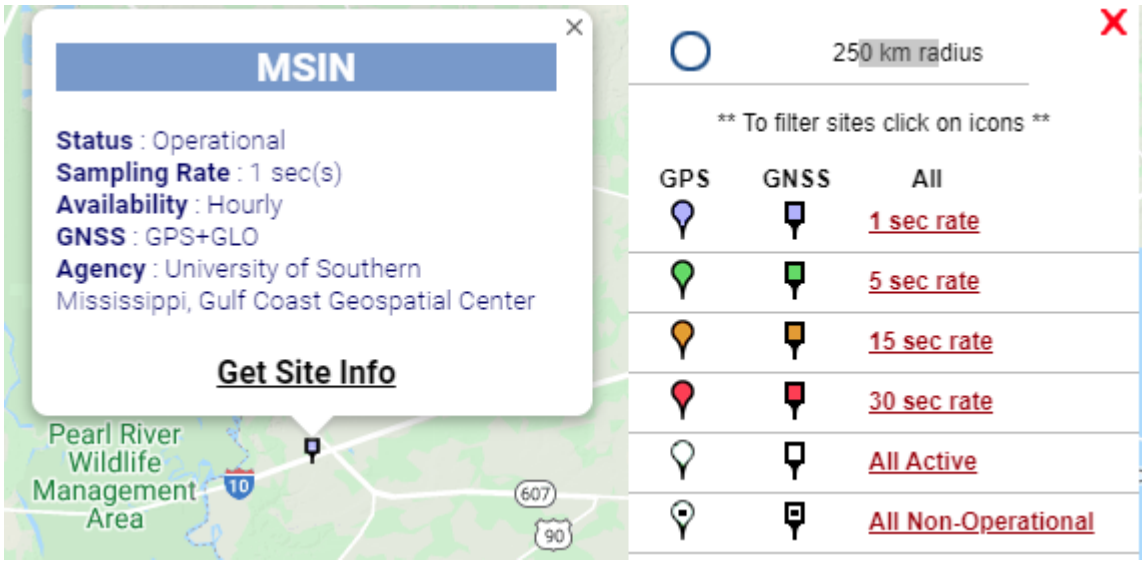

Figure 5.25 *NGS CORS map showing 1-sec sampling rate for MSIN*

The third issue identified is the interpolation of MSIN observation files from a 30-s to 1-s rate, which may be invalid as indicated in the GrafNav and GFZRNX tool. Attempts to re-sample MSIN with the GFZRNX tool at 1 s failed as the RINEX tool

defaults the output back to 30 s. GrafNav's attempts seem successful in seven out of twenty-five processing batches. The resampled observation files from GrafNav are in binary format; hence a direct verification of the re-sampled data remained unverifiable. Further investigations into the PPK solution output file (ASCII) from GrafNav shows that MSIN PPK solution did not include GLO SVs at 1-s time-step but only at the 30-s step for eighteen of the twenty-five processed batches. That resulted in a continuous fluctuating number of SVs used in the PPK solutions. Figure 5.26a and Figure 5.26b depict that scenario and compare the number of SVs included in MSIN PPK with those included in USMCS PPK.

Figure 5.27a represents the combined effect of the RINEX data interpolation and the limited MGNSS data availability in PPK processing. The up component variations are up to 0.25 m (95th percentile) for all hardware pairings, although the ambiguity resolution status is between 99 and 100%. In contrast, the 95% uncertainties relative to NetR9 do not exceed 0.1 m for USMCS PPK shown in Figure 5.27b.

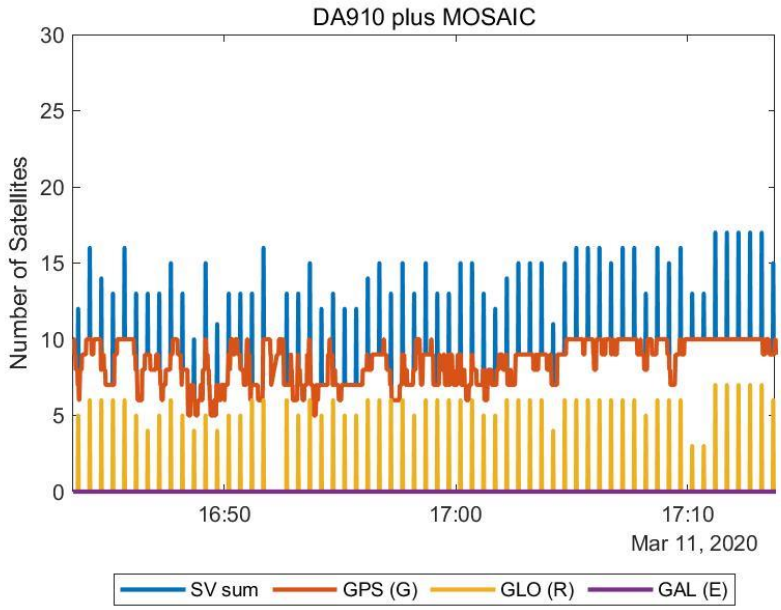

Figure 5.26a Number of SVs in MSIN PPK

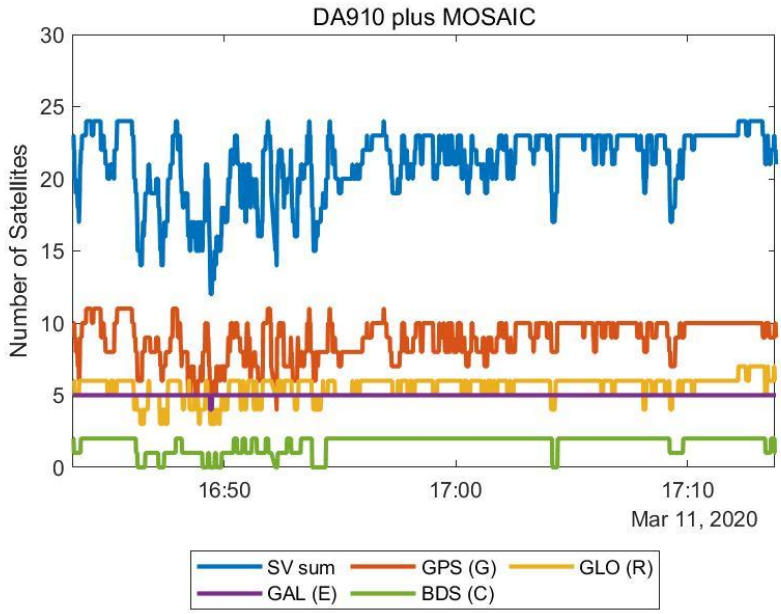

Figure 5.26b Number of SVs in USMCS PPK

Figure 5.26 *Number of SVs in MSIN PPK and USMCS PPK*

In Figure 5.26a, the fluctuating number of SVs used in a PPK solution test with MSIN CORS. The fluctuation is due to the re-sampled reference station (MSIN) data.

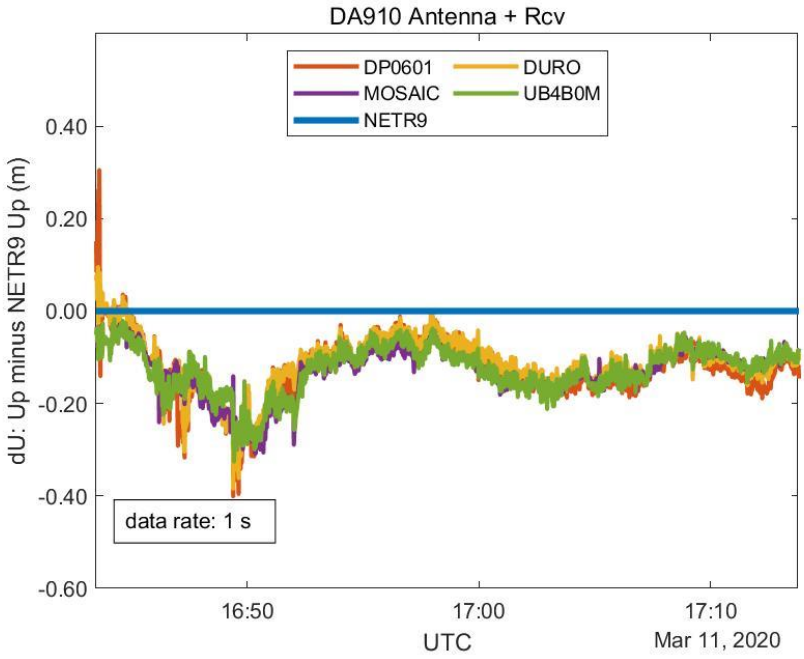

Figure 5.27a Drift effect

.

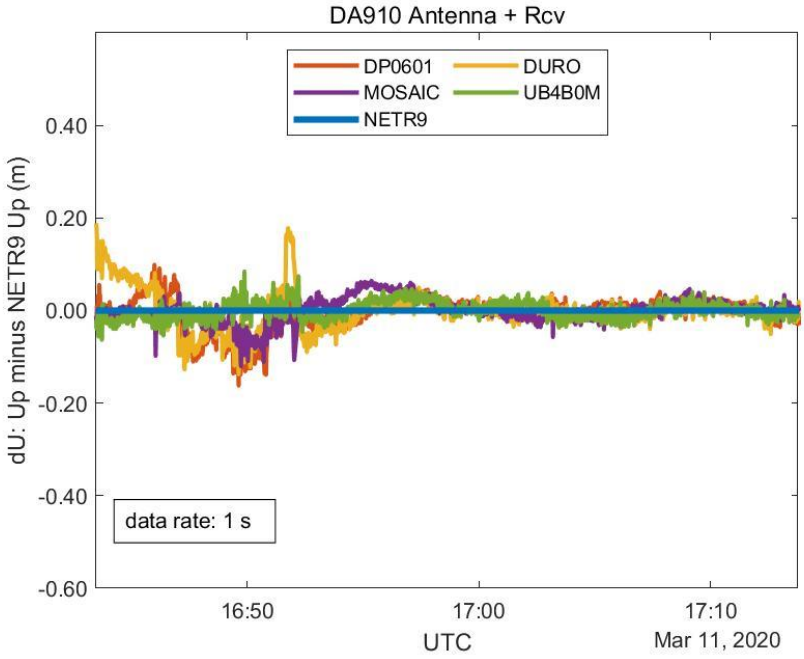

Figure 5.27b Improvement with MGNSS

Figure 5.27 *Drift effect and improvement with MGNSS*

Figure 5.27a is the resultant effect of the fluctuating number of SVs on positioning solutions. Figure 5.27b is the MGNSS solution for the same dataset as *Figure 5.27a*. Note that the NetR9 reference solutions (shown in blue on both figures) are from USMCS MGNSS PPK.

Another example of positioning degradation when using NGS CORS is shown in Figure 5.28a, where 100% of Duro and 50% of DP0601 PPK are float solutions. Overall, significant improvements with MGNSS are noted in Figure 5.27b and Figure 5.28b. That further emphasizes how LM3GNSS positioning benefits from multi-constellation capabilities. The results presented in this section suggest that a user has to exercise caution when deciding on a CORS as reference for both geodetic-grade and LM3GNSS PPK solutions since many CORSs are yet to be multi-constellation-enabled, and their data sampling interval may be much higher than 1 s.

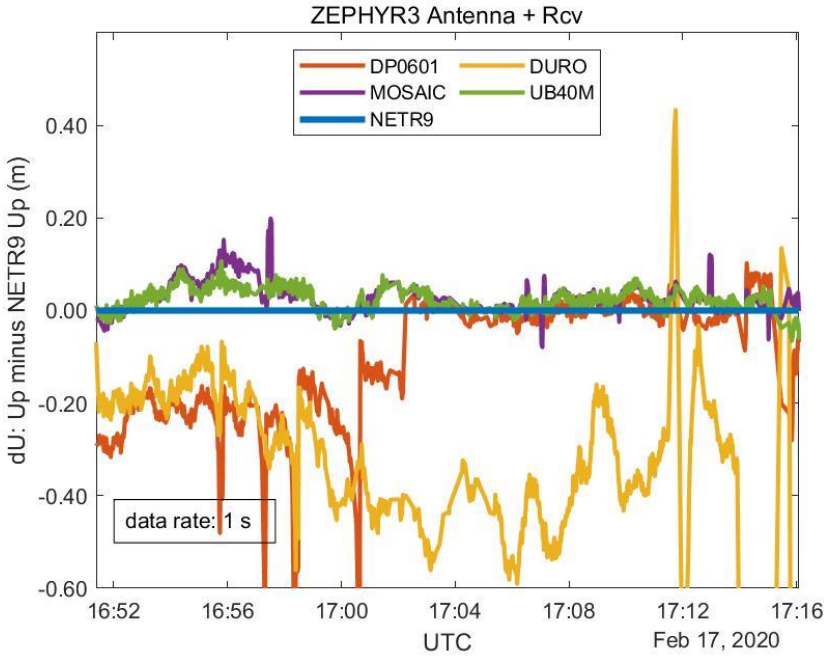

Figure 5.28a GrafNav PPK float effect

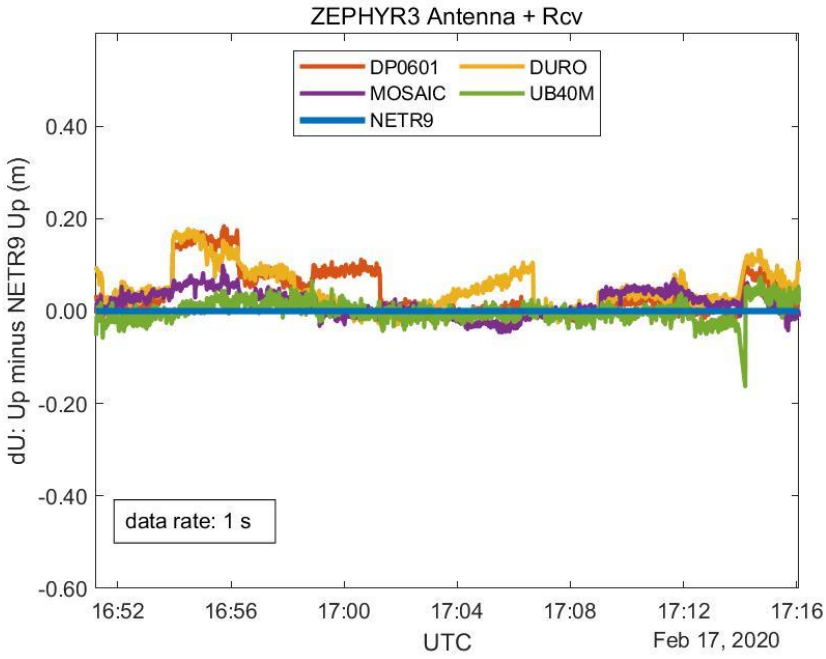

Figure 5.28b improvement with MGNSS

Figure 5.28 *GrafNav PPK float effect and improvement with MGNSS*

Figure 5.28a shows 100% float solutions for Duro, 50% float solutions for DP601, 99% fixed solutions for UB4B0M, and MOSAIC. Figure 5.28b shows the improvement with MGNSS when using USMCS as the reference.

CHAPTER VI CONCLUSIONS AND RECOMMENDATIONS

This chapter summarizes this dissertation, the results and concludes with answers to the dissertation questions. Briefly summarized here is the newly developed GNSS tool, which provided thorough data analysis.

6.1.1 Conclusions

For data processing efficiency and analysis, a new GNSS analysis software called GPM is introduced for multipath and SNR characterization as metrics for data quality. The software was used throughout the data analysis in this dissertation. GPM features include but are not limited to the ingestions of RINEX3, SP3, GrafNav binary residual, GipsyX ASCII, GrafNav ASCII files. The processing features include orbit interpolation, multipath, SNR characterizations, coordinate transformations, and GPS calendar computations (GPS week number and DOY). The automated scripting feature includes script generation for unattended operation of GipsyX software in Linux with minimal interaction, unsupervised data analysis, and systematic file management.

Recall that this dissertation emphasizes the vertical positioning performances of LM3GNSS receivers in the context of ERS strategy and the minimum requirement for hydrographic surveys, especially in shallow waters. The dissertation discussed four LM3GNSS receivers and antennas from different manufacturers in PPK and PPP strategies and determined that they can perform comparably to high-end GNSS receivers. Since LM3GNSS receivers are power efficient and cost-effective, their positioning shows they are good alternatives for high accuracy positioning. Recall that their results approach those of higher-end GNSS receivers.

Conclusion 1: LM3GNSS hardware provide effective alternative positioning and navigation performance for emerging survey platforms such as ASV and sUAS.

Using the IHO specification as the minimum standard for vertical uncertainty, the TVU uncertainty in very shallow waters (0 – 20 m) should not exceed 0.29 m at a 95% confidence interval. That value encompasses all the uncertainties associated with depth-dependent parameters that must be budgeted and accounted for in all stages of the bathymetric survey. For the GNSS height component, when using the ERS technique, this dissertation assumes 0.15 m as a conservative 95% uncertainty criterion for deciding on LM3GNSS receiver's performances in meeting high-accuracy positioning requirements on marine platforms.

The experiment designs addressed the performances of LM3GNSS receivers on mobile and relatively non-mobile platforms via reasonable simulations. All the receivers tracked data in the ZBL configuration in all sessions. The PPK and kinematic PPP solutions with a roving minivan simulated the performances of LM3GNSS on mobile marine platforms while the SK-PPP solutions at USMCS simulated the LM3GNSS performances on GNSS buoy. At USMCS, this dissertation compared LM3GNSS hardware performances relative to the calibration coordinates and NetR9 solutions. The minivan PPK performances are assessed relative to NetR9 solutions, while the minivan PPP is assessed relative to NetR9 PPK solutions. In addition to the positioning performances of LM3GNSS receivers, their measurement quality has been characterized in this dissertation using multipath, SNR, code, and carrier residuals.

This dissertation notes that the positioning method's processing strategy is vital in the performance achievable with any LM3GNSS receiver-antenna pairing. The author

used GipsyX software for the SK-PPP solutions at USMCS to simulate the performances a user might expect when using LM3GNSS receivers on offshore buoys. GipsyX PPP strategy permits the ionospheric-free combinations for all LM3GNSS datatypes, unlike the online CSRS-PPP processing engine currently limited to specific modulations, as discussed in this dissertation. Besides, GipsyX software permits the modification to data processing configurations via files that are openly accessible by the users. High-accuracy PPP solutions that are better than 0.12 m at a 95% confidence level are achievable with any LM3GNSS hardware pairings, especially when the antenna is in operation on less dynamic platforms. That order of accuracy and successful processing is only possible provided the GNSS receiver, ocean-loading, and ANTEX files are modified to include LM3GNSS receiver and antenna names, as well as station information in the GipsyX database.

To minimize errors due to phase center offset and variation patterns for the DA910 and GPS500 antennas (uncalibrated), an NGS ANTEX file was cloned. SK-PPP solutions relative to the calibration coordinates shows that most hardware performances (about 0.1 m at 95% confidence level) in the up component when using the GPS500 antenna are comparable to calibrated antennas (Zephyr3, Polant, and HXCCSX601A). The best vertical positioning performance in the GipsyX PPP strategy is noted in the Polant antenna pairings as the uncertainties are better than 0.08 m at a 95% confidence level. The SK-PPP solutions at USMCS relative to NetR9 also show that the performances of LM3GNSS receivers with uncalibrated antennas are better than 0.06 m while it is better than 0.05m 95% confidence with a calibrated antenna. Those relative comparisons to the calibration coordinates and NetR9 show that:

Conclusion 2: Any LM3GNSS hardware can provide accuracy on the order of 0.15m at a 95% confidence level in PPP strategy on relatively non-mobile platforms.

However, their performances in dynamic environments may differ slightly, depending on the platform dynamics, as demonstrated in this dissertation. Receiver correlators have different sensitivity to platform dynamics depending on their design. For receivers with high dynamics sensitivity, the tracking error will be significant in a harsh dynamic environment, such that loss of lock occurs (Teunissen & Montenbruck, 2017, p. 386). In such a scenario, measurements become noisy and thus impact the performance. That explains why this dissertation examined the performances of LM3GNSS receivers while roving at an average speed of 80 km per hour to simulate navigation speed rarely applied in a typical marine survey. This dissertation assessed the PPK solutions during five minivan surveys with baseline length from USMCS, reaching about 33 km at the farthest end of the route. Uncertainty in the up component rarely reaches 0.15 m (95% confidence level). The performance is often better than 0.1 m with any receiver or antenna, including the uncalibrated antennas. The worst performances are noted in sessions using the Zephyr3 antenna, particularly in pairing with Swift Navigation Duro (0.14m) and the Drotek DP601 (0.15m) receivers. Likewise, with the DA910 antenna (uncalibrated) paired with DP601 (0.13m) – all uncertainty at 95%. Like any high-end GNSS receivers,

Conclusion 3: LM3GNSS receivers can provide PPK solutions at medium (30 – 40 km) baselines at an accuracy better than 0.15m.

This dissertation also assessed the PPP results of the minivan sessions relative to NetR9 PPK results. It is reasonable to evaluate LM3GNSS PPP that way since the PPK results offer much better accuracy. In contrast, the instrument code and phase delays slow down the ambiguity resolution and convergence in PPP strategy but are easily removed in the double differencing algorithm. The PPP (minivan session) results show that the receiver's ability to track multi-GNSS and the inclusion of the trackable SVs in IGS products are essential to the performance of LM3GNSS receivers in PPP strategy. Eight of about eleven BDS MEO SVs that are trackable at USMCS are excluded in IGS MGEX products. Since very few BDS SVs are included in most PPP solutions for the minivan sessions, the performances of LM3GNSS hardware varies as a function of the number of SVs available in the solution.

The results show that kinematic PPP performances range between 0.1 and 0.8 m. Ten of the twenty hardware pairing scenarios show that PPP performance is better than 0.2m. Six of the pairing scenarios are better than 0.4m; three are better than 0.6m, while the DP0601 receiver combined with the HXCCSX601A antenna shows the worst performance of 0.8m at 95% confidence level. As expected, those PPP performances will not meet the maximum TVU tolerance for special-order in very shallow waters (0 – 20m) since the performance will vary with the convergence time and the number of tracked SVs. It is known that PPP convergences to a better accuracy with time.

Conclusion 4: LM3GNSS receivers in PPP strategy should meet order-1 and order-2 in shallow waters.

Another known challenge with kinematic PPP is post-cycle-slip convergence, where the accuracy is degraded until after a period when the ambiguity term is reasonably

resolved. Strategies such as PPP-AR will be explored as part of the future work discussed in the next section, to explore LM3GNSS receivers for high accuracy performances in shallow-water PPP or in a scenario where remotely operated vehicles require accurate and instant positioning solutions when launched from an offshore platform.

It is clear from the residual analysis that the Zephyr3 antenna, being a high-end GNSS antenna, may not offer the best improvement in LM3GNSS receivers' performance, especially on a dynamic platform. When the antennas are stationary, as with the case during SK-PPP sessions, the code and phase residuals for all hardware are better than 10 m and 0.04 m, respectively. However:

Conclusion 5: For both PPK and kinematic PPP in the minivan, the overall code and carrier residuals are better in hardware pairings with Polant than with the Zephyr3 antenna.

The measurement characterization of the LM3GNSS hardware shows that irrespective of the antenna paired with the Mosaic receiver, code-multipath is well-mitigated compared to the rest of the LM3GNSS receivers, which shows larger and varying code-multipath magnitude. The magnitude of code-multipath is less in Mosaic compared to NetR9.

Conclusion 6: Mosaic LM3GNSS receiver measurement quality performance is comparable or better than NetR9, as reflected in the positioning performances.

The results and analysis in Section 5.4.1 show that some CORSs are not well-suited for high-rate kinematic applications, and using such CORSs in PPK strategy is risky as the accuracy of the ellipsoidal height may be degraded by 0.20 m or worse, and as much as 50% of the results may be float solutions. That leads to:

Conclusion 7: LM3GNSS receivers will achieve optimum performance in PPK strategy if the reference station is multi-constellation enabled and the data acquisition rate at the reference station is sufficiently high.

6.1.2 Future Work

Future work will develop a ***comprehensive approach for adapting existing ANTEX file for use with uncalibrated low-cost antennas***. For the first time, this dissertation adapts existing ANTEX from the NGS database to improve the PPP results for observations with uncalibrated low-cost antennas. This area requires extensive exploration of how uncalibrated low-cost antennas might benefit from ANTEX file cloning.

Future work will determine how ***LM3GNSS performances in a harsh dynamic environment*** differ from the roving minivan performances, especially in typical hydrographic survey speed (up to 10 knots {18.5 km/hour}) and high degree attitude. It is expected that typical hydrographic survey speed should not degrade LM3GNSS performances. However, it is still unknown how significant attitude variations (e.g., roll and pitch) will impact the sensitivity of the receiver correlators and hence cycle slips

The ***performances of mass-market IMUs in combinations with LM3GNSS*** receivers for high accuracy marine positioning are desirable since hydrographic positioning hardware integrates GNSS+IMU. Recently, the GNSS industry has witnessed a surge in IMU technology development, driven by mass-market applications. There are indications that manufacturers are striving to deliver high accuracy products that will compete with the industry-grade hardware.

A future effort will explore ***LM3GNSS hardware in PPP-AR using GipsyX and Bernese GNSS*** software. Consider a scenario where fleets of unmanned vehicles are deployed from a large ship to deliver high accuracy products, say for engineering and habitat mapping, as soon as they are launched and powered. The unmanned vehicles will require a positioning strategy better than the conventional PPP strategy. In such a scenario, at remote locations where accuracy needs may be as tight as in the nearshore cases (i.e., pipe laying project), the PPP-AR strategy is either near real-time post-processing, offers a better alternative.

The author is curious whether a correlation exists among the ***vertical solution drift, residual corrections from ocean-loading, and data sampling rate at a reference station***, especially nearshore in PPK strategy (35 km baseline). Recall that this dissertation briefly touched on ocean-loading effects in PPP strategy (Section 4.4.3) and discussed the effect of data interpolation at 1 Hz from a 30 s observation file (Section 5.4.1). The assumption is that the double-differencing strategy applied in PPK should eliminate or minimize that error. That can only be true if the magnitude of the effect is the same on the sea as the land-bound reference station. Whether the effect is at all noticeable and relevant at sea is another question.

The author desires to show, empirically, whether ***PPP-AR, in atmospheric-constrained processing, would benefit from the choice of a weather model*** over another. As noted in GipsyX processing, the numerical and empirical weather models (NMF, GMF, VMF1, GPT2) for estimating hydrostatic and wet tropospheric delays are apriori inputs. Lagler et al. (2013) present GPT2 as an improvement over GMF, offering improved spatial and temporal resolutions, as well as improved apriori tropospheric delay

estimates. It is desirable to how if improved weather models have any impact on PPP results.

In the future, it is desirable to explore ***LM3GNSS receivers for low-cost GNSS buoys development***. That project will determine the best strategy that will achieve very high accuracy tide measurement on buoy platforms using LM3GNSS receivers and explore the potential of such a platform for chart datum determination at offshore locations. The study will apply the long-baseline processing strategy as available in the Bernese processing engine.

The author plans that GPM evolves into a GNSS research software capable of GNSS+INS processing sometimes in the future. That goal is intended to ensure the author's continuous capacity building in GNSS processing and algorithm developments. The first step towards achieving that goal would be the expansion of GPM to handle any GNSS data pre-processing steps and solution analysis adequately. That will include sidereal filtering for multipath, orbit interpolation using three-day arcs to address day-boundary value problems as discussed in this dissertation, full support for GLO to convert carrier-phase observable to range equivalent, ingestion of all IGS products including the SINEX, ERP, and clock files, the interpolation of global ionospheric and tropospheric models, cycle-slips search, ambiguity search, and eventually the implementation of PPP and PPP-AR for static observations. The author plans to unbundle GPM and implement all its algorithms in object-oriented programming accessible via a command-line and multiple GUI windows in Python programming language. Once those are achieved, the author will implement PPK algorithms (GNSS only) and, eventually, the GNSS+IMU processing.

Figure A.1a Zephyr3 antenna at USMCS. Swapped-out Zephyr3 antenna when using low-cost antennas

Figure A.1b Zephyr3 antenna mounted on the roving minivan

Figure A.1c ZBL setup (4 LM3GNSS receivers and Trimble NetR9) at USMCS.

Figure A.1d UB4B0M installed in a locally-built enclosure using a pelican case

Figure A.1 *USMCS setup, roving minivan, and UB4B0M in a pelican case*

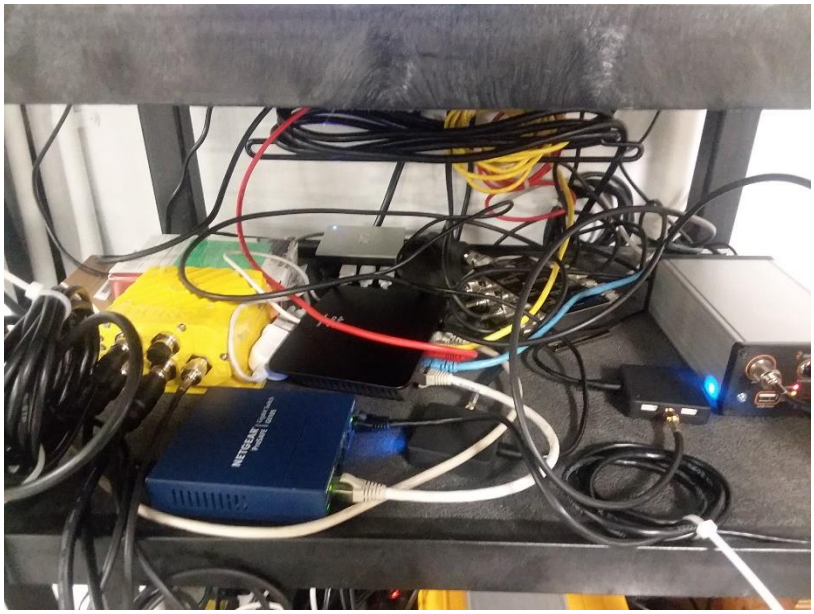

Figure A.2a ZBL setup at USMCS

Figure A.2b ZBL setup inside the roving minivan

Figure A.2 *Typical ZBL setups at USMCS and in the roving minivan*

UB4B0M receiver is not in the minivan picture because it was located in the rear due to crowed space in the front and proximity to a power outlet.

Figure A.3 *ZBL setup inside the roving minivan*

Note that the Drotek receiver is right on top of the Duro receiver only for the convenience of taking a vivid picture. Typical setup ensured separation between the recivers to avoid heat transfer. A typical minivan setup is shown in *Figure A.2b*

Figure A.4a Zephyr3

Figure A.4b PolaNt-x MF

Figure A.4c HXCCSX601A

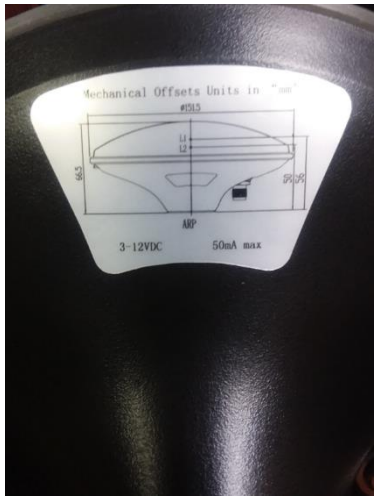

Figure A.4d DA910

Figure A.4e GPS500

Figure A.4 *Geodetic and low-cost antennas*

APPENDIX B GPM FUNCTION DESCRIPTION

Table B.1 *GPM function classification and description*

Function Classification	**Number of functions / Total number of lines**	**Function**	**Description**
DataMatching	6 / 18	intersect_2vec.m intersect_3vec.m intersect_4vec.m intersect_5vec.m intersect_6vec.m intersect_7vec.m	Intersects 2, …, seven vectors, and returns matching values; the matching values are later used elsewhere to find the indices of elements in the original vectors.
FileReaders	2 / 22	readCSRSposfile4.m readfiledirname.m	Reads all pos files from CSRS PPP in a given path Reads files in a given directory based on the given extension filename
Geodesy	20 / 182	calcM.m calcCT.m	Calculates projection factors, M, M1, …, M4 needed in UTM grid computations Returns C and T constants as a function of latitude in the direct and inverse problem of map projection on the UTM system

Function Classification	Number of functions / Total number of lines	Function	Description
		dayofweek.m	Returns the day of week number referenced to Sunday for a given date, such that Sunday is 0 Saturday is 6. It is capable of handling batch input and output
		ellipsab2ee.m	Returns first and second eccentricity (e, e') for a given major (a) and minor (b) axis of an ellipsoid
		ellipsaeLat2Rm.m	Returns prime vertical radius for a given latitude on an ellipsoid defined by a, e
		ellipsaf2ee.m	Returns first and second eccentricity (e, e') for a given a and flattening (f) of an ellipsoid
		ellipsoid_af_db.m	ellipsoid database
		gpsweeknum.m	Returns GPS week number vector for given date vector
		rotmat2localENU.m	Returns the rotation matrix E and ellipsoidal height vector for given vectors of x, y, z and given ellipsoid
		tow2civil.m	converts time of the week in seconds to hh:mm: ss vectors

Function Classification	Number of functions / Total number of lines	Function	Description
		xyz2enu.m	Returns easting, northing, ellipsoidal height, and zone number for a given vector of x, y, z on GRS80 and NAD83 ellipsoid.
		ellipaeLat2Rm.m	Returns prime meridian radius Rm for a given a, e, Lat
		ellipsab2f.m	Returns ellipsoid flattening from given a, and b
		ellipsaeLat2Rn.m	Returns prime vertical radius Rn for a given a, e, Lat
		ellipslatlon2EN.m	Returns easting, northing, and zone number of a given latitude and longitude on GRS80 and NAD83 ellipsoid; A sub-function that calls the ellipsoid database is expandable to include any other ellipsoid. It can handle batch processing
		gnsscal.m	Glues together the time-related functions to return a complete GNSS calendar, including GPS week, day of year, date, day of the week for a given vector of date.

Function Classification	Number of functions / Total number of lines	Function	Description
		tow_sec_2_hms.m	returns h:m: s for time of week given in seconds
		utct_j2k_2civil.m	Converts UTC in seconds, referenced to J2000 to civil time (i.e., wall clock format (h:m: s))
		xyz2llh.m	Returns latitude, longitude, and ellipsoidal height for given vectors of x, y, z
GipsyX	28 / 2,584	A_gipsyXAnalysis_Start_Here.m	GPM command line starter program
		gipsyX_mgr_CL_analysis.m	The main routine for managing GipsyX and GrafNav analysis; it maintains the main function branches into different operations and controls the project directory paths.
		gipsyX_mgr_ResDataPlot.m	Sorts code and residual phase data ingested from the GipsyX output file into the different constellation and generates the histograms and time series plots
		gipsyXCodePhaseRes.m	Optionally sorts code and phase residual data by three attributes, i.e., all, deleted, included

Function Classification	Number of functions / Total number of lines	Function	Description
		gipsyXCodePhaseSplit.m	Splits all code and phase residual file
		gipsyXIndofBadGood.m	Finds the index of good and bad data sets
		gipsyXllh2enu.m, gipsyXllh2enu_only.m	Transforms latitude, longitude, the height of GipsyX dataset to UTM grid by calling ellipslatlon2EN.m
		gipsyXResDataPlot.m	Plots
		gipsyXtdpSplit.m	Splits time-dependent parameter output file from GipsyX into clock bias solution file, satellite clock bias, station clock bias, receiver's x, y, z position, zenith tropospheric delay, tropospheric gradient
		stat_data4_gipsyXgNav_mgr.m	Analyses data, calculate statistics and writes the report to formatted ASCII file
		plot_data4_gipsyXgNav_mgr.m	Plots analyzed data
		gd2escript.m	Writes the script that runs GipsyX gd2e

Function Classification	Number of functions / Total number of lines	Function	Description
		masterstartscript.m	Writes GipsyX mater scripts for calling plotting, product download, products unzip, RINEX conversion to GipsyX native format, second-order ionospheric product download, and gfzrnx ASCII time plots scripts
		plotdenuscript.m	Auto-writes scripts to plot GipsyX output files
		prodfetchscript.m	Auto-writes scripts to fetch GNSS products
		produnzipscript.m	Auto-write scripts to unzip downloaded GNSS products
		rnx2datarecordscript.m	Auto-write scripts to convert RINEX data to GipsyX native format
		rnx2stndbscript.m	Auto-write scripts to create station database from RINEX file
		secdorderionoscript.m	Auto-write scripts to download second-order ionospheric files for GipsyX
		gfzrnxtimeplotscript.m	Writes scripts that call the gfzrnx tool in GipsyX for

Function Classification	Number of functions / Total number of lines	Function	Description
			writing ASCII time plot of observation per PRN
		tdp2llhscript.m	Auto-write script to convert time-dependent parameter file to latitude, longitude, and height
		copyresultscript.m	Copies output files from the GipsyX processing environment into an auto-named folder for onward analysis in GPM
		write_google_earth.m	Writes Google Earth kml file
GrafNav	8 / 765	A_gravNavAnalysis_Start_Here.m	Command-line caller for grafNav dataset analysis It provides switch options for ellipsoid type, plotting scale, cm / m unit, antenna dynamics, project type It calls gipsyX_mgr_CL_analysis, stat_data4_gipsyXgNav_mgr, and plot_data4_gipsyXgNav_mgr

Function Classification	Number of functions / Total number of lines	Function	Description
		grafNavResDataPlot.m	plots time series and histograms of code and phase residuals it decides on the legend based on the available dataset from multi-constellation
		grafNavResDataReport.m	It writes a summary report for the residual data in a text file
		grafNavResDataSort.m	Sorts GrafNav residual data into the respective constellation
		grafNavSatGeo_Stat.m	Plots number of satellites per constellation used in GrafNav solution, vertical dilution of precision (VDOP), standard deviation (SD) in the up component
		grafNavTxtDataRead.m	Reads GrafNav “jmez” ASCII format and converts it to a structured variable
		grafNavWrite_CAD_pt_txt.m	Writes script to auto plot GrafNav data in AutoCAD environment
GrafNavBinary	3 / 299	grafnav_bin_reader_fbp_rbp.m	Translate GrafNav residual binary file to ASCII

Function Classification	**Number of functions / Total number of lines**	**Function**	**Description**
		grafnav_bin2ascii_cleaner.m grafnav_bin2ascii_statistics.m	Cleans the translated file Computes statistics of ASCII file translated from GrafNav binary format
Maths	2 / 50	Lagrange.m decimalplace.m	Lagrange algorithm Determines the precision (up to 13 decimal place) of a floating number
NMEA	2 / 834	allTrimbleNmea.m allCnavNmea.m	Two NMEA file readers for sorting variants of NMEA strings into separate files It reads standard and proprietary NMEA strings from Trimble and CNAV receivers
Orbits	13 / 897	sp3interpol.m	It interpolates at a chosen interval, the ingested and sorted orbit; identifies interpolation gaps and sends orbit snippets, per time, containing 6 points on

Function Classification	Number of functions / Total number of lines	Function	Description
			either side of 1 gap to Lagrange interpolation function; It plots the 3-dimensional component of the all SV position vector and a 2-dimensional vector sample (G01)
		sp3reader.m	SP3 file reader
		sp3sortedplots.m	Plots SP3 data called from
		sp3sorting.m	Sorts SP3 data into the respective constellations in a structured variable
		gipsyX_constDB_reader.m	It reads the GipsyX constellation database and extracts PRN from active SVN to match the records in GipsyX interpolation output with the SP3 file
		gipsyX_pos_goa_reader.m	It reads the GipsyX satellite state output file after interpolation. The format is known in GipsyX as “PosGoa.”
		gipsyX_posgoa_sorting.m	It sorts the PosGoa variable (interpolated orbit) into respective constellation and PRNs

Function Classification	Number of functions / Total number of lines	Function	Description
		gipsyXposgoa_orbit_addprn.m	This function adds the respective PRN to the PosGoa variable, having matched the data with the GispyX constellation database
		gipsyXsvn2prn.m	gipsyXsvn2prn.m works with other PosGoa function in the process of converting SVN to PRN
		GPM_versus_GipsyX_orbit_start_here.m	The command-line interface for orbit validation processing
		gpm_vs_gipsyx_orbs.m	It finds the differences between two orbits and calculates the statistics
		gpm_vs_gpx_orb_diff_plotting.m	It plots orbit validation statistics
		orbclk_interp_write.m	This function writes the interpolated orbit to a CSV file
ProductsDownload	3 / 216	A_StartHere.m	Command-line script to download GNSS products from analysis centers supports downloads from CODE and JAXA. It is expandable to include downloads from any

Function Classification	Number of functions / Total number of lines	Function	Description
			open FTP sites. It unzips the products and deletes the zipped files.
		codescript.m	Auto writes the download script for CODE AC
		jaxscript.m	Auto writes the download script for JAXA AC
Rinex3Jinex	14 / 1492	Rnx3Jinex_SNR.m	Calls RINEX3 file reader (Rnx3Jinex_v5), find_code_sig_type, snrplot_per_const, snrplot_all_const, Rnx3Jinex_SP3_Multipath_Caller
		Rnx3Jinex_SNR_Start_Here.m	runs the command-line option for SNR and multipath analysis
		Rnx3Jinex_SP3_Multipath_Caller.m	A root function, supporting Rnx3Jinex_SNR_Start_Here.m
		Rnx3Jinex_v5.m	Main RINEX3 file reader
		find_code_sig_type.m	Finds code or phase data type in RINEX3 data
		find_prns_in_datatable.m	Prepares a list of unique PRNs from imported RINEX file
		gnssfreqdbase.m	GNSS frequency database

Function Classification	Number of functions / Total number of lines	Function	Description
		interp_rate_datamatch.m	Auto determine interpolation rate for orbit by examining RINEX3 data rate
		multipath_analysis.m	The primary multipath analysis tool
		rnx3_hdwr_list_finder.m	Finds all directories containing receiver-antennas names in a project folder path
		rnx3constnam2abr.m	Converts RINEX3 constellation name to abbreviated names (i.e., G to GPS, R to GAL, etcetera.)
		rnx3sorting_sys.m	A function for sorting RINEX3 data into datatypes per constellation. The function follows RINEX3 documentation and supports all documented frequency bands
		rnx3sorting_sys_level2.m	
		snrplot_all_const.m	Plots SNR for all constellation as a composite
		snrplot_per_const.m	Plots SNR on separate figures per constellation

Function Classification	Number of functions / Total number of lines	Function	Description
Statistics	1/10	order95CL.m	Finds the 95% confidence level for an ordered statistic

GPM runs a total of 8,692 lines of code grouped into 102 functions viz.: DataMatching functions, 18 lines of codes; FileReaders functions, 22 lines of codes; Geodesy, 182; GipsyX 2,584; GrafNav, 765; GrafNavBinary, 299; Maths, 50; NMEA, 834; Orbits, 897; ProductsDownload, 216; Rinex3Jinex, 1492; Statistics, 10; and GPM GUI runs 1323 lines of code.

B.2 How GPM GUI works

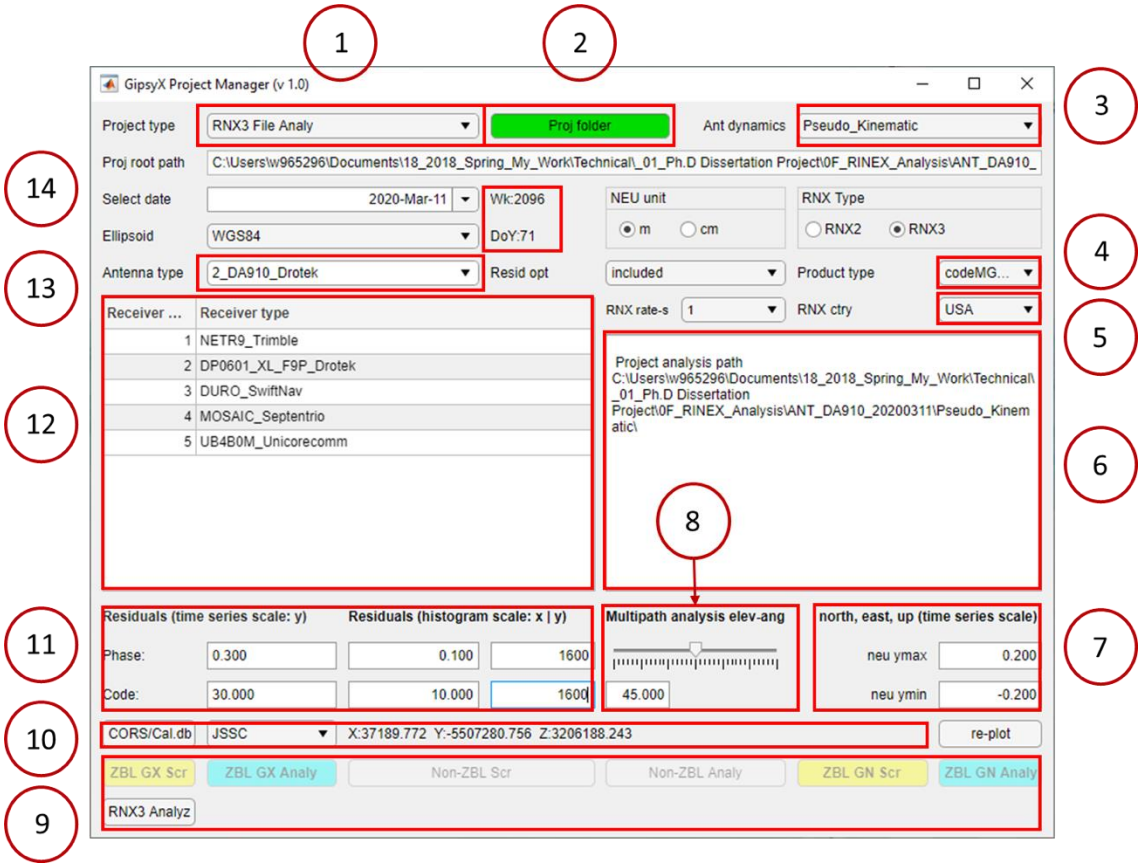

Figure B.1 *How GPM GUI works*

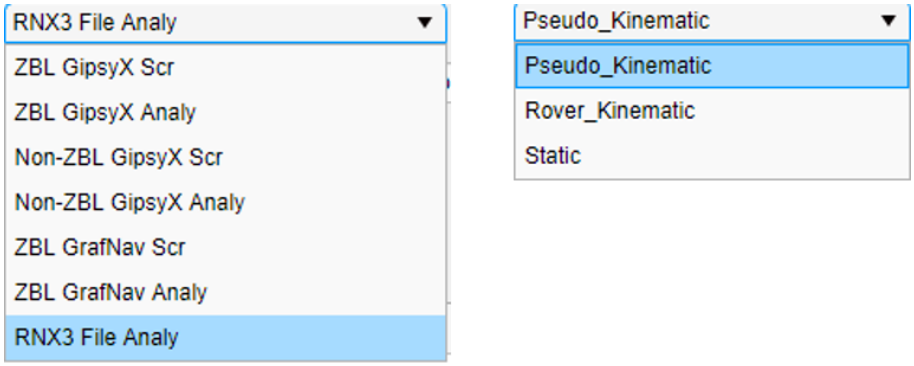

Figure B.2 *GPM project type (left) and antenna dynamics (right) options*

The following numbered bullets describe briefly how the GPM GUI works. The numbered bullets represent each item highlighted in Figure B.1.

1) PROJECT TYPE provides seven processing options in the drop-down list box (Figure B.2, left), associated with command buttons in (9). Only one button is activated at a time, depending on the option selected in (1)
2) PROJECT FOLDER defines the project path and must be a directory anywhere on the user system
3) ANTENNA DYNAMICS defines the antenna motion, and the options include kinematic, static, and simulated-kinematic (Figure B.2, right). The antenna-dynamics option is combined with the project path, date, antenna, and receiver names to define a unique project directory for a session. The project path is auto-generated, primarily when GPM is used in scripting mode. In analysis mode, GPM expects the user to create the project directory in a pattern similar to that of the scripting mode. The reason is that the user will have the move folder containing results from GipsyX and GrafNav to the GPM processing environment. GPM will check the user's directory and verify if it matches what it expects based on the antenna, receiver, date, and the root directory defined in (2). If the path is valid, it will trigger processing once the user pushes an active button in (9)
4) PRODUCT TYPE contains a list of product types and FTP links. The database serves dual purposes in that it is used to decide on the product type to download within GPM for orbit interpolation and subsequent multipath characterization as a function of SV elevations. It is also a database of product-type in GipsyX. A

selected option will be included in the batch files created in scripting mode for subsequent use in GipsyX "gd2e.py" program

5) RINEX COUNTRY (RNX CTR) contains the list of country codes used for all IGS MGEX stations according to the RINEX3 file naming convention
6) OUTPUT SCREEN displays the current project folder path; future versions will display processing logs
7) NEU TIME SERIES SCALE allows the user to define the y-axis plotting scale for north-east-up (NEU) time series
8) MULTIPATH ANALYSIS ELEVATION ANGLE allows the user to define the elevation angle for multipath characterization, using either the slider bar or the textbox
9) TRIGGER PANEL holds all the command buttons that activate the data processing for all project types in GPM. An active button in (9) triggers unattended scripting or processing pipeline, depending on the project type selected in (2)
10) COORDINATE DATABASE pulls the list of station names and their coordinates. The station names in the database are case sensitive. It is designed to be compatible with both RINEX 2 and RINEX3 file naming convention, which uses lower and upper cases, respectively, in some FTP repository
11) RESIDUAL SCALE PANEL holds textboxes for defining the scales for time series and histogram plots of residuals
12) RECEIVER DATABASE holds the receiver names extracted from a predefined ASCII file. A user can choose to remove a receiver from here without modifying

the receiver database, and the computation will be limited to what is displayed on the GPM GUI.

13) ANTENNA DATABASE extracts antenna names from a customizable ASCII file. Once those names are provided in the database, they will appear in GPM GUI for the user's selection.

14) DATE WEEK DOY PANEL provides a calendar up to 2040. In scripting mode, GPM converts a selected date to GPS week number and DOY and appends those to auto-generated batch files for unattended GipsyX processing.

Other features not described include options for data rate, plotting unit, and RINEX2 / RINEX3 file.

APPENDIX C WAYPOINT BINARY DOCUMENTATION

WAYPOINT BINARY VALUES OUTPUT FILE FORMAT
VERSION 8.70

This document outlines Waypoint's binary values output file format as it pertains to Version 8.70. This document may not be redistributed without the consent of NovAtel Inc.

Please note that all structures are aligned using 1-byte boundaries. NovAtel reserves the right to change this format at any time without prior notification. Any such changes are not guaranteed to maintain backwards-compatibility. If you have any questions, please contact Support at support@novatel.com.

File Header

This header appears once at the start of the file.

Field #	Data Type	Name	Comment	Bytes
1	char	szHdrStr	file header string; should be set to $BINVALUE	16
2	int16_t	sHdrSize	size of this header, in bytes; should be set to 7394	2
3	int16_t	sEpochSize	size of epoch record, in bytes; should be set to 68	2
4	int16_t	sBaselineSize	size of baseline record, in bytes; should be set to 30	2
5	int16_t	sSatelliteSize	size of satellite record, in bytes; should be set to 19	2
6	uint32_t	ulNumRecords	total number of epochs in this file	4
7	char	szReserved	reserved	48
8	int16_t	sNumBaseline	number of baselines per epoch (will be set to 1 for PPP)	2
9	char	szReserved	Reserved	7316

Total size = 7394 bytes

Epoch Record

This record appears once at the start of every epoch. This record will be followed by all of the baselin records, which will then be followed by all of the satellite records.

Field #	Data Type	Name	Comment	Bytes
1	uint16_t	usSync	sync bytes; should be 0xFF88	2
2	int16_t	sWeek	GPS week number (no roll-overs)	2
3	uint32_t	ulEpochTimeMs	GPS time, in milliseconds of the week	4
4	double	dECEFX	ECEF X-axis remote antenna position, in meters	8
5	double	dECEFY	ECEF Y-axis remote antenna position, in meters	8
6	double	dECEFZ	ECEF Z-axis remote antenna position, in meters	8
7	int16_t	sNumSatRec	number of satellite records to follow	2
8	char	szReserved	reserved	34

Total size = 68 bytes

Baseline Record

This record appears once per baseline for every epoch. Check *sNumBaseline* in the file header for the number of records to expect.

Field #	Data Type	Name	Comment	Bytes
1	unsigned char	ucFlag	validity flag; 1=baseline rejected, 0=baseline OK	1
2	unsigned char	ucNumSats	number of satellites used at this epoch	1
3	int16_t	sCaCode	RMS of all C/A code residuals, in meters (scaled by 100)	2
4	int16_t	sLnPhase	RMS of all L1 phase residuals, in meters (scaled by 5000)	2
5	int16_t	sDoppler	RMS of all L1 Doppler residuals, in m/s (scaled by 1000)	2
6	char	szReserved	reserved	2
7	uint16_t	usPDOP	PDOP value (scaled by 100); will be zeroed for PPP	2
8	uint16_t	usWeight	baseline weighting (0 to 1, scaled by 10000)	2
9	char	szReserved	reserved	16

Total size = 30 bytes

Satellite Record

This record appears once per satellite for each baseline that used it at the given epoch. Check *sNumSatRec* in the epoch record for the total number of records to expect. The records will be grouped by baseline. Check *ucNumSats* in the baseline record for the number of satellites expected for each baseline. Note that they will be ordered in the same way that the baseline records appear.

Field #	Data Type	Name	Comment	Bytes
1	unsigned char	ucPRN	satellite PRN; see table below	1
2	unsigned char	ucConst	constellation type; see table below	1
3	unsigned char	ucFlag	bit flag; see table below	1
4	int16_t	sCaCodeSD	C/A code standard deviation, in meters (scaled by 100)	2
5	int16_t	sLnPhaseSD	L1 phase standard deviation, in meters (scaled by 5000)	2
6	char	szReserved	reserved	4
7	int16_t	sCaCodeRes	C/A code residual, in meters (scaled by 100)	2
8	int16_t	sLnPhaseRes	L1 phase residual, in meters (scaled by 5000)	2
9	char	szReserved	reserved	4

Total size = 19 bytes

Definitions for *ucPRN* and *ucConst*:

Constellation	ucConst	ucPRN
GPS	0	1-32
GLONASS	1	1-24
BeiDou	2	1-37
QZSS	3	1-5
GALILEO	4	1-36

Definition for *ucFlag*:

Bit Value	Bit Definition
0x01	reserved
0x02	reserved
0x04	reserved
0x08	reserved
0x10	reserved
0x20	reserved
0x40	1=base satellite* 0=normal satellite
0x80	1=satellite was rejected* 0=satellite was used

* Satellite will not have any standard deviations or residuals computed (i.e., values will be zeroed)

APPENDIX D – NETWORK ADJUSTMENT REPORT (USMCS)

All coordinate accuracies reported here are 1σ formal uncertainties from the solution.

NGS BETA OPUS-Projects 1.49

Submitted by	Johnson Oguntuase
Solution File Name:	Network-Final_A.Sum
Solution Software:	GPSCOM (1908.29)
Solution Date:	2020-01-31t10:41:58 UTC
Standard Error of Unit Weight:	0.677
Total Number of Observations:	786,160
Total Number of Marks:	6
Constrained Marks:	1 Horizontal, 0 Vertical

MSIN: N30:18:42.20559 W089:36:15.50720 -17.296m

NAD_83 (2011) @ 2010.0000

MSIN 0.12cm 0.07cm 0.15cm NEU Sigma

Start Time:	2020-01-01t00:00:00 GPS
Stop Time:	2020-01-09t23:59:30 GPS
Frequency:	L1-Only to Ion-Free [By Baseline Length]
Observation Interval:	30 S
Elevation Cutoff:	15 Deg
Tropo Interval:	7200 S [Piecewise Linear Parameterization]
DD Correlations:	On

Table D.1 *Session Information*

Included Solution.		RMS	Software	Run date
1	2020-001 A	1.2 cm	page5(1908.29)	2020-01-31T10:36 UTC
2	2020-002 A	1.3 cm	page5(1908.29)	2020-01-31T02:03 UTC
3	2020-003 A	1.8 cm	page5(1908.29)	2020-01-31T08:11 UTC
4	2020-004 A	1.3 cm	page5(1908.29)	2020-01-31T08:22 UTC
5	2020-005 A	1.1 cm	page5(1908.29)	2020-01-31T02:20 UTC
6	2020-006 A	1.2 cm	page5(1908.29)	2020-01-31T02:20 UTC
7	2020-007 A	1.2 cm	page5(1908.29)	2020-01-31T08:24 UTC
8	2020-008 A	1.1 cm	page5(1908.29)	2020-01-31T02:23 UTC
9	2020-009 A	1.2 cm	page5(1908.29)	2020-01-31T08:28 UTC

Table D.2 *Baseline Information*

Baseline	Length	RMS	Obs	Omitted	Fixed in Solution(S)
jssc-msin	6.937 km	0.9 cm	155782	6.9%	99.8% 1, 2, 3,...
mary-msin	43.689 km	1.3 cm	159238	3.9%	97.9% 1, 2, 3,...
sbch-msin	49.623 km	1.4 cm	157494	5.2%	98.6% 1, 2, 3,...
covg-msin	50.595 km	1.4 cm	159952	3.4%	97.4% 1, 2, 3,...
eng6-msin	57.958 km	1.3 cm	153694	3.8%	99.1% 1, 2, 3,...

Table D.3 *Mark Estimated - A Priori Coordinate Shifts*

Mark	North (m)	East (m)	Up (m)
covg	0.008 (0.001)	-0.002 (0.000)	-0.002 (0.001)
eng6	0.005 (0.001)	-0.002 (0.000)	0.005 (0.001)
jssc	0.001 (0.001)	-0.007 (0.000)	-0.014 (0.001)
mary	0.007 (0.001)	-0.001 (0.000)	0.023 (0.001)
msin	0.001 (0.001)	0.000 (0.000)	0.000 (0.001)
sbch	0.010 (0.001)	0.001 (0.000)	0.000 (0.001)

Table D.4 *USMCS Coordinates*

Ref Frame	**NAD_83(2011) @ 2010.0000 (m)**		**ITRF2014 @ 2020.0123 (m)**	
X	37190.616	0.000	37189.772	0.000
Y	-5507282.250	0.001	-5507280.756	0.001
Z	3206188.424	0.001	3206188.243	0.001
LAT	30 22 25.79023	0.001	30 22 25.80980	0.001
E LON	270 23 12.88278	0.000	270 23 12.85156	0.000
W LON	89 36 47.11722	0.000	89 36 47.14844	0.000
EL HGT	-13.067	0.001	-14.452	0.001
ORTHO HGT	14.045	0.015	(= EL HGT - -27.112 GEOID18 HGT)	

Table D.5 *Grid Coordinates*

	UTM Coordinates UTM (Zone 16)	**State Plane Coordinates SPC (2301 MS E)**
Northing (Y)	3363106.750 m	97118.385 m
Easting (X)	248880.804 m	225050.554 m
Convergence	-1.32197500 deg	-0.39429444 deg
Point Scale	1.00037804	1.00001927
Combined Factor	1.00038009	1.00002132

US NATIONAL GRID DESIGNATOR: 16RBU4888063106 (NAD 83)

APPENDIX E – MULTIPATH IN GPM AND GRAFNAV

This appendix compares the multipath estimation in GPM and GrafNav. Figure E.1 shows code minus carrier estimation for the first twelve GPS SVs in GrafNav software, while Figure E.2 shows the same GPM estimation. Figure E.3 and Figure E.4 show GPM's processing steps in the removal of ionospheric delay and biases.

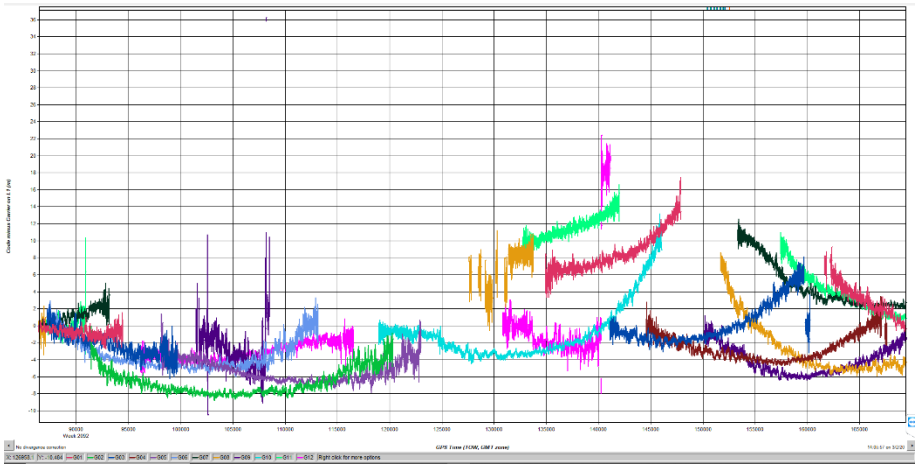

Figure E.1 *GrafNav's code minus carrier (GPS SV 01 to 12)*

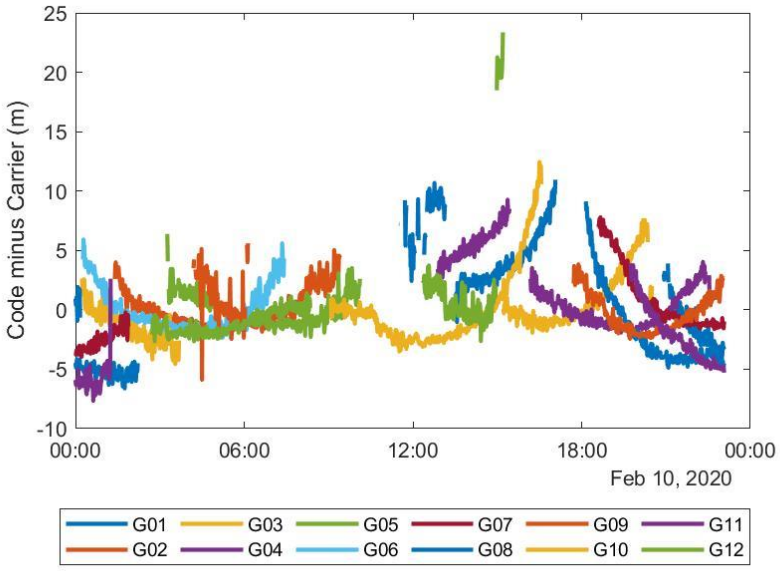

Figure E.2 *GPM's code minus carrier (GPS SV 01 to 12)*

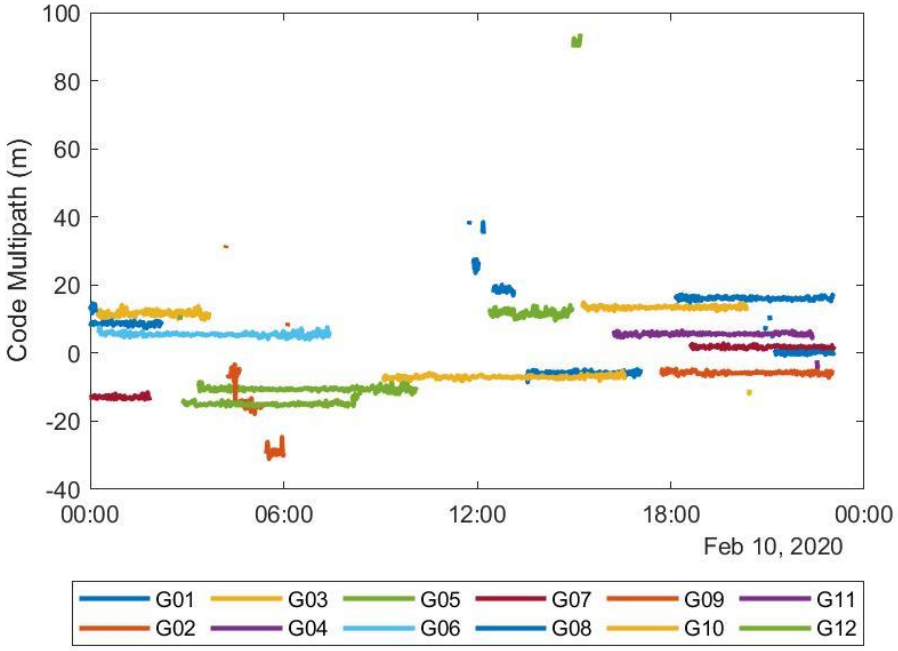

Figure E.3 *GPM ionospheric-free multipath (biased) estimation (GPS SV 01 to 12)*

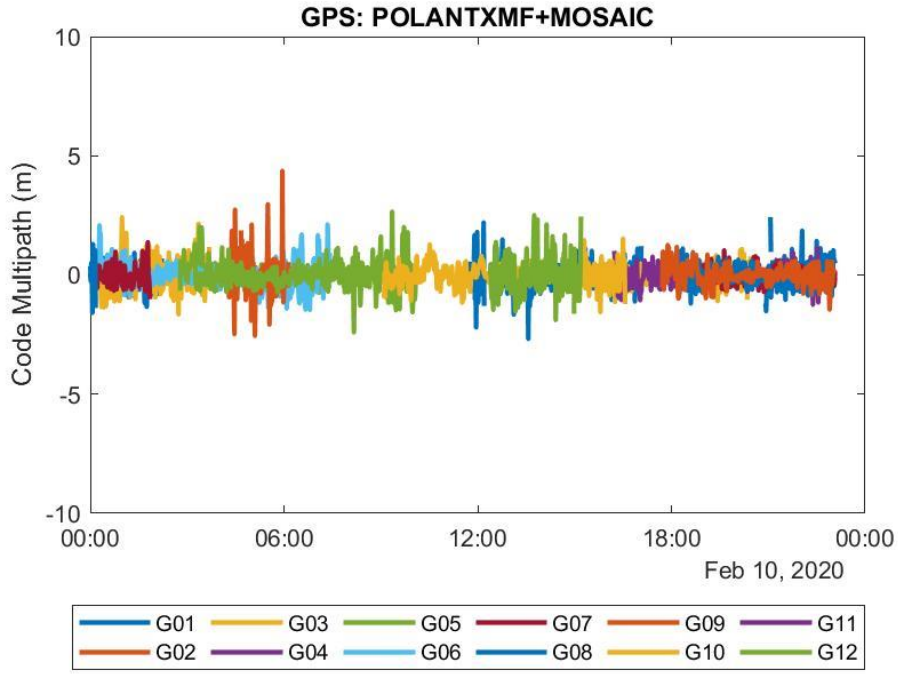

Figure E.4 *GPM ionospheric-free multipath (unbiased) estimation (GPS SV 01 to 12)*

APPENDIX F EXTERNAL FIGURES

This external appendix is available as an online link on request at Johnson.oguntuase@usm.edu. It contains a total of 39 folders, 975 figures, and five pdfs (LM3GNSS datasheets). Figure F.1 is the navigation tree of the external appendix. Note that the branches reflect the relevant section numbers where the figures are discussed in the dissertation.

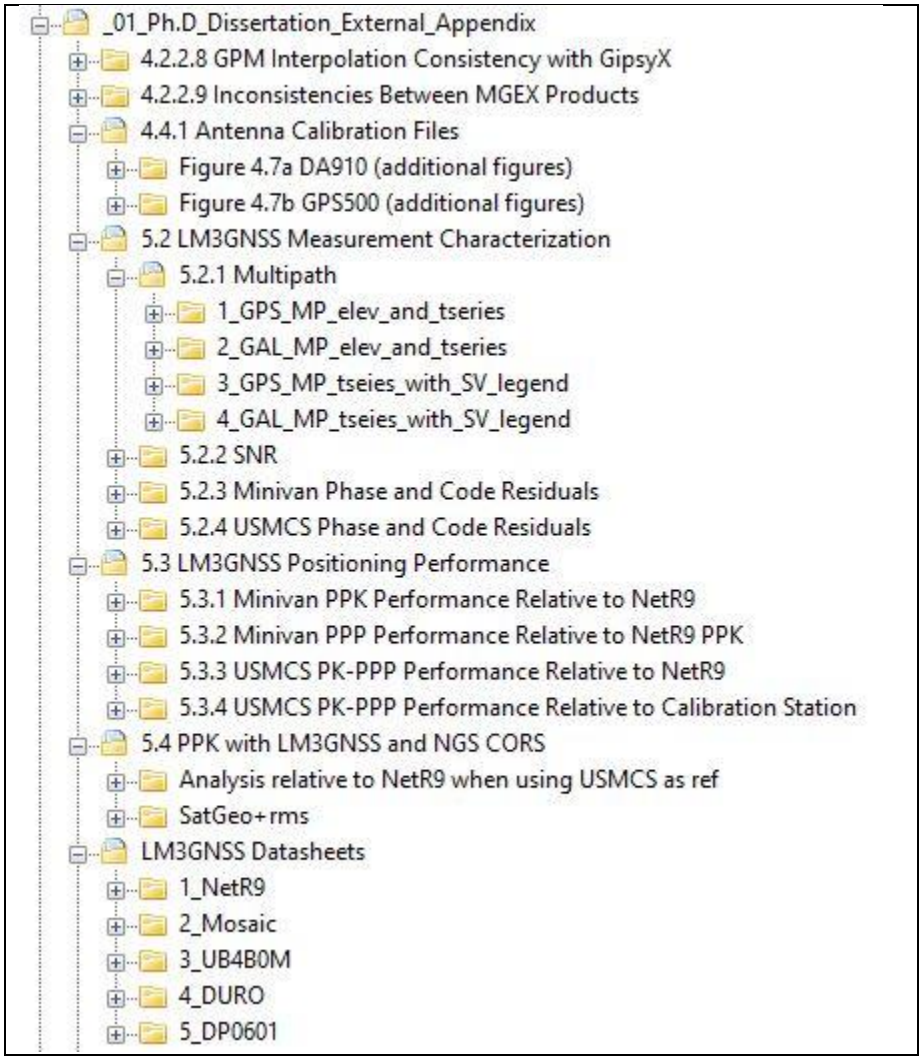

Figure F.1 *External appendix navigation tree*

REFERENCES

Aggrey, J., Bisnath, S., Naciri, N., Shinghal, G., & Yang, S. (2019). Accuracy trend analysis of low-cost GNSS chips: The case of multi-constellation GNSS PPP. *Proceedings of the 32nd International Technical Meeting of the Satellite Division of the Institute of Navigation, ION GNSS+ 2019*, 3618–3635. https://doi.org/10.33012/2019.16971

Banville, S., & Diggelen, F. van. (2016). Precise GNSS for Everyone: Precise Positioning Using Raw GPS Measurements from Android Smartphones. *GPS World.*, *27*(November), 43–48.

Banville, S., Lachapelle, G., Ghoddousi-Fard, R., & Gratton, P. (2019). Automated processing of low-cost GNSS receiver data. *Proceedings of the 32nd International Technical Meeting of the Satellite Division of the Institute of Navigation, ION GNSS+ 2019*, 3636–3652. https://doi.org/10.33012/2019.16972

Bertiger, W., Bar-Sever, Y., Dorsey, A., Haines, B., Harvey, N., Hemberger, D., Heflin, M., Lu, W., Miller, M., Moore, A. W., Murphy, D., Ries, P., Romans, L., Sibois, A., Sibthorpe, A., Szilagyi, B., Vallisneri, M., & Willis, P. (2020). GipsyX/RTGx, A New Tool Set for Space Geodetic Operations and Research. *Advances in Space Research*. https://doi.org/10.1016/j.asr.2020.04.015

Bertiger, W., Desai, S. D., Haines, B., Harvey, N., Moore, A. W., Owen, S., & Weiss, J. P. (2010). Single receiver phase ambiguity resolution with GPS data. *Journal of Geodesy*, *84*(5), 327–337. https://doi.org/10.1007/s00190-010-0371-9

Bisnath, S., & Langley, R. (2001). Pseudorange multipath mitigation by means of multipath monitoring and de-weighting. *KIS 2001, Proceedings of International*

Symposium on Kinematic Systems in Geodesy, Geomatics and Navigation, *June*, 392–400. http://gauss.gge.unb.ca/papers.pdf/kis01.bisnath.pdf

Bos, M. S., & Scherneck, H.-G. (2005). *The free ocean tide loading provider*. Onsala Space Observatory, Chalmers University of Technology, Gothenburg, Sweden. http://www.oso.chalmers.se/~loading

Cai, C., Gao, Y., Pan, L., & Zhu, J. (2015). Precise point positioning with quad-constellations: GPS, BeiDou, GLONASS and Galileo. *Advances in Space Research*, *56*(1), 133–143. https://doi.org/10.1016/j.asr.2015.04.001

Chen, H., Jiang, W., Ge, M., Wickert, J., & Schuh, H. (2014). An enhanced strategy for GNSS data processing of massive networks. *Journal of Geodesy*, *88*(9), 857–867. https://doi.org/10.1007/s00190-014-0727-7

Chen, X., Parini, C. G., Collins, B., Yao, Y., & Ur Rehman, M. (2012). Antennas for Global Navigation Satellite Systems. *Antennas for Global Navigation Satellite Systems*, *100*(7), 2349–2355. https://doi.org/10.1002/9781119969518

Choy, S., Bisnath, S., & Rizos, C. (2017). Uncovering common misconceptions in GNSS Precise Point Positioning and its future prospect. *GPS Solutions*, *21*(1), 13–22. https://doi.org/10.1007/s10291-016-0545-x

CSRS PPP. (2020). *CSRS-PPP News*. https://webapp.geod.nrcan.gc.ca/geod/tools-outils/ppp-update.php?locale=en

Dodd, D., & Mills, J. (2012). Ellipsoidally Referenced Surveys Separation Models. *FIG Working Week 2012, Knowing to Manage the Territory, Protect the Environment, Evaluate the Cultural Heritage.*, *2012*, 1–20.

Gebre-Egziabher, D., Jackson, J., Saborio, R., Ghazanfar, S. A., & Davis, B. (2018).

Evaluation of Low-Cost , Centimeter-Level Accuracy OEM GNSS Receivers. *Minnesota Department of Transportation*, *February*. http://www.dot.state.mn.us/research/reports/2018/201810.pdf

Ghilani, C. D. (2010). *Adjustment Computations Spatial Data Analysis* (5th ed.). John Wiley & Sons. https://doi.org/10.1002/9781119390664

Gill, M., Bisnath, S., Aggrey, J., & Seepersad, G. (2018). Precise Point Positioning (PPP) using Low-Cost and Ultra-Low-Cost GNSS Receivers. *Proceedings of the 30th International Technical Meeting of The Satellite Division of the Institute of Navigation (ION GNSS+ 2017)*, *May*, 226–236. https://doi.org/10.33012/2017.15123

Gross, J. (2016). *Advances in GIPSY GNSS / IMU Integrated Positioning and Application to UAVs Goals & Motivation*.

Guo, F., Li, X., Zhang, X., & Wang, J. (2017). Assessment of precise orbit and clock products for Galileo, BeiDou, and QZSS from IGS Multi-GNSS Experiment (MGEX). *GPS Solutions*, *21*(1), 279–290. https://doi.org/10.1007/s10291-016-0523-3

Guo, J., Xu, X., Zhao, Q., & Liu, J. (2016). Precise orbit determination for quad-constellation satellites at Wuhan University: strategy, result validation, and comparison. *Journal of Geodesy*, *90*(2), 143–159. https://doi.org/10.1007/s00190-015-0862-9

Håkansson, M. (2019). Characterization of GNSS observations from a Nexus 9 Android tablet. *GPS Solutions*, *23*(1), 1–14. https://doi.org/10.1007/s10291-018-0818-7

Hammerstad, E. (2001). *Subject : Multibeam Echo Sounder Accuracy*. 1–19.

Hare, R., Godin, A., & Mayer, L. (1995). *Accuracy Estimation of Canadian Swath and Sweep Sounding Systems*.

Hauschild, A., Montenbruck, O., & Langley, R. B. (2020). Flight results of GPS-based attitude determination for the Canadian CASSIOPE satellite. *Navigation, Journal of the Institute of Navigation*, *67*(1), 83–93. https://doi.org/10.1002/navi.348

Hofmann-Wellenhof, B., Lichtenegger, H., & Wasle, E. (2007). *Global Navigation Satellite Systems GPS, GLONASSS, Galileo & more* (2008th ed., Vol. 136, Issue 1). Springer-Verlag Wien.

HSSD. (2019). *Hydrographic Surveys Specifications and Deliverables*. *March*. https://nauticalcharts.noaa.gov/publications/docs/standards-and-requirements/specs/hssd-2019.pdf

IHO. (2008). *IHO Standards for Hydrographic Surveys* (5th, Febru ed.). The International Hydrographic Bureau, Monaco.

International GNSS Service. (2020). *IGS MGEX Products*. http://mgex.igs.org/IGS_MGEX_Products.php

Jokinen, A., Infante, E., Norman, L., de Groot, L., & Kruger, B. (2018). Precise Positioning for Automotive with Mass Market GNSS Chipsets. *Proceedings of the 31st International Technical Meeting of The Satellite Division of the Institute of Navigation (ION GNSS+ 2018)*, 596–610. https://doi.org/10.33012/2018.16003

Kazmierski, K., Sośnica, K., & Hadas, T. (2018). Quality assessment of multi-GNSS orbits and clocks for real-time precise point positioning. *GPS Solutions*, *22*(1). https://doi.org/10.1007/s10291-017-0678-6

Khodabandeh, A., & Teunissen, P. J. G. (2015). An analytical study of PPP-RTK

corrections: precision, correlation and user-impact. *Journal of Geodesy*, *89*(11), 1109–1132. https://doi.org/10.1007/s00190-015-0838-9

Kirkko-Jaakkola, M., Söderholm, S., Honkala, S., Koivula, H., Nyberg, S., & Kuusniemi, H. (2015). Low-cost precise positioning using a national GNSS network. *28th International Technical Meeting of the Satellite Division of the Institute of Navigation, ION GNSS 2015*, *4*, 2570–2577.

Kreyszig, E., Kreyszig, H., & Norminton, E. J. (2011). *Advanced Engineering Mathematics* (10th ed.). John Wiley & Sons, Inc. http://www.wiley.com/college/kreyszig

Lagler, K., Schindelegger, M., Böhm, J., Krásná, H., & Nilsson, T. (2013). GPT2: Empirical slant delay model for radio space geodetic techniques. *Geophysical Research Letters*, *40*(6), 1069–1073. https://doi.org/10.1002/grl.50288

Liu, T., Yuan, Y., Zhang, B., Wang, N., Tan, B., & Chen, Y. (2017). Multi-GNSS precise point positioning (MGPPP) using raw observations. *Journal of Geodesy*, *91*(3), 253–268. https://doi.org/10.1007/s00190-016-0960-3

Liu, W., Shi, X., Zhu, F., Tao, X., & Wang, F. (2019). Quality analysis of multi-GNSS raw observations and a velocity-aided positioning approach based on smartphones. *Advances in Space Research*, *63*(8), 2358–2377. https://doi.org/10.1016/j.asr.2019.01.004

Liu, Y., Lou, Y., Ye, S., Zhang, R., Song, W., Zhang, X., & Li, Q. (2017). Assessment of PPP integer ambiguity resolution using GPS, GLONASS and BeiDou (IGSO, MEO) constellations. *GPS Solutions*, *21*(4), 1647–1659. https://doi.org/10.1007/s10291-017-0641-6

Lou, Y., Zheng, F., Gu, S., Wang, C., Guo, H., & Feng, Y. (2016). Multi-GNSS precise point positioning with raw single-frequency and dual-frequency measurement models. *GPS Solutions*, *20*(4), 849–862. https://doi.org/10.1007/s10291-015-0495-8

Mayer, L., Jakobsson, M., Allen, G., Dorschel, B., Falconer, R., Ferrini, V., Lamarche, G., Snaith, H., & Weatherall, P. (2018). The Nippon Foundation—GEBCO Seabed 2030 Project: The Quest to See the World's Oceans Completely Mapped by 2030. *Geosciences*, *8*(2), 63. https://doi.org/10.3390/geosciences8020063

Mills, J., & Dodd, D. (2014). Ellipsoidally Referenced Surveying for Hydrography. In *International Federation of Surveyor (FIG)* (Issue 62).

Montenbruck, O., Steigenberger, P., Prange, L., Deng, Z., Zhao, Q., Perosanz, F., Romero, I., Noll, C., Stürze, A., Weber, G., Schmid, R., MacLeod, K., & Schaer, S. (2017). The Multi-GNSS Experiment (MGEX) of the International GNSS Service (IGS) – Achievements, prospects and challenges. *Advances in Space Research*, *59*(7), 1671–1697. https://doi.org/10.1016/j.asr.2017.01.011

NASA. (2018). *CDDIS - Data and Derived Products - GNSS MGEX Data*. https://cddis.nasa.gov/Data_and_Derived_Products/GNSS/gnss_mgex.html

National Geodetic Survey. (2019). *OPUS Projects*. https://www.ngs.noaa.gov/OPUS-Projects/

National Ocean Service. (2018). *Hydrographic Surveys Specifications and Deliverables (2018)*. *April*.

Nie, Z., Liu, F., & Gao, Y. (2020). Real-time precise point positioning with a low-cost dual-frequency GNSS device. *GPS Solutions*, *24*(1). https://doi.org/10.1007/s10291-019-0922-3

NOAA. (2020). *Index of /cors/*. ftp://geodesy.noaa.gov/cors/

Odolinski, R., & Teunissen, P. J. G. (2017). Low-cost, high-precision, single-frequency GPS–BDS RTK positioning. *GPS Solutions*, *21*(3). https://doi.org/10.1007/s10291-017-0613-x

Parkins, A., Hide, C., & Ammann, D. (2018). *GNSS RTK for Mass Market Applications*. 580–595.

Pesyna, K. M., Heath, R. W., & Humphreys, T. E. (2014). Centimeter Positioning with a Smartphone-Quality GNSS Antenna. *ION GNSS Conference*, 10. https://pdfs.semanticscholar.org/d439/e85aab7bce7e9361fe3ad68c55c28c0e8c5a.pdf

Pirazzi, G., Mazzoni, A., Biagi, L., & Crespi, M. (2018). Preliminary Performance Analysis with a GPS+Galileo Enabled Chipset Embedded in a Smartphone. *Proceedings of the 30th International Technical Meeting of The Satellite Division of the Institute of Navigation (ION GNSS+ 2017)*, *November*, 101–115. https://doi.org/10.33012/2017.15260

Pustoshilov, A. S., & Tsarev, S. P. (2017). Universal coefficients for precise interpolation of GNSS orbits from final IGS SP3 data. *2017 International Siberian Conference on Control and Communications, SIBCON 2017 - Proceedings*, *June 2017*. https://doi.org/10.1109/SIBCON.2017.7998463

Rice, G., & Riley, J. (2011). Measuring the Water Level Datum Relative to the Ellipsoid During Hydrographic Survey. *Proceedings of the U.S. Hydro 2011 Conference*. http://ushydro.thsoa.org/hy11/0427A_08.pdf%0Ahttp://www.thsoa.org/hy11/0427A_08.pdf

Seepersad, G., & Bisnath, S. (2015). Reduction of PPP convergence period through

pseudorange multipath and noise mitigation. *GPS Solutions*, *19*(3), 369–379. https://doi.org/10.1007/s10291-014-0395-3

Siddakatte, R., Broumandan, A., & Lachapelle, G. (2017). Performance Evaluation of Smartphone Gnss Measurements With Different Antenna Configurations. *Presented at Royal Institute of Navigation International Navigation Conference*, *1*(November), 27–30.

Smith, S. M. (2018). Seabed 2030: A Call to action. *Hydro International*, *22*(1), 22–23.

Smolyakov, I., Rezaee, M., & Langley, R. B. (2019). *Resilient Multipath Prediction and Detection Architecture for Low-cost Navigation in Challenging Urban Areas*. 175–188.

Soffel, M., Klioner, S. A., Petit, G., Wolf, P., Kopeikin, S. M., Bretagnon, P., Brumberg, V. A., Capitaine, N., Damour, T., Fukushima, T., Guinot, B., Huang, T.-Y., Lindegren, L., Ma, C., Nordtvedt, K., Ries, J. C., Seidelmann, P. K., Vokrouhlick, D., Will, C. M., & Xu, C. (2003). The IAU 2000 Resolutions for Astrometry, Celestial Mechanics, and Metrology in the Relativistic Framework: Explanatory Supplement. *The Astronomical Journal*, *126*(6), 2687–2706. https://doi.org/10.1086/378162

Steigenberger, P., Hugentobler, U., Loyer, S., Perosanz, F., Prange, L., Dach, R., Uhlemann, M., Gendt, G., & Montenbruck, O. (2015). Galileo orbit and clock quality of the IGS Multi-GNSS Experiment. *Advances in Space Research*, *55*(1), 269–281. https://doi.org/10.1016/j.asr.2014.06.030

Stroud, K. A., & Booth, D. J. (2003). *Advanced-Engineering-Mathematics-4th-ed-k-stroud-signed-download.pdf* (4th ed.). Palgrave Macmillan.

Sun, J., Liu, J., Fan, S., & Lu, X. (2015). Multi-GNSS PPP and PPP-RTK: Some GPS+BDS Results in Australia. *Lecture Notes in Electrical Engineering*, *340*(November). https://doi.org/10.1007/978-3-662-46638-4

Tegedor, J., Øvstedal, O., & Vigen, E. (2014). Precise orbit determination and point positioning using GPS, Glonass, Galileo and BeiDou. *Journal of Geodetic Science*, *4*(1), 65–73. https://doi.org/10.2478/jogs-2014-0008

Teunissen, P. J. G., & Kleusberg, A. (1998). GPS for Geodesy. In *GPS for Geodesy* (2nd ed.). Springer Berlin Heidelberg. https://doi.org/10.1007/978-3-642-72011-6

Teunissen, Peter J.G., & Montenbruck, O. (Eds. . (2017). *Spinger Handbook of Global Navigation Satellite Systems* (Peter J.G. Teunissen & O. (Eds. . Montenbruck (eds.)). Springer International Publishing. https://doi.org/10.1007/978-3-319-42928-1

The Nippon Foundation-GEBCO Seabed 2030 Project. (2020). *Nearly a fifth of world's ocean floor now mapped*. https://seabed2030.gebco.net/news/gebco_2020_release.html

Villiger, A., Dach, R. (eds. . (2017). International GNSS Service Technical Report 2017 (IGS Annual Report). *IGS Central Bureau and University of Bern*. https://doi.org/XXXXXX

Villiger, A., Dach, R. (eds. . (2019). *International GNSS Service Technical Report 2018 (IGS Annual Report)*. https://doi.org/10.7892/boris.116377

Wanninger, L., & Heßelbarth, A. (2020). GNSS code and carrier phase observations of a Huawei P30 smartphone: quality assessment and centimeter-accurate positioning. *GPS Solutions*, *24*(2), 1–9. https://doi.org/10.1007/s10291-020-00978-z

Wübbena, G., Schmitz, M., & Bagge, A. (2005). PPP-RTK : Precise Point Positioning

Using State-Space Representation in RTK Networks. *Proc. ION ITM 2005, Institute Of Navigation, Long Beach, CA, USA, September 13 - 16*, 2584–2594. http://ww.ion.org/publications/abstract.cfm?articleID=6467

Yoaz, B.-S. (2017). *RTGx/GipsX: A New Generation of GNSS Navigation Software*. 1–9. https://www.nasa.gov/sites/default/files/atoms/files/session_1_-_6_rtgx_gipsy_a_new_generation_of_gnss_navigation_software_yoaz_bar-sever_0.pdf

Zhang, B. C., Teunissen, P. J. G., & Odijk, D. (2010). *A Novel Un-differenced PPP-RTK Concept*. *2*.

Zhang, X., Tao, X., Zhu, F., Shi, X., & Wang, F. (2018). Quality assessment of GNSS observations from an Android N smartphone and positioning performance analysis using time-differenced filtering approach. *GPS Solutions*, *22*(3), 1–11. https://doi.org/10.1007/s10291-018-0736-8

Zhao, Q., Wang, C., Guo, J., Wang, B., & Liu, J. (2018). Precise orbit and clock determination for BeiDou-3 experimental satellites with yaw attitude analysis. *GPS Solutions*, *22*(1), 1–13. https://doi.org/10.1007/s10291-017-0673-y

Zumberge, J. F., Heftin, M. B., Jefferson, D., Watkins, M. M., & Webb, F. H. (1997). Precise point positioning for the efficient and robust analysis of GPS data from large networks. *Journal of Geophysical Research*, *102*(10), 5005–5017. https://doi.org/10.1029/96JB03860